**Springer Theses**
Recognizing Outstanding Ph.D. Research

Guangmin Zhou

# Design, Fabrication and Electrochemical Performance of Nanostructured Carbon Based Materials for High-Energy Lithium–Sulfur Batteries

## Next-Generation High Performance Lithium–Sulfur Batteries

Springer

## Springer Theses

Recognizing Outstanding Ph.D. Research

## Aims and Scope

The series "Springer Theses" brings together a selection of the very best Ph.D. theses from around the world and across the physical sciences. Nominated and endorsed by two recognized specialists, each published volume has been selected for its scientific excellence and the high impact of its contents for the pertinent field of research. For greater accessibility to non-specialists, the published versions include an extended introduction, as well as a foreword by the student's supervisor explaining the special relevance of the work for the field. As a whole, the series will provide a valuable resource both for newcomers to the research fields described, and for other scientists seeking detailed background information on special questions. Finally, it provides an accredited documentation of the valuable contributions made by today's younger generation of scientists.

## Theses are accepted into the series by invited nomination only and must fulfill all of the following criteria

- They must be written in good English.
- The topic should fall within the confines of Chemistry, Physics, Earth Sciences, Engineering and related interdisciplinary fields such as Materials, Nanoscience, Chemical Engineering, Complex Systems and Biophysics.
- The work reported in the thesis must represent a significant scientific advance.
- If the thesis includes previously published material, permission to reproduce this must be gained from the respective copyright holder.
- They must have been examined and passed during the 12 months prior to nomination.
- Each thesis should include a foreword by the supervisor outlining the significance of its content.
- The theses should have a clearly defined structure including an introduction accessible to scientists not expert in that particular field.

More information about this series at http://www.springer.com/series/8790

Guangmin Zhou

# Design, Fabrication and Electrochemical Performance of Nanostructured Carbon Based Materials for High-Energy Lithium–Sulfur Batteries

## Next-Generation High Performance Lithium–Sulfur Batteries

Doctoral Thesis accepted by
Institute of Metal Research, Chinese Academy of Sciences, China

Springer

*Author*
Dr. Guangmin Zhou
Institute of Metal Research
Chinese Academy of Sciences
Shenyang
People's Republic of China

*Supervisors*
Prof. Hui-Ming Cheng
Shenyang National Laboratory for Materials Science, Institute of Metal Research
Chinese Academy of Sciences
Shenyang
People's Republic of China

Prof. Feng Li
Shenyang National Laboratory for Materials Science, Institute of Metal Research
Chinese Academy of Sciences
Shenyang
People's Republic of China

ISSN 2190-5053 ISSN 2190-5061 (electronic)
Springer Theses
ISBN 978-981-10-3405-3 ISBN 978-981-10-3406-0 (eBook)
DOI 10.1007/978-981-10-3406-0

Library of Congress Control Number: 2016961671



Printed on acid-free paper

This Springer imprint is published by Springer Nature
The registered company is Springer Nature Singapore Pte Ltd.
The registered company address is: 152 Beach Road, #22-06/08 Gateway East, Singapore 189721, Singapore

# Supervisors' Foreword

The ever-increasing demand for economical and efficient electrochemical energy storage technologies has triggered continuous exploration of advanced battery systems. Lithium-ion batteries have dominated the battery market for consumer electronic devices since the 1990s and with over two decades of improvements, their energy density is now close to the theoretical limit but cannot meet the requirements of new electric vehicles (EVs), hybrid EVs, and next-generation portable electronic devices. Therefore, it is urgently needed to develop high-capacity electrode materials and explore new battery systems that use a multi-electron reaction in order to achieve a high-energy density.

Sulfur, as a cathode material, can react with lithium to form $Li_2S$ with a two-electron reaction process, leading to a lithium–sulfur battery with a high theoretical capacity of 1675 mAh $g^{-1}$ and an energy density (2600 Wh $kg^{-1}$), which is 7 times that of lithium-ion batteries ($LiCoO_2$ cathode and graphite anode with a theoretical energy density of 360 Wh $kg^{-1}$). Sulfur is also inexpensive, abundant, and nontoxic. Therefore, lithium–sulfur batteries are considered promising next-generation high-energy batteries. However, sulfur has a low electrical conductivity, low material utilization, poor structural stability, and low cycle life during discharge/charge. Carbon materials, including carbon nanotubes and graphene, have a large surface area, high electrical conductivity, abundant porosity, and can also be associated with various surface functional groups. They can be used to construct electrically conductive networks, anchor/disperse sulfur, buffer the volume change of sulfur during cycling, and consequently obtain high performance. Therefore, sulfur/carbon materials are promising electrode materials for lithium–sulfur batteries.

Aiming at high-performance electrodes and devices, Dr. Guangmin Zhou's work focuses on sulfur/carbon hybrid cathode materials, including hierarchical porous carbons, graphene, and carbon nanotubes (CNTs) for use as a matrix to confine sulfur in micropores, surface active sites, and CNT walls. There are several distinct ways of achieving this. First, melt adsorption–solvent extraction was used to immobilize sulfur in the micropores of hierarchical porous carbon. Such micropores

(less than 1 nm) have a strong adsorption potential to confine the sulfur species, and can thus act as a solvent-restricted reactor for sulfur lithiation, even in carbonate-based electrolytes. Second, a self-supporting fibrous graphene–sulfur hybrid was synthesized by a one-pot process using hydrothermal reduction and self-assembly. The surface oxygen-containing functional groups of graphene promote the distribution of sulfur nanocrystals and the tight contact of sulfur with the graphene. Third, sulfur has been encapsulated in the walls of carbon nanotubes by template-directed chemical vapor deposition and the carbon thermoreduction of sulfate. Combined with first-principles calculations, it is found that sulfur exists as short chain-like molecules ($S_{2\text{-}4}$) in sub-nm pores rather than cyclo-$S_8$ molecules. All these hybrid materials have shown high capacity, high rate, and long life.

Dr. Zhou has also developed a sandwich structure and a three-dimensional graphene framework that assist in achieving high-capacity, high-power, and long-life lithium–sulfur batteries. He designed a unique sandwich structure with pure sulfur between two graphene membranes, one of which is used as a current collector to replace commercial Al foil with sulfur coated on it as the active material, and the other is coated on a commercial polymer separator. In order to improve the S/C ratio, a graphene-foam-based flexible electrode was prepared by a simple yet effective method. This graphene foam may also be promising as a support for lithium iron phosphate, lithium titanium oxide, silicon, and other electrode materials in improving the energy density of the batteries. Moreover, Dr. Zhou is the first researcher to use three-dimensional X-ray microtomography to explore sulfur diffusion during cycling.

He has demonstrated that the fabrication of sulfur/carbon hybrid materials and electrodes is an efficient way to obtain high-performance lithium–sulfur batteries. The results obtained lay the groundwork for the design and development of high-capacity, high-power, and long-life lithium–sulfur batteries. It is expected that the industrial production and application of these batteries will be realised in the near future.

Shenyang, People's Republic of China — Prof. Hui-Ming Cheng
October 2016 — Prof. Feng Li

**Parts of this thesis have been published in the following journal articles:**

**[A1] Guangmin Zhou,** Songfeng Pei, Lu Li, Da-Wei Wang, Shaogang Wang, Kun Huang, Li-Chang Yin, Feng Li, Hui-Ming Cheng. A graphene-pure sulphur sandwich structure for ultrafast, long-life lithium-sulphur batteries. ***Advanced Materials,*** 2014, 26, 625–631.

**[A2] Guangmin Zhou,** Li-Chang Yin, Da-Wei Wang, Lu Li, Songfeng Pei, Ian R. Gentle, Feng Li, and Hui-Ming Cheng, Fibrous hybrid of graphene and sulfur nanocrystals for high performance lithium-sulfur batteries. ***ACS Nano,*** 2013, 7, 5367–5375.

**[A3] Guangmin Zhou,** Da-Wei Wang, Feng Li, Peng-Xiang Hou, Li-Chang Yin, Chang Liu, Gaoqing (Max)Lu, Gentle, Ian, Hui-Ming Cheng. A flexible nanostructured sulphur-carbon nanotube cathode with high rate performance for Li-S batteries. ***Energy & Environmental Science,*** 2012, 5, 8901–8906.

**[A4] Guangmin Zhou,** Lu Li, Chaoqun Ma, Shaogang Wang, Ying Shi, Nikhil Koratkar, Wencai Ren, Feng Li, Hui-Ming Cheng. A graphene foam electrode with high sulfur loading for flexible and high energy Li-S batteries. ***Nano Energy,*** 2015, 11, 356–365.

**[A5] Guangmin Zhou,** Feng Li, Hui-Ming Cheng. Progress in flexible lithium batteries and future prospects, ***Energy & Environmental Science,*** 2014, 7, 1307–1338.

**[A6]** Da-Wei Wang[#], **Guangmin Zhou[#]** (Co-first author), Feng Li, Kuang-Hsu, Wu, Gaoqing (Max) Lu, Hui-Ming Cheng, Gentle, Ian. A micro-mesoporous carbon with graphitic structure for high-rate stable sulfur cathode in carbonate solvent-based Li-S batteries. ***Physical Chemistry Chemical Physics***, 2012, 14, 8703–8710.

# Acknowledgements

I would like to express my grateful appreciation to my two respectable supervisors, Profs. Hui-Ming Cheng and Feng Li, who led me into the palace of science and allowed me the freedom to pursue what I feel interested in. Professor Cheng has great passion and motivation in the research, and he not only guides me how to create innovative ideas in the scientific aspect but also encourages me to think more simple yet effective strategies for practical applications. His continuous encouragement and support help me reach a level that I can never imagine.

I would like to convey my special gratitude to Prof. Feng Li, who is my supervisor since I came for undergraduate thesis project. During the past 6 years, he provided me valuable instructions and suggestions referring to my life, study, work, and every aspect I felt confused or encountered difficulties. I cannot estimate the time we discuss, the versions of manuscript revision we have, and could not develop my research work successfully without his insightful guidance. His open, encouraging, and inspiring training helps me quickly develop my independent research capability and makes me fall in love with research.

I would like to show my gratitude to Dr. Da-Wei Wang, who is my mentor when I entered the energy storage field. He provided all kinds of suggestions and help to me to overcome the difficulties I faced at my initial stage. We had a lot of fruitful discussions, and cooperated many projects that were really exciting.

I want to show my appreciation to my great collaborators: Prof. Peng-Xiang Hou, Mr. Chao Shi, and Wenshan Li provided me large amounts of carbon nanotubes and helpful discussions; Dr. Li-Chang Yin and Mr. Wei Chen, we had a lot of discussion and collaborations in the theoretical calculations, they expanded my knowledge and deepened my understanding on the experimental results; Dr. Songfeng Pei, Mr. Kun Huang, and Mr. Chaoqun Ma offered me the skill in fabricating high-quality graphene-based materials; Dr. Shaogang Wang spent a lot of time in discussing with me and constructing the 3D X-ray tomography images that are helpful for us to publish the high-quality papers. I have pleasant cooperations with all of you.

I am grateful to Dr. Zhe Ying and Dr. Lei Wen, who have provided me assistance in building the lithium rechargeable batteries and mastering the skill in electrochemical test. I thank Prof. Wencai Ren who gave me a lot of suggestions in graphene and expanded my vision in this area. Special thanks to Dr. Haofeng Lu, Dr. Zhong-Shuai Wu, Dr. Dai-Ming Tang, Dr. Bilu Liu, and Dr. Shi-Sheng Li, who helped me a lot when I entered our group and began doing experiments. I thank Dr. Xuyi Shan, we worked together on the new direction of Li–S battery system in our group. I would like to show my special gratitude to Ms. Lu Li, for her great contributions in helping me finish many interesting experiments. We discussed a lot, conquered the experimental troubles, and enjoyed the happy time after the successful experiments and acceptance of our work.

I would like to show my special thanks to Dr. Zhenhua Sun, Ms. Ying Shi, Mr. Renshen Song, Dr. Na Li, Dr. Zhe Weng, Dr. Wanjing Yu, Chengming Liu, Man Gao, Ruopian Fang, Jing Chen, Yuzuo Wang, Bin Yan, and Guangjian Hu. We are in the same energy storage subgroups and had a lot of fruitful discussions. Dr. Ping Niu, Dr. Lili Zhang, Dr. Wenbin Liu, and Dr. Chaoren Liu, we joined advanced carbon divisions together and fighted together for many years. I thank Ms. Lida Wang, Mr. Zhaoyu Wang, Mr. Ning Kang, Mr. Baoquan Wang, Ms. Ning Xu, and Ms. Chongxiao Zhang who supported me to book the chemicals and experimental setups that ensured that the experiments went smoothly.

I thank the support from all the members in the advanced carbon materials division. Professors. Chang Liu, Hongtao Cong, Shuo Bai, Gang Liu, You Zeng and Dongming Sun, who gave me lots of suggestions in the group discussions. I would also like to thank the teachers and administrators of the graduate school, especially Prof. Min Liu, Mr. Kang Pei, Ms. Ying He, Mr. Xiaobin Wang, Mr. Lirun Ji, Mr. Yang Li, and Dr. Wei Wei, for providing me with a peaceful and active environment for living and studying. As a leader in the class, I contacted frequently with all of you and you gave us infinite support and help. I thank Dr. Fengkai Yan, Dr. Qun Yang, Dr. Yang Liu, and Dr. Qingsong Pan; we worked together for our class and enjoyed the acknowledgements form the teachers and classmates. Special thanks to Dr. Zhe Geng, we fighted and helped each other for nearly ten years. I thank all my classmates for recognizing each other and the experiences we had, which will be my unforgettable memories and fortunes.

In addition, many other professors or friends out of our group and institute also gave me a lot of help and support. Special thanks to Profs. Quanhong Yang and Qiang Zhang, they gave me excellent support and encouragement throughout my Ph.D. study. I thank Prof. Haitao Fang, Prof. Chengmeng Chen, Dr. Chen Zhang, and Dr. Wei Lv; we have pleasant and effective collaborations. I thank Dr. Mengqiang Zhao, Dr. Jiaqi Huang, Mr. Xinbing Cheng, Mr. Hongjie Peng, Dr. Fugen Sun, Dr. Zhen Li, Dr. Long Qie, Dr. Yongming Sun, Dr. Bin Luo, Dr. Da Hong, Mr. Huixin Wang, Mr. Qihao Chen, and Dr. Chuankun Jia for their help and support.

I thank the support from our professional technicians in SYNL including Dr. Jun Tan, Mr. Bo Wu, Dr. Chuan-Bin Jiang, Mr. Kui-Yi Hu, Mr. Xiao-Ping Song,

Mr. Sucheng Wang, Ms. Xiaoming Lou, Ms. Yu-Zhen Sun, and Ms. Bin Zhang, who helped me a lot in various structural characterizations

For the publication of the current translated thesis, I would like to thank my editors, Dr. Wayne Hu and Dr. Dharmalingam Suresh, for their professional work, kind and patient help.

Last but not least, I want to express my deepest gratitude to my family for their infinite love and support.

Guangmin Zhou

# Contents


**1 Introduction** . . . . . 1
1.1 Introduction of Lithium–Sulfur Secondary Battery . . . . . 1
1.1.1 Cathode Materials . . . . . 3
1.1.2 Anode Materials . . . . . 13
1.1.3 Separators and Interlayers . . . . . 15
1.1.4 Electrolyte . . . . . 16
1.2 Motivations of the Thesis . . . . . 18
References . . . . . 19

**2 Revealing Localized Electrochemical Transition of Sulfur in Sub-nanometer Confinement** . . . . . 23
2.1 Research Background . . . . . 23
2.2 Design, Fabrication, and Characterization of Carbon–Sulfur Composite Cathode . . . . . 25
2.2.1 Synthesis of Hierarchical Porous Carbon (HPC) . . . . . 25
2.2.2 Synthesis of Carbon–Sulfur Composite . . . . . 26
2.2.3 Structure Characterization of the Carbon–Sulfur Composite . . . . . 26
2.2.4 Electrochemical Performance of the Carbon–Sulfur Composite Cathode . . . . . 29
2.3 Mechanism Analysis of the Pore Size Dependence of Confinement on Electrochemical Performance in Li–S Batteries . . . . . 32
2.4 Conclusion . . . . . 35
References . . . . . 35

**3 Flexible Nanostructured Sulfur–Carbon Nanotube Cathode with High-Rate Performance for Li–S Batteries** . . . . . 39
3.1 Research Background . . . . . 39
3.2 Design and Fabrication of Flexible Nanostructured S-CNT Cathode . . . . . 41

3.2.1 Synthesis of S-Containing Anodic Aluminum Oxide (AAO) Template . . . 41
3.2.2 Synthesis of S-CNTs Composites . . . 41
3.2.3 Synthesis of CNTs . . . 42
3.2.4 Fabrication of Flexible S-CNT Membranes . . . 42
3.3 Sulfur Formation Mechanism . . . 42
3.4 Characterization of S-CNTs . . . 43
3.5 Control of the Sulfur Content in the S-CNTs . . . 45
3.6 First-Principles Calculations of the Sulfur Molecules Diffusion Within the Micropores . . . 46
3.7 Synthesis, Structure, and Performance of Flexible S-CNT Electrode . . . 46
3.8 Electrochemical Performance of Flexible Nanostructured S-CNT Cathode . . . 48
3.9 Fabrication of Flexible Silicon/Graphene Anode and Assembly of Flexible Li–S Full Battery Prototype . . . 50
3.9.1 Fabrication of Flexible Silicon/Graphene Composite Film . . . 50
3.9.2 Fabrication of Flexible Prelithiated Silicon/Graphene Composite Film . . . 51
3.9.3 Assembly of Flexible Li–S Full Battery Prototype . . . 52
3.10 Conclusion . . . 53
References . . . 53

**4 Fibrous Hybrid of Graphene and Sulfur Nanocrystals for High-Performance Lithium–Sulfur Batteries** . . . 57
4.1 Research Background . . . 57
4.2 Material Fabrication and Structure . . . 58
4.2.1 Synthesis of GO . . . 58
4.2.2 Synthesis of Intercalation Exfoliated Graphene . . . 59
4.2.3 Synthesis of the Thermal Exfoliated-Reduced Graphene . . . 59
4.2.4 Preparation of G–S Hybrids . . . 59
4.2.5 Preparation of G–S Hybrids (Powder) . . . 59
4.2.6 Preparation of G–$S_{mix}$ . . . 59
4.2.7 Structure Characterization of the Composites . . . 60
4.3 Interaction Mechanism Between Oxygen-Containing Groups and Sulfur/Polysulfides . . . 65
4.4 Properties of Sulfur Nanocrystal/Graphene Composites . . . 67
4.4.1 Electrical Property and Mechanical Flexibility . . . 67
4.4.2 Electrochemical Performance . . . 68
4.5 Conclusion . . . 72
References . . . 72

**5 Graphene–Pure Sulfur Sandwich Structure for Ultrafast, Long-Life Lithium-Sulfur Batteries** . . . . . 75
5.1 Research Background . . . . . 75
5.2 Construction of Sandwich Cathode Structure . . . . . 77
5.2.1 GCC Fabrication . . . . . 77
5.2.2 Fabrication of Sulfur-Coated GCC Electrodes . . . . . 77
5.2.3 G-Separator Fabrication . . . . . 77
5.3 Structure Characterization of the Sandwich Cathode Structure . . . . . 78
5.3.1 Structure Characterization of the Graphene Powder . . . . . 78
5.3.2 Structure Feature of the GCC . . . . . 78
5.3.3 Structure Characterization of the GCC/S Cathode . . . . . 80
5.3.4 Structure Characterization of the G-Separator . . . . . 82
5.4 Electrochemical Performance of the Sandwich Cathode Structure . . . . . 83
5.5 Interaction Between Graphene and Sulfur Species in Sandwich Cathode Structure . . . . . 88
5.5.1 Function as a Current Collector . . . . . 88
5.5.2 Function as a Separator Coating Layer . . . . . 89
5.6 Conclusion . . . . . 92
References . . . . . 93

**6 A Graphene Foam Electrode with High Sulfur Loading for Flexible and High-Energy Li–S Batteries** . . . . . 95
6.1 Research Background . . . . . 95
6.2 Fabrication and Characterization of the 3D GF-Based Electrode . . . . . 96
6.2.1 Preparation of PDMS/GF . . . . . 96
6.2.2 Preparation of S-PDMS/GF Electrode . . . . . 96
6.2.3 Structure Characterization of the S-PDMS/GF Electrode . . . . . 97
6.3 Mechanical Properties of the 3D GF-Based Electrode . . . . . 100
6.4 Electrochemical Performance of the 3D GF-Based Sulfur Electrode . . . . . 101
6.5 Areal Capacity of the 3D GF-Based Sulfur Electrode . . . . . 105
6.6 Conclusion . . . . . 109
References . . . . . 110

**7 Conclusions and Perspective** . . . . . 113
7.1 Main Conclusion and Innovations . . . . . 113
7.2 Perspective for Future Works . . . . . 115

# About the Author

**Guangmin Zhou** got his Ph.D. from Institute of Metal Research (IMR), Chinese Academy of Sciences in 2014 under the supervision of Profs. Hui-Ming Cheng and Feng Li, and then worked as a postdoc in UT Austin with Prof. Manthiram for one year. Now he is a postdoc fellow in Stanford University with Prof. Yi Cui. His research mainly focuses on the advanced carbon-based (porous carbon, graphene, carbon nanotubes) composites for energy storage: synthesis, electrochemical properties, and mechanisms. Zhou has published more than 50 articles in peer-reviewed scientific journals, and first-authored 21 papers published in Nature Communications, Advanced Materials, Advanced Energy Materials, ACS Nano, Energy & Environmental Science, Advanced Functional Materials, Chemistry of Materials, Nano Energy, etc. His original work has had a broad influence on the field of high-energy lithium secondary batteries, where his publications have been cited 6881 times (Google Scholar), and his first-authored 21 papers have been cited over 4100 times (13 individual papers have been cited more than 100 times, and the highest cited times is 1141 times for Chemistry of Materials 2010). The paper published in Advanced Materials 2014 has been selected as one of Top 100 most influenced papers in China in 2014. Additionally, he has authored 1 book chapter (≤Graphene Science Handbook≥), 15 conference papers and posters, 10 (9 Chinese & 1 PCT) patents.

## Other Academic Awards and Honors Include

2015 Excellent Doctorate Theses Award of Chinese Academy of Sciences (CAS)
2015 Carbon Journal Prize (Only one person all over the world in 2015)
2015 Excellence in Review Award for Carbon
2014 The Special Prize of President Scholarship for Postgraduate Students of CAS
2014 SHI CHANGXU Award by IMR CAS

2014 Electrochemical Conference on Energy & Environment Poster Award Winner
2013 Sinopoly Battery Scholarship
2013 University of CAS-BHP Billiton Scholarship (25 out of ~36,000)
2013 National Scholarship for Postgraduate Students
2012 National Scholarship for Postgraduate Students
2012 The 7th International Green Energy Conference "AIP BEST poster"
2011 SHI CHANGXU Award by IMR CAS
2011 Second Prize of the International Graduate Microstructure of Material Contest

# Abbreviations

| | |
|---|---|
| AAO | Anodic aluminum oxide |
| CNT | Carbon nanotube |
| CV | Cyclic voltammetry |
| CVD | Chemical vapor deposition |
| DEC | Diethyl carbonate |
| DFT | Density functional theory |
| DME | 1,2-dimethoxyethane |
| DOL | 1,3-dioxolane |
| EC | Ethylene carbonate |
| EDS | Energy-dispersive X-ray spectroscopy |
| EELS | Electron energy loss spectroscopy |
| EIS | Electrochemical impedance spectroscopy |
| GF | Graphene foam |
| GO | Graphene oxide |
| HF | Hydrofluoric acid |
| HRTEM | High-resolution transmission electron microscopy |
| LED | Light-emitting diode |
| MWCNT | Multi-walled carbon nanotube |
| NMP | N-methyl-2-pyrrolidone |
| PAN | Polyacrylonitrile |
| PANI | Polyaniline |
| PC | Propylene carbonate |
| PDMS | Poly(dimethyl siloxane) |
| PEDOT | Poly(3,4-(ethylenedioxy)thiophene) |
| PEG | Polyethylene glycol |
| PEO | Poly(ethylene oxide) |
| PP | Polypropylene |
| PPY | Polypyrrole |
| PVDF | Polyvinylidene fluoride |
| SEI | Solid–electrolyte interphase |

| | |
|---|---|
| SEM | Scanning electron microscopy |
| STEM | Scanning transmission electron microscope |
| SWCNT | Single-walled carbon nanotube |
| TEGDME | Tetra(ethylene glycol) dimethyl ether |
| TEM | Transmission electron microscopy |
| XPS | X-ray photoelectron spectroscopy |
| XRD | X-ray diffraction |
| XRM | X-ray microtomography |

# Chapter 1
# Introduction

## 1.1 Introduction of Lithium–Sulfur Secondary Battery

Lithium-ion batteries (LIBs) play a dominant role in portable electronic devices for decades due to their high performance compared to the other battery systems [1, 2]. However, the increased demand for electric vehicles and large-scale smart grid stringently requires batteries with high energy density, low cost, and long cycle life [3]. The current main challenge is the capacity mismatch between the cathode and anode, which makes LIB approach its theoretical energy density limits [4, 5]. The relatively lagged progress on cathodes (capacity usually lower than 200 mAh $g^{-1}$) becomes a barrier in further improving the energy density of LIBs, which has triggered the exploration of new electrochemical energy storage systems (Fig. 1.1), such as the lithium–sulfur (Li–S) batteries with a high theoretical capacity of 1675 mAh $g^{-1}$ and energy density of 2600 Wh $kg^{-1}$ [6, 7]. The energy density is five times higher compared to the commercial LIBs with $LiCoO_2$/graphite system (387 Wh $kg^{-1}$) [3, 7, 8]. Sulfur is also abundant, nontoxic, and inexpensive. Despite the considerable advantages of Li–S batteries, several problems prevent it from practical applications: (1) the insulating characteristic of sulfur ($5 \times 10^{-30}$ S $cm^{-1}$, 20 orders lower compared to the commonly used transition metal oxide-based cathodes) and its discharge products ($Li_2S$), leading to a low utilization of active material [9]; (2) large volumetric expansion/shrinkage (80%) during discharge/charge due to the different densities of sulfur (2.03 g $cm^{-3}$) and lithium sulfides (1.67 g $cm^{-3}$), resulting in an instability of the electrode structure; (3) the soluble polysulfide intermediates ($Li_2S_x$, $3 \leq x \leq 8$) in the organic liquid electrolyte during the cycle process bring about the polysulfide "shuttle effect," which leads to irreversible capacity loss and corrosion on the lithium–metal anode [4, 10, 11].

The rhombic stacking of $S_8$ is the stable room-temperature form, which consists of eight sulfur atoms constructing a crown structure. The redox chemistry of sulfur in the cathode relies on a solid (cyclo-$S_8$)–liquid (lithium polysulfide)–solid



G. Zhou, *Design, Fabrication and Electrochemical Performance of Nanostructured Carbon Based Materials for High-Energy Lithium–Sulfur Batteries*, Springer Theses,
DOI 10.1007/978-981-10-3406-0_1

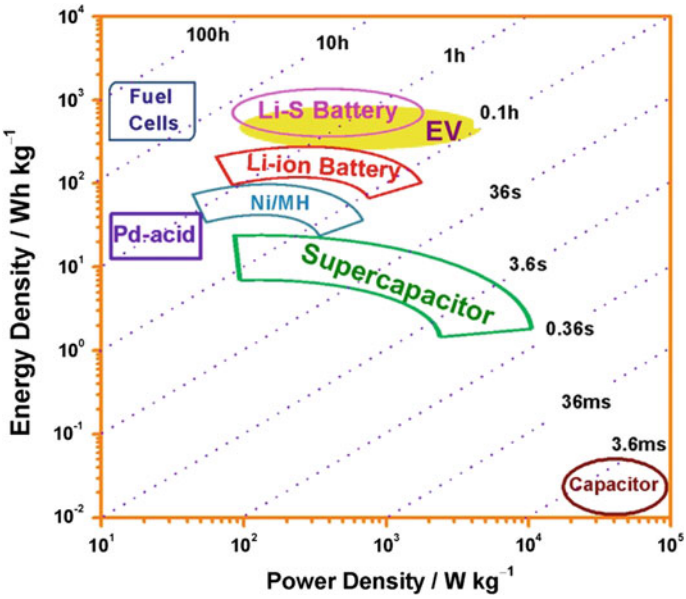


**Fig. 1.1** Comparison of different energy storage devices in terms of power and energy density

($Li_2S_2$/$Li_2S$) reaction with a transformation of $S_8$ + 16 $Li^+$ + 16 $e^-$ ↔ 8 $Li_2S$. This is a two-electron conversion reaction through breaking the S–S bonds and forming a series of sulfur species such as $Li_2S_8$, $Li_2S_6$, $Li_2S_4$, $Li_2S_3$, $Li_2S_2$, and $Li_2S$. During the following charge, $Li_2S$ is converted into intermediate lithium polysulfides and finally to $S_8$ resulting in a reversible cycle (Fig. 1.2) [10]. In order to address the above issues and realize the application of high energy density and long cycling life Li–S batteries, people investigate all the key components in Li–S batteries and great

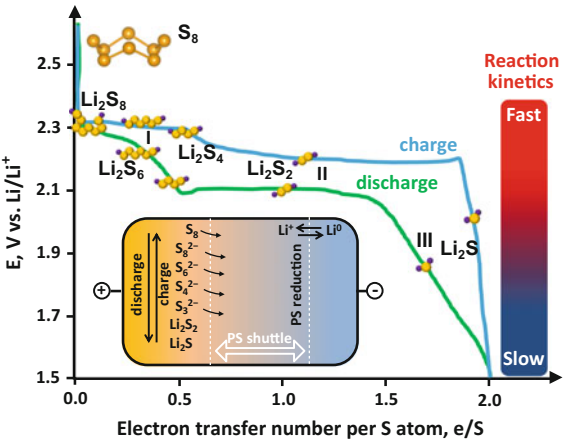


**Fig. 1.2** Typical charge–discharge curves in the Li–S battery, inset: schematic illustration of the polysulfide shuttle effect in the Li–S battery. Reprinted with permission from Ref. [10]. Copyright 2013, Royal Society of Chemistry

progress has been made in this field. For example, Sion Power adopts Li–S batteries as energy storage system and uses solar cell to charge the battery in the daytime and provide electricity through Li–S batteries in the night. As a record, the Li–S battery can power the unmanned plane for continuous 336 h (14 days). Here we briefly summarize the recent advances in Li–S batteries, including the sulfur-based cathode, lithium metal anode, separators and electrolytes, and new designs of Li–S batteries with a metallic Li-free anode.

## *1.1.1 Cathode Materials*

Currently the most commonly adopted strategy in designing sulfur cathodes includes sulfur–carbon composites, sulfur–conducting polymer composites, sulfur/metal oxide composites, and lithium sulfide materials, which will be briefly introduced below.

### 1.1.1.1 Sulfur–Carbon Composites

All kinds of sulfur–carbon composites take the advantages of the conductivity of carbon to overcome the insulating property of sulfur. Abundant sulfur could be loaded on the pores of large surface area carbon-based materials. The pore structure of carbon could provide enough space to accommodate the volume change of sulfur during charge and discharge processes, and mitigate the dissolution of polysulfide intermediates, so the utilization of sulfur and cycle performance can be improved. At the same time, the porous structure could enhance the reaction kinetics by providing the electrolyte ion transport channels. Abundant oxygen-/nitrogen-containing functional groups on the surface of carbon could trap polysulfides by strong surface interactions. Therefore, the sulfur–carbon composites have attracted wide attention.

Nazar's group has fabricated CMK-3/S composite with 70 wt% sulfur content by a melt-diffusion strategy [12]. As shown in Fig. 1.3a, sulfur has been trapped into the long-range order channels of mesoporous CMK-3 (pore diameter: 3–4 nm). The nanostructured composite exhibits an impressive initial discharge capacity of 1005 mAh $g^{-1}$ at 168 mA $g^{-1}$ (all of the capacity values in this article are calculated on the basis of sulfur mass unless otherwise specified). After 20 cycles, the capacity still maintained at about 800 mAh $g^{-1}$. To further trap the highly polar polysulfide species, they adopted polyethylene glycol (PEG) to functionalize the hydrophilicity of the carbon external surface after sulfur infiltration. The initial discharge capacity increased to 1320 mAh $g^{-1}$, and after 20 cycles, the capacity is stabilized at 1100 mAh $g^{-1}$ [12]. Liang, etc. reported a kind of bimodal porous carbon with 7.3 nm mesopores and less than 2 nm mesopores through a soft-template synthesis method combining with the potassium hydroxide activation, as shown in Fig. 1.3b [13]. Elemental sulfur has been loaded to the micropores

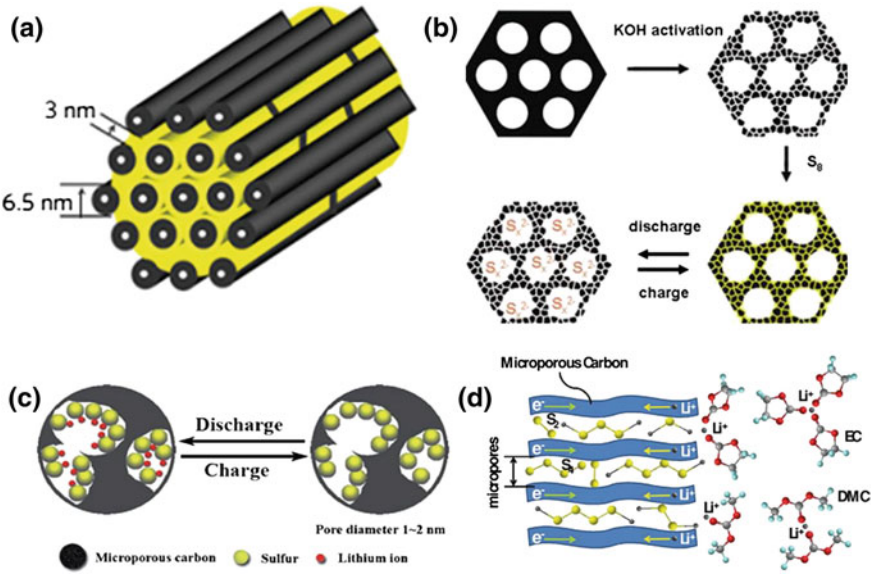


**Fig. 1.3** **a** Schematic of sulfur confined in the interconnected pore structure of mesoporous carbon. Reprinted with permission from Macmillan Publishers Ltd.: Ref. [12]. Copyright 2009. **b** Illustration of the sulfur/carbon composite cathode material using a bimodal porous carbon as the support. Reprinted with permission from Ref. [13]. Copyright 2009, American Chemical Society. **c** Schematic of the constrained electrochemical reaction process inside the micropores of a sulfur/carbon composite cathode. Reprinted with permission from Ref. [15]. Copyright 2010, Royal Society of Chemistry. **d** Schematic of the lithiation process in a microporous carbon cathode in carbonate-based electrolyte. Reprinted from Ref. [16] by permission of John Wiley & Sons Ltd.

through a solution infiltration method. When the sulfur loading was lower than 37.1 wt%, sulfur mainly existed in the micropores and small mesopores (<3 nm), which are beneficial for the sulfur confinement. However, when sulfur loading was higher than 37.1 wt%, extra sulfur mainly exists in the large mesopores, which could offer the channels for lithium-ion transportation. When sulfur loading was reduced to only 11.7 wt%, the capacity was maintained at 780 mAh $g^{-1}$ after 50 cycles, indicating the cyclic performance and sulfur loading need to be further enhanced.

The above results suggest that mesoporous carbon could store sulfur and offer the facile transport paths for Li ions while the microporous structure exhibits more powerful capability in trapping sulfur. However, the polysulfide dissolution still exists in the above systems. When the diameter of the micropore is lower than that of $S_8$ ($\sim$0.7 nm), the chain-like sulfur molecules in the carbon micropores could not transform to the large $S_8$ rings, but maintain as $S_{2-4}$ molecules, which leads to the reduction process starting from $S_{2-4}$ to $S_2$ instead of the transition from $S_8$ to $S_{2-4}$ and eliminating the shuttle effect of lithium polysulfides [14]. For example, Gao's group prepared a sulfur–carbon composite spheres by encapsulating sulfur into micropores of the carbon spheres. Sublimed sulfur and carbon spheres were mixed

and thermal treated at 155 °C followed by vaporizing superfluous sulfur on the outer surface of the carbon spheres. Due to the small diameter of micropore (0.7 nm), sulfur exists as a small molecule and highly dispersed state inside the carbon spheres, which effectively restricts the diffusion of polysulfides and ensures the good electric conductivity of the composite cathode (Fig. 1.3c). This sulfur–carbon sphere cathode presents a long cyclic stability up to 500 cycles with a capacity retention over 80% at current density of 400 mA $g^{-1}$ [15]. Guo's group also reported a metastable sulfur allotropes $S_{2-4}$ confined in micropores of carbon. These confined small $S_{2-4}$ molecules exhibit a high Li electroactivity and a novel electrochemical behavior with a single output plateau at $\sim$1.9 V, in contrast to the common cyclo-$S_8$, and can essentially solve the critical problems of polysulfide dissolution in conventional Li–S batteries [14]. The as-obtained $S_{2-4}$ molecule–based cathode shows a high specific capacity of 1670 mAh $g^{-1}$, an impressive cycling stability of 1149 mAh $g^{-1}$ after 200 cycles, and a favorable high-rate capability of 800 mAh $g^{-1}$ at 5 C. Recently, Huang group further investigated the electrochemical mechanism of the $S_{2-4}$ cathode confined in a highly ordered microporous carbon matrix in various electrolytes (carbonate and ether electrolytes) through combined experimental results and theoretical calculation. If the micropores of carbon are small enough to prevent the penetration of the solvent molecules (e.g., EC: 0.574 nm, DMC: 0.796 nm), the lithiation/delithiation for $S_{2-4}$ occurs as a solid–solid process (Fig. 1.3d) [10, 16]. The irreversible chemical reactions between the polysulfides and carbonates and the dissolution of the polysulfides into the ethers can be effectively avoided due to the steric hindrance. The sulfur cathode based on this strategy exhibits excellent rate capability and cycling stability. However, microporous carbon faces the challenge of small pore volume and low sulfur loading, which impedes the realization of high energy density. Further optimization of mesopore–micropore ratio is also required for achieving high-performance Li–S batteries.

The excellent electrical conductivity, large specific surface area, and flexible two-dimensional structure of graphene makes it a promising encapsulation material for sulfur cathodes by forming conductive network, buffering the volume change, and improving the electrochemical activity of sulfur. Besides, the easy functionalization of graphene could also establish strong chemical interaction between graphene and polysulfides to stabilize sulfur cathodes. Dai's group has reported a graphene/sulfur composite by wrapping PEG-coated sulfur particles with mildly oxidized graphene oxide sheets decorated by carbon black nanoparticles, as shown in Fig. 1.4a. Graphene sheets and carbon black could enhance the conductivity of sulfur and PEG could effectively accommodate volume expansion of the coated sulfur particles during charge and discharge processes. The coating layers consisting of PEG and graphene are helpful to trap soluble polysulfide intermediates; thereby, a high and stable specific capacity has been achieved [17]. The initial discharge capacity is 750 mAh $g^{-1}$ at 0.2 C (1 C = 1672 mA $g^{-1}$); and after 100 cycles, the value has been kept at around 500 mAh $g^{-1}$. Besides this core–shell structure, the performance of Li–S batteries has also been improved by the

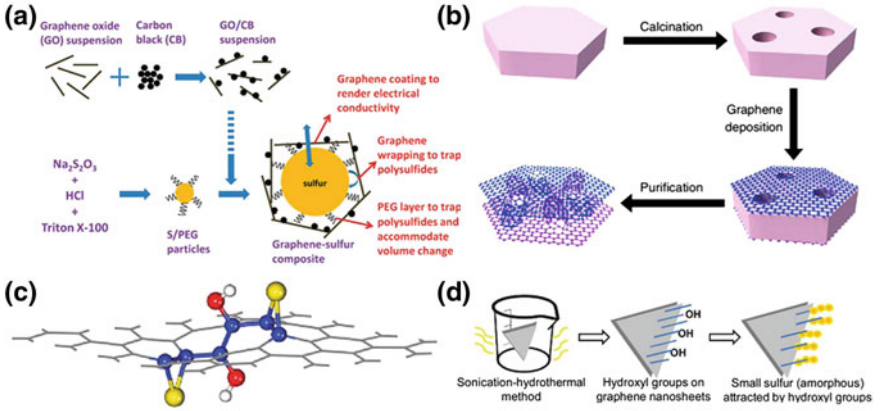


**Fig. 1.4** **a** Schematics of the synthesis steps for a PEG-S/graphene composite. Reprinted with permission from Ref. [17]. Copyright 2011, American Chemical Society. **b** Scheme for the synthesis of unstacked graphene. Reprinted with permission from Macmillan Publishers Ltd.: Ref. [24]. Copyright 2013. **c** Representative pattern of GO immobilizing sulfur. Reprinted with permission from Ref. [25]. Copyright 2011, American Chemical Society. **d** Schematic of the synthesis process of the hydroxylated graphene/S nanocomposite. Reprinted from Ref. [26] by permission of John Wiley & Sons Ltd.

sandwich-type graphene/sulfur composite [18], graphene/sulfur capsule structure [19], "fish in net" structure [20], and gradient graphene/sulfur structure [21].

However, due to the easy aggregation and stacking of graphene, it compromises their advantages in the applications of Li–S batteries. Zhao et al. proposed a novel graphene/single-walled carbon nanotube (G/SWCNT) hybrid by placing SWCNTs among graphene planes through covalent C–C bonding under the catalysis growth on layered double hydroxide [22]. After the sulfur immersing, the obtained G/SWCNTs cathode exhibits excellent performance in Li–S batteries with a capacity as high as 650 mAh $g^{-1}$ after 100 cycles even at a high current rate of 5 C due to the construction of a high electrical conductive pathway made of SWCNT and graphene [22]. On the basis of chemical vapor deposition (CVD) of graphene/carbon nanotube hybrids and further chemical activation, nanoarchitectured graphene/CNT@porous carbon was designed to trap lithium polysulfides in Li–S batteries [23]. Recently, this group also developed an intrinsically unstacked double-layer graphene via a template (MgAl layered double oxides)-directed CVD method. The stacking of graphene has been effectively avoided [24], as shown in Fig. 1.4b. This un-stacked double-layer graphene shows a high specific surface area of 1628 $m^2$ $g^{-1}$ and a large pore volume of 2.0 $cm^3$ $g^{-1}$. When this material was used for Li–S batteries, the reversible capacity could be up to 713 mAh $g^{-1}$ at 10 C, suggesting its excellent high-rate performance. After 1000 cycles at 5 C, the reversible capacity still retained ca. 530 mAh $g^{-1}$ [24].

Surface chemistry is another important factor which could affect the performance of Li–S batteries. Zhang et al. coated sulfur on the surface of graphene oxide

(GO) sheets by a simple chemical reaction–deposition strategy and a subsequent low-temperature thermal treatment method [25]. The simulation results and X-ray absorption spectroscopy measurement have suggested the functional groups on the GO surface enhance the interactions between the carbon and sulfur species (Fig. 1.4c), and confine the dissolution of polysulfides thus avoiding "shuttle effect" effectively. A stable cycling performance with a high reversible capacity (954 mAh $g^{-1}$) at 0.1 C (1 C = 1675 mA $g^{-1}$) after 50 cycles has been achieved. Manthiram group synthesized a hydroxylated graphene with the aid of ultrasonication during the hydrothermal process [26]. The hydroxyl groups in graphene could induce heterogeneous nucleation of amorphous sulfur nanoparticles and make them distribute uniformly on the graphene surface. Besides, the hydroxyl groups could interact with the sulfur-containing compounds and render the graphene/sulfur electrode to exhibit high-rate and stable performance (Fig. 1.4d) [26]. With the help of the rich functional groups on the GO, Yang's group demonstrated a graphene/sulfur hybrid could be obtained by the effective reduction of GO and the removal of $H_2S$ simultaneously. Pollutant $H_2S$ gas could environmentally convert into a promising cathode for high-performance Li–S batteries with 950 mAh $g^{-1}$ at 0.2 A $g^{-1}$ [27].

One-dimensional carbon nanotubes (CNTs) have been applied to construct various kinds of sulfur/CNT cathodes in Li–S batteries to improve the performance, because of their unique tube structures, high aspect ratios, and excellent conductivity; for example, sulfur-coated CNTs coaxial structures [28, 29], self-weaving sulfur–carbon composite [30], and vertical aligned CNTs/sulfur composite [31–33]. However, these traditional melting or liquid infiltration methods would leave some residual sulfur exposing outside of the CNTs, which will cause sulfur dissolving into the electrolyte easily during electrochemical reactions. Cui et al. adopted a kind of hollow carbon nanofiber derived from anodic aluminum oxide (AAO) templates to encapsulate sulfur [34]. AAO template could facilitate sulfur infusion into the hollow fibers and avoid sulfur residues remained on the exterior of carbon wall. The hollow chamber of carbon nanofiber could confine sulfur, reduce volumetric expansion, and effectively increase the utilization of sulfur. Thin carbon wall also accelerates rapid transport of electrons and Li ions, which helps to realize a high specific capacity of about 730 mAh $g^{-1}$ after 150 cycles at 0.2 C rate [34]. Wang et al. also synthesized disordered CNTs using AAO membranes as the template [35]. After dropping sulfur-dissolved $CS_2$ solution on the CNTs, which was vacuum-sealed and heated, sulfur successfully impregnated into disordered CNTs. This strategy avoids the direct contact between sulfur and electrolyte, mitigating the polysulfide shuttle effect. After being heated at 500 °C, this sulfur/disordered CNT electrode has better stability with 72.9% capacity retention after 100 cycles at a current density of 200 mA $g^{-1}$ compared with the sample heated at 160 °C. However, two traditional discharge plateaus changed into one potential plateau at 2.05 V, followed by a slope-shaped curve. New peaks also appeared in the XRD pattern of the sample heated at 500 °C, which could not be identified as any known compound, suggesting the reaction and bond formation between sulfur and carbon [35].

#### 1.1.1.2 Sulfur-Conducting Polymer Composites

The aforementioned carbon coating techniques, such as CVD coating of carbon [34, 35], usually require thermal treatment at an elevated temperature to increase the electronic conductivity of the coating layer [36]. However, as the sublimation temperature of sulfur is low, the direct coating must be carried out at low temperature, which inevitably limits the number of suitable synthetic techniques and materials [37]. Since polymers can be synthesized at low temperatures (below 100 °C) and well dispersed in the solution for realizing sulfur coating [4], a variety of conducting polymer–sulfur hybrids have been developed. For example, polyacrylonitrile (PAN) [38], polypyrrole (PPY) [39], polyaniline (PANI) [40], poly (3,4-(ethylenedioxy)thiophene) (PEDOT) [41], etc. have been adopted to mitigate the dissolution of polysulfides, improve the electrical conductivity, and accommodate the volume variation of sulfur during repeated charging/discharging processes. Liu's group proposed to use self-assembled PANI nanotubes as a sulfur encapsulation matrix [40]. The PANI nanotubes were treated at 280 °C with sulfur, which resulted in a partial reaction of sulfur with the polymer to form a 3D, cross-linked, structurally stable S-PANI composite [40], as shown in Fig. 1.5a. The PANI backbones are interconnected with inter- and/or intrachain disulfide bonds. This S-PANI polymer molecular framework provides strong physical and chemical confinement to the elemental sulfur and the resident polysulfide, which leads to superior cycle stability and rate capability. The composite cathode could retain a discharge capacity of 568 mAh $g^{-1}$ after 100 cycles at 1 C rate and a discharge capacity of 432 mAh $g^{-1}$ was obtained after long-term cycling of 500 cycles, which corresponds to a 76% capacity retention (Fig. 1.5b). Chen et al. reported a membrane-assisted precipitation technique to synthesize ultrafine sulfur nanoparticles with diameter of 10–20 nm, and then coated with a conducting PEDOT to form S-PEDOT core–shell nanoparticles (Fig. 1.5c) [42]. The small-sized sulfur particles facilitate the electrical conduction and improve sulfur utilization. The encapsulation of conducting PEDOT shell restricts the polysulfides diffusion, alleviates self-discharging and the shuttle effect, and thus enhances the cycling stability. The resulted S-PEDOT core–shell nanoparticles show initial discharge capacity of 1117 mAh $g^{-1}$ and a stable capacity of 930 mAh $g^{-1}$ after 50 cycles at a current density of 400 mA $g^{-1}$ [42]. Although the sulfur-conducting polymer composites can greatly improve the electrochemical performance of sulfur cathode, the conductivity of conducting polymer is inferior compared with carbon materials, resulting in a relative low sulfur loading (usually lower than 70 wt%) with decreased energy density. Therefore, the electrical conductivity of the polymer shell should be further improved toward high-rate and high energy applications.

#### 1.1.1.3 Sulfur/Metal Oxide Composite

Due to the high surface area and strong polysulfide adsorption capability, nanosized metal oxides are used as functional absorbents or coating layers to suppress

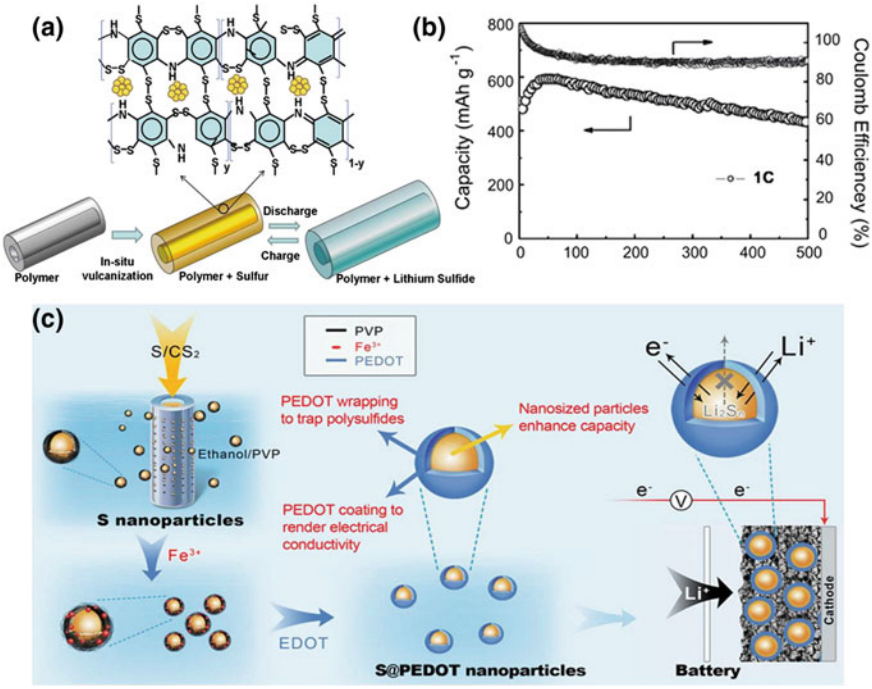


**Fig. 1.5** **a** Schematics of the construction and discharge-charge process of the S/PANI nanotube composite. **b** Cycling performance and Coulombic efficiency of the S/PANI electrode up to 500 cycles at 1 C rate. Reprinted from Ref. [40] by permission of John Wiley & Sons Ltd. **c** Schematics of the preparation of S/PEDOT core/shell nanoparticles and their application as cathode materials for Li–S batteries. Reprinted with permission from Macmillan Publishers Ltd.: Ref. [42]. Copyright 2013

polysulfide shuttling in Li–S batteries through their chemisorption effect toward polysulfide species. These metal oxides in the composites help disperse the sulfur and avoid their agglomeration. For example, some metal oxides (such as $Al_2O_3$ [43], $TiO_2$ [44], $SiO_2$ [45], $La_2O_3$ [46, 47], and $Mg_{0.6}Ni_{0.4}O$ [48]) as absorbents have proven to be highly effective at on-site adsorbing of lithium polysulfides and improving the long-term cyclic ability of Li–S batteries. In addition, some metal oxides play a critical role in catalyzing the reduction of sulfur to $Li_2S$ and oxidation of $Li_2S$ back to sulfur during battery discharging/charging, which are crucial steps to realize high-capacity and Columbic efficiency. For instance, Song et al. synthesized nanosized $Mg_{0.6}Ni_{0.4}O$ powders by the sol–gel method and added them to the sulfur cathode [48]. It was found that the $Mg_{0.6}Ni_{0.4}O$ powders used as an additive in sulfur cathodes effectively retained the polysulfides in the cathode and increased the porosity of the sulfur cathode and rate capability. Through adsorbing the polysulfides within the cathode, $Mg_{0.6}Ni_{0.4}O$ additives prevented the shuttle effect of the Li–S battery. As a result, the initial charge–discharge capacity

increased from 741 (without additives) to 1185 mAh $g^{-1}$ (with additives) and the cyclic stability of the cell improved from 76% of the initial discharge capacity to 85% at the 50th cycle after the addition of nanosized $Mg_{0.6}Ni_{0.4}O$ particles [48]. Ji et al. proposed a concept to mitigate the above problems, which relies on the design principles of drug delivery [45]. The strategy employs a porous silica embedded within the carbon–sulfur composite that not only absorbs the polysulfides through weak binding, but also permits their reversible desorption and release (Fig. 1.6a) [45]. It functions as an internal polysulfide reservoir during the reversible electrochemical process to produce long-term stability with improved Coulombic efficiency. A discharge capacity above 650 mAh $g^{-1}$ is steadily maintained after 40 cycles at 0.2 C with the Coulombic efficiency above 95%. Recently, Cui's group demonstrates the design of a sulfur–$TiO_2$ yolk–shell nanoarchitecture for stable cycling over long charge/discharge cycles. The yolk–shell structure is prepared by hydrolysis of sulfur with titanium precursor and partially dissolved by toluene, and the size is about several hundred nanometers with void space (Fig. 1.6b) [49]. The advantage of the yolk–shell morphology lies in the presence of internal void space to accommodate the large volumetric expansion of sulfur during lithiation, thus preserving the structural integrity of the shell to minimize polysulfide dissolution. The battery with the yolk–shell design demonstrates an initial discharge capacity of 1030 mAh $g^{-1}$, and the capacity retention was found to be 67% after 1000 cycles, corresponding to a small capacity decay of 0.033% per cycle, which is one of the best performances reported (Fig. 1.6c). In comparison with bare sulfur and sulfur–$TiO_2$ core–shell nanoparticles, the yolk–shell nanostructures are found to exhibit the highest capacity retention owing to the effectiveness of the intact $TiO_2$ shell in limiting polysulfide dissolution. However, the non-conductive characteristic of $TiO_2$ inevitably compromises the rate capability of the sulfur cathode. The precise control of the $TiO_2$ thickness and the addition of conductive carbon materials are therefore required. The combination of metal oxides with conducting carbon or polymer is a promising approach worth exploration. The treatment of $TiO_2$ under high temperature with $H_2$ gas to form conductive $Ti_4O_7$ phase and produce more unsaturated Ti atoms to chemically bind with sulfur species [6, 50] is another strategy to further lift the electrochemical performance.

#### 1.1.1.4 Lithium Sulfide Materials

In Li–S batteries, sulfur should be paired with a lithium metal anode which faces another challenge for the formation of lithium dendrites caused by the non-uniform deposition of lithium. These dendrites can eventually pierce the separator and lead to short-circuiting within the cell, causing serious safety concerns. Meanwhile, metallic lithium has high activity, which can easily react with electrolyte, causing the depletion of lithium and electrolyte. Therefore, excess lithium source and electrolyte amount are needed, leading to decreased specific and volumetric energy density. Replacing sulfur with lithium sulfide ($Li_2S$) is a promising strategy to address the above challenges. The theoretical capacity of $Li_2S$ (1166 mAh $g^{-1}$) is

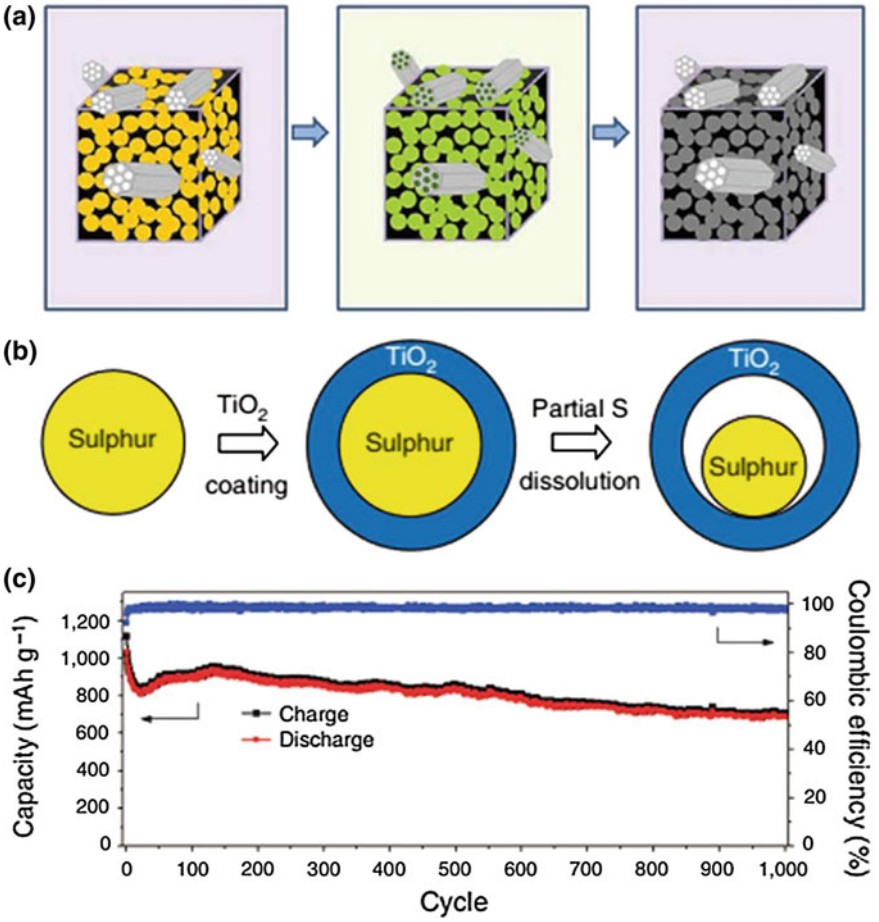


**Fig. 1.6** **a** Schematic of the concept of the "polysulfide reservoir" afforded by SBA-15 platelets in a sulfur electrode. Reprinted with permission from Macmillan Publishers Ltd.: Ref. [45]. Copyright 2011. **b** Schematic of the synthesis process of S-$TiO_2$ yolk–shell nanostructures. **c** Charge/discharge capacity and Coulombic efficiency of the S–$TiO_2$ yolk–shell nanostructure at 0.5 C over 1000 cycles. Reprinted with permission from Macmillan Publishers Ltd.: Ref. [49]. Copyright 2013

much higher than that of current commercial cathode materials, and the fully lithiated state (i.e., $Li_2S$ state) avoids the issue of volume expansion during charging [51–53]. Besides metallic lithium, it can be matched with other nonlithium-containing anode materials such as silicon, germanium, tin, and carbonaceous materials with more reliable safety properties [54, 55]. However, the poor electronic and ionic conductivity of $Li_2S$ ($10^{-13}$ S $cm^{-1}$ at room temperature) as well as the polysulfide shuttle effect are still unsolved issues, resulting in poor cycling stability and low rate capacity.

Many efforts have been made to solve these issues by designing conductive coating layers or improving the contact between $Li_2S$ and electrical conductors. For example, Scrosati et al. employed low-energy ball milling to mix commercial $Li_2S$ powder with carbon as cathode ($Li_2S$/C), selecting a high-capacity tin/carbon nanocomposite as the anode material alternative to lithium metal, combined with gel electrolyte to assemble Sn/C//$Li_2S$/C rechargeable battery (Fig. 1.7a) [55]. The strategy proposed benefits from an entirely electrode and electrolyte configuration, which is effective in controlling the polysulfide dissolution, resulting in good cycling stability. This novel tin–lithium sulfide battery demonstrates a capacity of about 900 mAh $g^{-1}$ (based on the mass of $Li_2S$) after 30 cycles at 1/20 C and provides a specific energy on the order of 1100 Wh $kg^{-1}$, significantly higher than conventional liquid electrolyte-based batteries. Cui's group reported a novel $Li_2S$/mesoporous carbon composite cathode and a silicon nanowire anode for lithium metal-free battery (Fig. 1.7b) [54]. The nanostructured design of both electrodes assists in overcoming the issues associated with using sulfur compounds and silicon in LIBs, and experimentally realized an initial discharge-specific energy of 630 Wh $kg^{-1}$ based on the mass of the active electrode materials.

The above researches adopt small-sized $Li_2S$ as active materials; however, bulk $Li_2S$ particles still suffer from low electrochemical activity and a large initial activation energy barrier (huge over-potential) [51, 52, 56, 57]. Many strategies have been proposed to circumvent the above issues, such as employing high energy ball-milled or pulsed laser deposition techniques to fabricate $Li_2S$–metal composites ($Li_2S$–Fe [58], $Li_2S$–Cu [59] and $Li_2S$–Co [60] composites) in order to improve the electrical conductivity of $Li_2S$. $Li_2S$–carbon composites are another widely adopted strategy utilized to overcome the current challenges with employing $Li_2S$ as a cathode. For example, carbon-coated $Li_2S$ core–shell spheres of varying sizes have

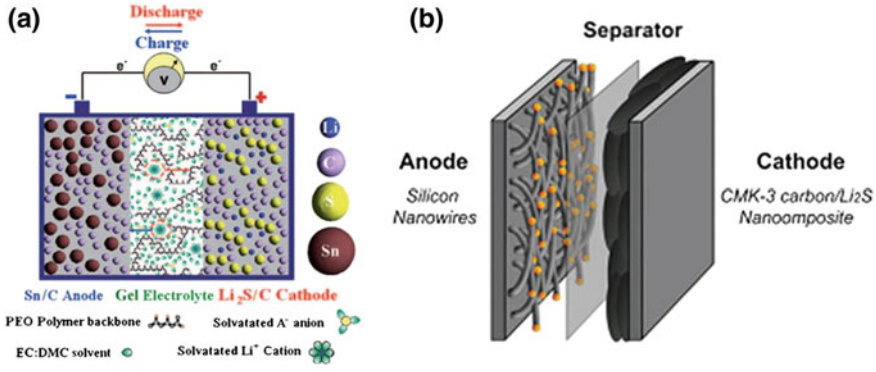


**Fig. 1.7** **a** Sketch of a Sn/C/CGPE/$Li_2S$/C polymer battery by a Sn/C composite anode, a PEO-based gel polymer electrolyte, and a $Li_2S$/C cathode. Reprinted from Ref. [55] by permission of John Wiley & Sons Ltd. **b** Schematic of a CMK-3 mesoporous carbon-embedded $Li_2S$/silicon nanowire battery. Reprinted with permission from Ref. [54]. Copyright 2010, American Chemical Society

**Table 1.1** The advantages and challenges of various sulfur cathode materials

| Cathodes | Advantages | Challenges |
|---|---|---|
| Sulfur–carbon composites | Carbon materials have large specific surface area, rich pore structure, excellent electrical conductivity, and abundant functional groups, which help improve the electrical conductivity and trap polysulfides | Optimize pore size and volume of carbon materials, improve the sulfur loading |
| Sulfur-conducting polymer composites | Low-temperature synthesis, surface functional groups restrict and trap polysulfides | Improve electrical conductivity and the sulfur loading |
| Sulfur/metal oxide composite | Large surface area helps adsorb polysulfides and limits the shuttle effect, catalyze the sulfur reduction and $Li_2S$ oxidation | Poor electrical conductivity of metal oxides, heavy mass of oxides reducing the energy density of Li–S batteries |
| Lithium sulfide-based cathodes | Avoid lithium dendrite issues and large amount of electrolyte consumption | $Li_2S$ easily reacts with $H_2O$ releasing hazardous $H_2S$ |

been synthesized via a two-step CVD method [61] and were able to demonstrate a high initial discharge capacity and stable cycling performance over 400 cycles at 0.5 C rate without additional carbon additives. $Li_2S$–C composite with lithium–nitrile interaction has been proposed by uniformly mixing lithium sulfide with PAN to form a lithium sulfide-PAN cross-linked matrix [62], enabling good cycling stability and high Coulombic efficiency. Aside from carbon coating, the encapsulation of $Li_2S$ particles using two-dimensional layered materials with high conductivity and strong binding affinity to $Li_2S/Li_2S_x$ species has recently been realized and well-explained by theoretical calculations [63]. All of these techniques demonstrated the feasibility of employing $Li_2S$ cathodes. However, the easy reaction of $Li_2S$ with $H_2O$ releasing hazardous $H_2S$ still limits the operation of $Li_2S$ in the dry environment or glovebox.

Based on the aforementioned discussion, the advantages and challenges of various sulfur cathode materials are summarized in Table 1.1.

### *1.1.2 Anode Materials*

As for the lithium anode side, the challenges mainly come from the reaction of metallic lithium with the electrolyte and polysulfides, causing corrosion of lithium metal, consumption of electrolyte, and low Coulombic efficiency. Nanostructured designs of lithium anodes and surface coating have been demonstrated as effective ways to protect metallic lithium, such as construction of a layer of interconnected hollow carbon nanospheres [64] or ultrathin BN/graphene [65] to form a stable solid electrolyte interphase (SEI) film; or employing 3D conducting scaffold as

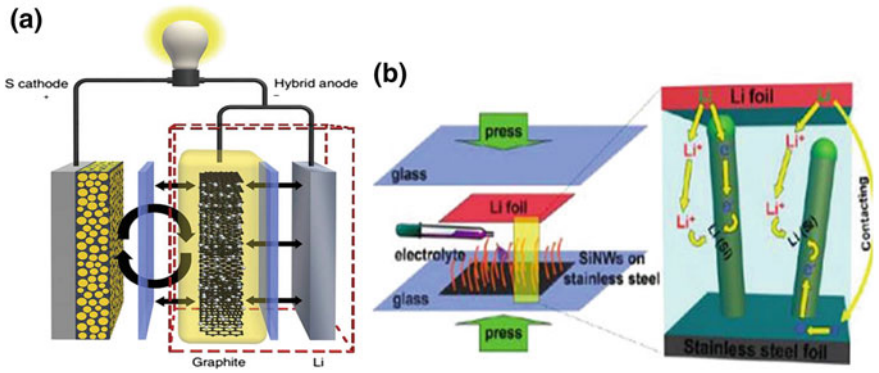


**Fig. 1.8** **a** Schematic of a hybrid anode design to manipulate the surface reactions on Li–S batteries. Reprinted with permission from Macmillan Publishers Ltd.: Ref. [68]. Copyright 2014. **b** Schematics showing the prelithiation of Si NWs on stainless steel foil, and the internal electron and $Li^+$ pathways during the prelithiation. Reprinted with permission from Ref. [69]. Copyright 2011, American Chemical Society

stable lithium hosts for Li stripping and plating [66, 67]. Another strategy reported by Liu's group is that they designed a Li–S battery using electrically connected graphite and lithium metal as a hybrid anode to control undesirable surface reactions on lithium side [68]. Lithiated graphite placed in front of the lithium metal functions as an artificial, self-regulated SEI layer to actively control the electrochemical reactions and minimize the deleterious side reactions, leading to significant performance improvement (Fig. 1.8a). Lithium–sulfur cells incorporating this hybrid anodes deliver capacities higher than 800 mAh $g^{-1}$ for 400 cycles at a high rate of 1737 mA $g^{-1}$, with only 11% capacity fade and a Coulombic efficiency larger than 99% [68]. Substituting the metallic Li anode by pairing the prelithiated Si or Sn anode with the sulfur cathode is another approach to address the lithium dendrite problems [69, 70]. For example, Cui group demonstrated a facile prelithiation method for silicon nanowires (Si NWs) [69]. Pressure was applied to induce electrical shorting between the Si NWs and the Li foil. As soon as the Si NWs and Li foil are shorted, the Si NWs begin to be electrochemically lithiated (Fig. 1.8b). With a 20 min prelithiation, the amount of lithium preloaded into the Si NWs is measured to be $\sim$2000 mAh $g^{-1}$ of Si. By directly pairing this prelithiated Si NW anode with an S/CMK-3 cathode, a proof-of-concept sulfur/Li–Si full battery demonstrates an initial discharge capacity of 1060 mAh $g^{-1}$ at 0.2 C and maintained 80% of the initial capacity after 10 cycles. Similarly, Kaskel's group sputtered 4 μm of amorphous silicon on a flexible carbon fiber material, and the Si–C anode was lithiated by short-circuiting versus metallic lithium. Then the prelithiated anode was paired with the carbon–sulfur cathode to assemble Li–S full cells [70]. The full cell showed a good stability with discharge capacity of 765 mAh $g^{-1}$ in the 5th cycle at 836 mA $g^{-1}$, and faded extremely slowly ($\sim$0.08%) over the following cycles. After 1400 reversible cycles, the capacity can

be maintained at 400 mAh $g^{-1}$ with Coulombic efficiency higher than 99%. The improved performance can be attributed to the stabled SEI and the electrolyte is not consumed upon cycling, confirming the feasibility of the prelithiation approach in the future applications.

### *1.1.3 Separators and Interlayers*

Great efforts have been devoted to alleviate the shuttle effect by designing nanostructured cathodes or anodes. The separator, however, has received less attention in Li–S batteries. Separator is an important part in Li–S batteries with the function to separate cathode and anode, and prevent internal short-circuit while maintaining the diffusion pathway of ions. It requires the separator to have good wetting ability and thermal stability. Modification of separators or the introduction of an interlayer between the sulfur cathode and separator is another promising route to trap polysulfides and reduce parasitic reaction [71]. Zhang and Huang et al. reported an efficient polysulfide ion shield by the incorporation of thin Nafion layer onto conventional polypropylene (PP) separator (Fig. 1.9a) [72]. With a simple coating-drying process, a thin Nafion layer with an areal loading amount of 0.7 mg $cm^{-2}$ was attached onto the PP membrane. The $-SO_3^-$-groups coated channels allow the hopping of lithium ions but reject the hopping of $S_n^{2-}$. In this case, lithium ions transfer freely and there is no significant increase in polarization, while the shuttle of lithium polysulfides was significantly suppressed. A high capacity of 781 mAh $g^{-1}$ at 1 C rate with Coulombic efficiency of over 95% and high cyclic stability of 0.08% per cycle decay rate were achieved within a long cycle test of 500 electrochemical cycles.

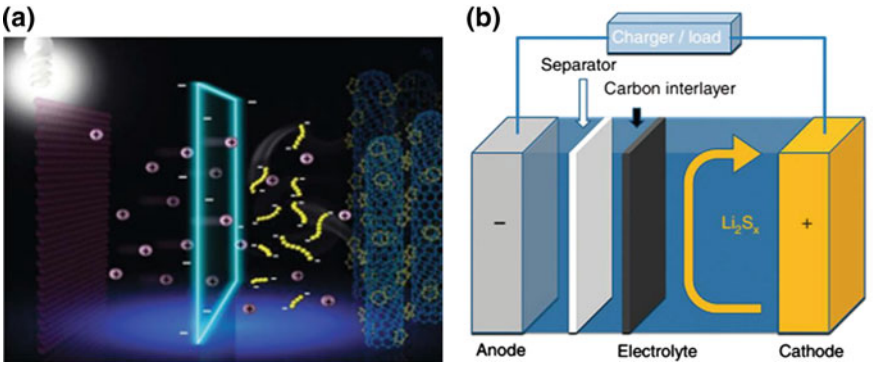


**Fig. 1.9** **a** Schematic of a Li–S battery configuration with ion selective transport membranes. Reprinted with permission from Ref. [72]. Copyright 2014, Royal Society of Chemistry. **b** Schematic configuration of a Li–S cell with a microporous carbon interlayer inserted between the sulfur cathode and the separator. Reprinted with permission from Macmillan Publishers Ltd.: Ref. [73]. Copyright 2012

Different from the modification of the commercial separators, Manthiram's group proposed to insert an interlayer between cathode and separator in a Li–S cell to serve as an upper current collector, which was effective in lowering the charge transfer resistance of the sulfur cathode and trapping of polysulfides in the cathode (Fig. 1.9b) [73]. These features afford an improved electrochemical performance of the batteries in both high specific capacity and excellent stability. A high initial discharge capacity of 1367 mAh $g^{-1}$ was delivered, and a high-rate capacity of 846 mAh $g^{-1}$ after 150 cycles at 2 C was achieved. Similarly, multi-walled CNTs (MWCNT) interlayer [74], activated carbon paper interlayer [75], and reduced GO barrier layer [76] also significantly improve the cell performance and this approach opens up a new research field for Li–S batteries. However, the introduction of interlayer itself will increase the weight of the battery, and inevitably decrease the energy density of the whole battery system. Therefore, optimization with controllable thickness and mass of the interlayer is critical toward building high-performance Li–S batteries.

### *1.1.4 Electrolyte*

Electrolyte is the medium for the transfer of $Li^+$ between cathode and anode, and the electrochemical behaviors can be dramatically different in various electrolytes for Li–S batteries, due to the different solubility and chemical interactions of polysulfides with various electrolyte solvents. Therefore, selection of suitable electrolytes is critically important for Li–S battery systems. Currently, liquid organic electrolytes are the main electrolytes applied in Li–S batteries. $LiClO_4$, $LiPF_6$, $Li(CF_3SO_2)_2N$, and LiTFSI are commonly used Li salts in Li–S systems. Compared with the commonly used $LiPF_6$ salt in LIBs, LiTFSI shows higher thermal and hydrolytic stability in Li–S batteries [36]. The main solvents utilized in Li–S batteries include ether and carbonate. Ether solvent shows good affinity with carbon and sulfur. For example, 1,3-dioxolane (DOL), 1,2-dimethoxyethane (DME), and tetra(ethylene glycol) dimethyl ether (TEGDME) are good in solubility of Li salts, with low viscosity and good Li ion conductivity [77, 78]. The widely used carbonate solvents in commercial LIBs, such as ethylene carbonate (EC), propylene carbonate (PC), and diethyl carbonate (DEC), are not suitable for Li–S batteries because carbonate-based solvents can react with polysulfide during the cycling process to generate possible thioether and sulfonium functionalities [79]. Therefore, only microporous carbon-based materials that confine sulfur molecules in the micropores can demonstrate impressive electrochemical properties with a carbonate-based electrolyte [14, 15]. These results suggest the importance in choosing electrolyte solvent, designing porous structure of carbon materials and investigating the existence states of sulfur molecules during cycling.

Generally, lithium salts are dissolved in the solvents forming the electrolytes. Recently, Hu group proposed the "solvent-in-salt" electrolyte (SIS electrolyte) with ultrahigh salt concentration (7 M LiTFSI per solvent) in DOL/DME with the aim of

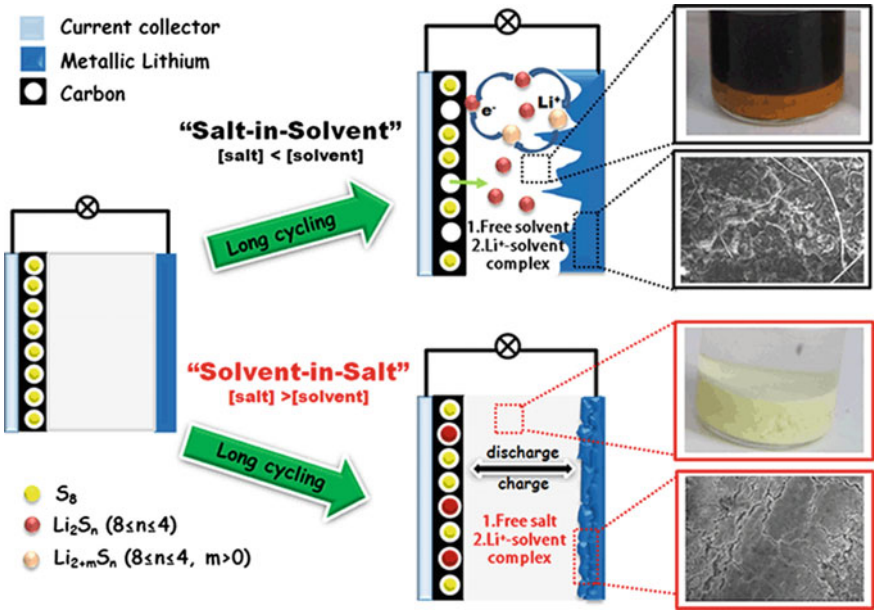


**Fig. 1.10** Schematic of the common "Salt-in-Solvent" and novel "Solvent-in-Salt" electrolytes in Li–S batteries, and the corresponding lithium polysulfide dissolution and surface morphology of lithium in different electrolyte systems. Reprinted with permission from Macmillan Publishers Ltd.: Ref. [80]. Copyright 2013

inhibiting the Li polysulfide dissolution and stabilizing the Li anode (Fig. 1.10) [80]. The ultrahigh concentration of LiTFSI in electrolyte is hard to dissolve the soluble polysulfide intermediate and thus avoids Li polysulfides shuttle. In addition, SIS electrolytes effectively protect metallic lithium anode against the formation of lithium dendrites, which makes the cell exhibit both excellent electrochemical performance and high safety. As a result, the CMK-3/S cathode with the SIS electrolyte delivers an initial specific discharge capacity of 1041 mAh $g^{-1}$ at 0.2 C with a high Coulombic efficiency during the cycling process, and the capacity maintained at 770 mAh $g^{-1}$ after 100 cycles. However, the high salt concentration increases the viscosity of the electrolytes which inevitably impedes the rapid transport of Li ion, leading to a lower rate performance with high polarization. Besides organic liquid electrolytes, room-temperature ionic liquid (RTIL) owns the advantages of high working voltage range (4–6 V), low-vapor-pressure, good thermal stability, and non-flammable properties, which can improve the safety of Li–S batteries. Moreover, the high-viscosity characteristics of RTIL could suppress the dissolution and shuttle of polysulfides, enhancing the cyclic stability of Li–S batteries at the expense of poor rate capability [36, 81, 82]. However, the high cost and difficult in fabricating ionic liquid still impede their large-scale application in Li–S batteries.

The electrolyte plays a key role in securing high battery safety. All solid-state Li–S batteries are thus promising because of their wide voltage range, high temperature tolerance, and mechanical robustness, and are regarded as the final target for building high-performance Li–S batteries [83]. Solid-state electrolytes have the solvent-free characteristics, which act as both the separators and electrolytes, and restrict the polysulfides in the cathode side. Additionally, they have the advantages of high safety with non-leakage and non-flammability properties, and also suppress the growth of Li dendrites [55, 84–86]. For instance, Scrosati et al. developed a solid-state Li–S battery employing a poly(ethylene oxide)-based (PEO-based) gel-type polymer membrane containing a PEO-$LiCF_3SO_3$ polymer matrix with finely dispersed nanosized zirconia and a $Li_2S$–C composite cathode [84]. The addition of zirconia increased the ionic conductivity of the composite electrolyte and improved the interfacial stability, thereby improving the electrochemical performance. A high specific capacity of about 900 mAh $g^{-1}$, referred to the sulfur mass, can be obtained by the all solid-state Li–S battery at 90 °C. Assuming an average voltage of 2.25 V, energy density value of 2025 Wh $kg^{-1}$ is obtained. Even considering a three times drop due to the weight of the electrolyte and of the case, the energy density (600 Wh $kg^{-1}$) remains considerably higher than that provided by conventional LIBs. However, they have a fast capacity fade and poor rate capability caused by low ionic conductivity of the solid-state electrolytes, especially at low temperatures, which needs to be further resolved through exploiting new solid-state electrolyte materials with higher ionic conductivity at room/low temperature. For the use of solid-state electrolytes, attention should also be paid to the optimization of the electrode/electrolyte interface to improve the battery safety and interfacial contact with a high utilization of the active surface of electrode materials.

## 1.2 Motivations of the Thesis

Based on the above investigation, there is an urgency to develop high-capacity electrode materials and explore new battery systems with multi-electrons reaction. Sulfur cathode materials are potential high energy electrode materials, but the low electrical conductivity, low material utilization, poor structural stability, and low cycle life during discharge/charge impede their application. Carbon materials have large surface area, high electrical conductivity, rich porosity, and various surface functional groups, so they can be used to construct electrically conductive network, anchor/disperse sulfur, buffer the volume change of sulfur during cycling, and consequently obtain high performance. In this dissertation, we designed and developed high-performance sulfur/carbon composite cathode materials by confining sulfur in micropores, surface active sites, two graphene membranes, and 3D graphene framework toward building high-capacity, high-power and long-life Li–S batteries.

# References


1. Tarascon JM, Armand M (2001) Issues and challenges facing rechargeable lithium batteries. Nature 414(6861):359–367
2. Dunn B, Kamath H, Tarascon J-M (2011) Electrical energy storage for the grid: a battery of choices. Science 334(6058):928–935
3. Bruce PG, Freunberger SA, Hardwick LJ, Tarascon J-M (2012) Li–$O_2$ and Li–S batteries with high energy storage. Nat Mater 11(1):19–29
4. Yang Y, Zheng G, Cui Y (2013) Nanostructured sulfur cathodes. Chem Soc Rev 42(7):3018–3032
5. Manthiram A, Fu Y, Chung S-H, Zu C, Su Y-S (2014) Rechargeable lithium-sulfur batteries. Chem Rev 114(23):11751–11787
6. Liang Z et al (2014) Sulfur cathodes with hydrogen reduced titanium dioxide inverse opal structure. ACS Nano 8(5):5249–5256
7. Manthiram A, Fu Y, Su Y-S (2012) Challenges and prospects of lithium-sulfur batteries. Acc Chem Res 46(5):1125–1134
8. Kolosnitsyn VS, Karaseva EV (2008) Lithium-sulfur batteries: Problems and solutions. Russ J Electrochem 44(5):506–509
9. Wang D-W et al (2012) A microporous-mesoporous carbon with graphitic structure for a high-rate stable sulfur cathode in carbonate solvent-based Li–S batteries. Phys Chem Chem Phys 14(24):8703–8710
10. Wang D-W et al (2013) Carbon-sulfur composites for Li–S batteries: status and prospects. J Mater Chem A 1(33):9382–9394
11. Zhang Q, Cheng XB, Huang JQ, Peng HJ, Wei F (2014) Review of carbon materials for advanced lithium-sulfur batteries. New Carbon Mater 29(4):241–264
12. Ji XL, Lee KT, Nazar LF (2009) A highly ordered nanostructured carbon-sulphur cathode for lithium-sulphur batteries. Nat Mater 8(6):500–506
13. Liang CD, Dudney NJ, Howe JY (2009) Hierarchically structured sulfur/carbon nanocomposite material for high-energy lithium battery. Chem Mater 21(19):4724–4730
14. Xin S et al (2012) Smaller sulfur molecules promise better lithium-sulfur batteries. J Am Chem Soc 134(45):18510–18513
15. Zhang B, Qin X, Li GR, Gao XP (2010) Enhancement of long stability of sulfur cathode by encapsulating sulfur into micropores of carbon spheres. Energy Environ Sci 3(10):1531–1537
16. Li Z et al (2014) Insight into the electrode mechanism in lithium-sulfur batteries with ordered microporous carbon confined sulfur as the cathode. Adv Energy Mater 4(7):1301473
17. Wang HL et al (2011) Graphene-Wrapped sulfur particles as a rechargeable lithium-sulfur battery cathode material with high capacity and cycling stability. Nano Lett 11(7):2644–2647
18. Cao YL et al (2011) Sandwich-type functionalized graphene sheet-sulfur nanocomposite for rechargeable lithium batteries. Phys Chem Chem Phys 13(17):7660–7665
19. Zhang FF, Zhang XB, Dong YH, Wang LM (2012) Facile and effective synthesis of reduced graphene oxide encapsulated sulfur via oil/water system for high performance lithium sulfur cells. J Mater Chem 22(23):11452–11454
20. Huang J-Q et al (2013) Entrapment of sulfur in hierarchical porous graphene for lithium–sulfur batteries with high rate performance from −40 to 60 °C. Nano Energy 2(2):314–321
21. Lv W et al (2014) Tailoring microstructure of graphene-based membrane by controlled removal of trapped water inspired by the phase diagram. Adv Funct Mater 24(22):3456–3463
22. Zhao M-Q et al (2012) Graphene/single-walled carbon nanotube hybrids: one-step catalytic growth and applications for high-rate Li–S batteries. ACS Nano 6(12):10759–10769
23. Peng H-J et al (2014) Nanoarchitectured Graphene/CNT@Porous carbon with extraordinary electrical conductivity and interconnected micro/mesopores for lithium-sulfur batteries. Adv Funct Mater 24(19):2772–2781
24. Zhao M-Q et al (2014) Unstacked double-layer templated graphene for high-rate lithium–sulphur batteries. Nat Commun 5:3410

25. Ji LW et al (2011) Graphene oxide as a sulfur immobilizer in high performance lithium/sulfur cells. J Am Chem Soc 133(46):18522–18525
26. Zu CX, Manthiram A (2013) Hydroxylated graphene–sulfur nanocomposites for high-rate lithium–sulfur batteries. Adv Energy Mater 3(8):1008–1012
27. Zhang C et al (2014) Reduction of graphene oxide by hydrogen sulfide: a promising strategy for pollutant control and as an electrode for Li–S batteries. Adv Energy Mater 4(7):1301565
28. Yuan LX, Yuan HP, Qiu XP, Chen LQ, Zhu WT (2009) Improvement of cycle property of sulfur-coated multi-walled carbon nanotubes composite cathode for lithium/sulfur batteries. J Power Sources 189(2):1141–1146
29. Zhang S-M et al (2013) Composite cathodes containing SWCNT@S coaxial nanocables: facile synthesis, surface modification, and enhanced performance for Li-Ion storage. Part Part Syst Charact 30(2):158–165
30. Su YS, Fu YZ, Manthiram A (2012) Self-weaving sulfur-carbon composite cathodes for high rate lithium-sulfur batteries. Phys Chem Chem Phys 14(42):14495–14499
31. Dorfler S et al (2012) High capacity vertical aligned carbon nanotube/sulfur composite cathodes for lithium–sulfur batteries. Chem Commun 48(34):4097–4099
32. Huang JQ et al (2013) Aligned sulfur-coated carbon nanotubes with a polyethylene glycol barrier at one end for use as a high efficiency sulfur cathode. Carbon 58:99–106
33. Cheng X-B et al (2014) Aligned carbon nanotube/sulfur composite cathodes with high sulfur content for lithium–sulfur batteries. Nano Energy 4:65–72
34. Zheng GY, Yang Y, Cha JJ, Hong SS, Cui Y (2011) Hollow carbon nanofiber-encapsulated sulfur cathodes for high specific capacity rechargeable lithium batteries. Nano Lett 11 (10):4462–4467
35. Guo JC, Xu YH, Wang CS (2011) Sulfur-impregnated disordered carbon nanotubes cathode for lithium–sulfur batteries. Nano Lett 11(10):4288–4294
36. Yin YX, Xin S, Guo YG, Wan LJ (2013) Lithium–sulfur batteries: electrochemistry, materials, and prospects. Angew Chem Int Ed 52(50):13186–13200
37. Wu F, Lee JT, Zhao E, Zhang B, Yushin G (2016) Graphene–$Li_2S$–Carbon nanocomposite for lithium-sulfur batteries. ACS Nano 10(1):1333–1340
38. Wang JL, Yang J, Xie JY, Xu NX (2002) A novel conductive polymer–sulfur composite cathode material for rechargeable lithium batteries. Adv Mater 14(13–14):963–965
39. Fu Y, Manthiram A (2012) Orthorhombic bipyramidal sulfur coated with polypyrrole nanolayers as a cathode material for lithium–sulfur batteries. J Phys Chem C 116(16):8910–8915
40. Xiao LF et al (2012) A soft approach to encapsulate sulfur: polyaniline nanotubes for lithium–sulfur batteries with long cycle life. Adv Mater 24(9):1176–1181
41. Wu F et al (2011) Sulfur/polythiophene with a core/shell structure: synthesis and electrochemical properties of the cathode for rechargeable lithium batteries. J Phys Chem C 115(13):6057–6063
42. Chen HW et al (2013) Ultrafine sulfur nanoparticles in conducting polymer shell as cathode materials for high performance lithium/sulfur batteries. Sci Rep 3:1910
43. Choi YJ et al (2007) Electrochemical properties of sulfur electrode containing nano $Al_2O_3$ for lithium/sulfur cell. Phys Scripta T129:62–65
44. Evers S, Yim T, Nazar LF (2012) Understanding the nature of absorption/adsorption in nanoporous polysulfide sorbents for the Li–S battery. J Phys Chem C 116(37):19653–19658
45. Ji X, Evers S, Black R, Nazar LF (2011) Stabilizing lithium–sulphur cathodes using polysulphide reservoirs. Nat. Commun. 2:325–331
46. Zheng W, Hu XG, Zhang CF (2006) Electrochemical properties of rechargeable lithium batteries with sulfur-containing composite cathode materials. Electrochem Solid State Lett 9 (7):A364–A367
47. Sun F et al (2013) A high-rate lithium-sulfur battery assisted by nitrogen-enriched mesoporous carbons decorated with ultrafine $La_2O_3$ nanoparticles. J Mater Chem A 1 (42):13283–13289

48. Song MS et al (2004) Effects of nanosized adsorbing material on electrochemical properties of sulfur cathodes for Li/S secondary batteries. J Electrochem Soc 151(6):A791–A795
49. Seh Z et al (2013) Sulphur–$TiO_2$ yolk–shell nanoarchitecture with internal void space for long-cycle lithium–sulphur batteries. Nat. Commun. 4:1331
50. Tao X et al (2014) Strong sulfur binding with conducting Magnéli-Phase $Ti_nO_{2n-1}$ nanomaterials for improving lithium-sulfur batteries. Nano Lett 14(9):5288–5294
51. Yang Y et al (2012) High-Capacity micrometer-Sized $Li_2S$ particles as cathode materials for advanced rechargeable lithium-ion batteries. J Am Chem Soc 134(37):15387–15394
52. Zu C, Klein M, Manthiram A (2014) Activated $Li_2S$ as a high-performance cathode for rechargeable lithium-sulfur batteries. J Phys Chem Lett 5(22):3986–3991
53. Son Y, Lee J-S, Son Y, Jang J-H, Cho J (2015) Recent advances in lithium sulfide cathode materials and their use in lithium sulfur batteries. Adv Energy Mater 5(16):1500110
54. Yang Y et al (2010) New nanostructured $Li_2S$/Silicon rechargeable battery with high specific energy. Nano Lett 10(4):1486–1491
55. Hassoun J, Scrosati B (2010) A high-performance polymer tin sulfur lithium ion battery. Angew Chem Int Ed 49(13):2371–2374
56. Meini S, Elazari R, Rosenman A, Garsuch A, Aurbach D (2014) The Use of redox mediators for enhancing utilization of $Li_2S$ cathodes for advanced Li–S battery systems. J Phys Chem Lett 5(5):915–918
57. Wang C et al (2015) Slurryless $Li_2S$/reduced graphene oxide cathode paper for high-performance lithium sulfur battery. Nano Lett 15(3):1796–1802
58. Obrovac MN, Dahn JR (2002) Electrochemically active lithia/metal and lithium sulfide/metal composites. Electrochem Solid State Lett 5(4):A70–A73
59. Hayashi A, Ohtsubo R, Ohtomo T, Mizuno F, Tatsumisago M (2008) All-solid-state rechargeable lithium batteries with $Li_2S$ as a positive electrode material. J Power Sources 183 (1):422–426
60. Zhou Y, Wu C, Zhang H, Wu X, Fu Z (2007) Electrochemical reactivity of Co–$Li_2S$ nanocomposite for lithium-ion batteries. Electrochim Acta 52(9):3130–3136
61. Nan C et al (2014) Durable carbon-coated $Li_2S$ core-shell spheres for high performance lithium/sulfur cells. J Am Chem Soc 136(12):4659–4663
62. Guo J, Yang Z, Yu Y, Abruña HD, Archer LA (2013) Lithium-Sulfur battery cathode enabled by lithium-nitrile interaction. J Am Chem Soc 135(2):763–767
63. Seh ZW et al (2014) Two-dimensional layered transition metal disulphides for effective encapsulation of high-capacity lithium sulphide cathodes. Nat Commun 5:5017
64. Zheng G et al (2014) Interconnected hollow carbon nanospheres for stable lithium metal anodes. Nat Nanotech 9(8):618–623
65. Yan K et al (2014) Ultrathin two-dimensional atomic crystals as stable interfacial layer for improvement of lithium metal anode. Nano Lett 14(10):6016–6022
66. Lin D et al (2016) Layered reduced graphene oxide with nanoscale interlayer gaps as a stable host for lithium metal anodes. Nat Nano 11(7):626–632
67. Liang Z et al (2016) Composite lithium metal anode by melt infusion of lithium into a 3D conducting scaffold with lithiophilic coating. Proc Natl Acad Sci USA 113(11):2862–2867
68. Huang C et al (2014) Manipulating surface reactions in lithium-sulphur batteries using hybrid anode structures. Nat Commun 5:3015
69. Liu NA, Hu LB, McDowell MT, Jackson A, Cui Y (2011) Prelithiated silicon nanowires as an anode for lithium ion batteries. ACS Nano 5(8):6487–6493
70. Brückner J et al (2014) Carbon-Based Anodes For Lithium Sulfur Full Cells With High Cycle Stability. Adv Funct Mater 24(9):1284–1289
71. Huang J-Q, Zhang Q, Wei F (2015) Multi-functional separator/interlayer system for high-stable lithium-sulfur batteries: progress and prospects. Energy Storage Mater 1:127–145
72. Huang JQ et al (2014) Ionic shield for polysulfides towards highly-stable lithium-sulfur batteries. Energy Environ Sci 7(1):347–353
73. Su Y-S, Manthiram A (2012) Lithium–sulphur batteries with a microporous carbon paper as a bifunctional interlayer. Nat Commun 3:1166

74. Su YS, Manthiram A (2012) A new approach to improve cycle performance of rechargeable lithium–sulfur batteries by inserting a free-standing MWCNT interlayer. Chem Commun 48 (70):8817–8819
75. Zu CX, Su YS, Fu YZ, Manthiram A (2013) Improved lithium-sulfur cells with a treated carbon paper interlayer. Phys Chem Chem Phys 15(7):2291–2297
76. Wang X, Wang Z, Chen L (2013) Reduced graphene oxide film as a shuttle-inhibiting interlayer in a lithium–sulfur battery. J Power Sources 242:65–69
77. Chang DR, Lee SH, Kim SW, Kim HT (2002) Binary electrolyte based on tetra(ethylene glycol) dimethyl ether and 1,3-dioxolane for lithium-sulfur battery. J Power Sources 112 (2):452–460
78. Shim J, Striebel KA, Cairns EJ (2002) The lithium/sulfur rechargeable cell—effects of electrode composition and solvent on cell performance. J Electrochem Soc 149(10):A1321–A1325
79. Gao J, Lowe MA, Kiya Y, Abruna HD (2011) Effects of Liquid electrolytes on the charge-discharge performance of rechargeable lithium/sulfur batteries: electrochemical and in-situ X-ray absorption spectroscopic studies. J Phys Chem C 115(50):25132–25137
80. Suo L, Hu Y-S, Li H, Armand M, Chen L (2013) A new class of solvent-in-salt electrolyte for high-energy rechargeable metallic lithium batteries. Nat Commun 4:1481
81. Yuan LX et al (2006) Improved dischargeability and reversibility of sulfur cathode in a novel ionic liquid electrolyte. Electrochem Commun 8(4):610–614
82. Park JW, Ueno K, Tachikawa N, Dokko K, Watanabe M (2013) Ionic Liquid Electrolytes for Lithium–Sulfur Batteries. J Phys Chem C 117(40):20531–20541
83. Zhou G, Li F, Cheng H-M (2014) Progress in flexible lithium batteries and future prospects. Energy Environ Sci 7:1307–1338
84. Hassoun J, Scrosati B (2010) Moving to a solid-state configuration: a valid approach to making lithium-sulfur batteries viable for practical applications. Adv Mater 22(45):5198–5201
85. Hayashi A, Ohtomo T, Mizuno F, Tadanaga K, Tatsumisago M (2003) All-solid-state Li/S batteries with highly conductive glass-ceramic electrolytes. Electrochem Commun 5(8):701–705
86. Nagao M, Hayashi A, Tatsumisago M (2011) Sulfur–carbon composite electrode for all-solid-state Li/S battery with Li2S–P2S5 solid electrolyte. Electrochim Acta 56(17):6055–6059

# Chapter 2
# Revealing Localized Electrochemical Transition of Sulfur in Sub-nanometer Confinement

## 2.1 Research Background

Current concerns of the pressing environmental pollution issues and limited fossil energy resources have increased the R&D interest and investment in clean energy technologies. LIBs, as commonly used clean energy storage devices, have transformed portable electronic devices and electric transportation greatly, but have limitations of high cost and relatively low specific energy [1]. Due to advantages such as high capacity, extremely low cost, and nontoxicity, sulfur has received considerable attention as a positive electrode material in Li–S batteries. Li–S batteries can deliver a very high theoretical specific energy of 2567 Wh $kg^{-1}$ or 2199 Wh $L^{-1}$ and dramatically outperform current LIBs [1, 2]. However, the low electronic/ionic conductivity of sulfur and the discharge products, large volume change ($\sim$80%) of sulfur during the lithiation/delithiation processes, and the shuttling of dissolved lithium polysulfides ($Li_2S_x$, $3 \leq x \leq 8$) between the sulfur cathode and the lithium–metal anode during cycling severely impede the practical applications of Li–S batteries [3, 4]. These problems not only lead to poor cycling stability, inferior rate capability, and low Coulombic efficiency, but also cause the deposition of insulating $Li_2S/Li_2S_2$ on both electrodes, resulting in low sulfur utilization and even triggering a series of safety problems [5–7].

Most current research has focused on solving the problems of polysulfide dissolution by reducing polysulfide solubility and/or adsorbing dissolved polysulfides in the cathode. The use of polymer-based or ionic liquid-based electrolytes eliminates the need for organic solvents in which polysulfides have high solubility [8–11], however the increased electrolyte viscosity and resistivity are detrimental to rate performance. Metal oxides, polymers, and silica can chemically or physically



G. Zhou, *Design, Fabrication and Electrochemical Performance of Nanostructured Carbon Based Materials for High-Energy Lithium–Sulfur Batteries*, Springer Theses,
DOI 10.1007/978-981-10-3406-0_2

adsorb polysulfide anions [12–15], but their semiconducting or insulating nature unavoidably slows down cathode reaction kinetics.

Porous carbon combines high adsorption capacity with good conductivity and is regarded as the best cathode sorbent. Various carbon–sulfur composite electrodes, such as carbon nanotubes/nanofibers [16–19], graphene [20, 21], mesoporous carbon [2, 22, 23], microporous carbon, and hierarchical porous carbon [24, 25] have been used in Li–S batteries. It is worth stressing, however, that these advances are partially due to the use of a non-carbonate solvent-based electrolyte and the additive $LiNO_3$ salt, in which the solubility of polysulfides is reduced or the polysulfide shuttle is passivated [26, 27]. Although the development of Li–S batteries requires advances in both the cathode and the electrolyte, the advantage of carbon materials that they can stabilize the sulfur cathode can be more clearly highlighted using the carbonate electrolyte that generates the most aggressive electrochemical environment attacking polysulfides. It has been found that the carbonate solvent trapped in a gel polymer electrolyte is less aggressive due to the physical shielding role of the polymer layer and allows the carbon–sulfur cathode to reversibly operate for 90 cycles [28]. Much longer cycling life of sulfur in a mixed carbonate electrolyte can be achieved by a micropore-confined cathode, which can operate stably over 500 cycles [24]. Therefore it is suggested that microporous carbon is the best candidate for Li–S cathodes using any solvent regarding merely the stability. Nonetheless the final lithium sulfide discharge product can only be formed at 1.0 V versus $Li^+/Li^0$ in this micropore-confined cathode [24]. The large lithiation overpotential represents the slow cathode reaction kinetics that possibly arises from retarded lithium ion migration in micropores. Unfortunately, little attention has been paid to develop a kinetically favorable micropore-confined sulfur cathode.

Based on the above analysis, it is not clear whether carbonate-based electrolyte can be used in Li–S batteries and immobilization of sulfur in pores has shown quite different cathode behavior depending on the pore size. The challenge of stable high-rate capacity remains unmet due to either the weak adsorption potential of mesopores or the blocking of porous networks after the sulfur filling. Understanding the confinement effect for different pore size and the suitable situation for employing carbonate-based electrolyte is a crucial step towards achieving high reversible capacity and long cycle life in Li–S batteries. In this work, we report the use of a microporous-mesoporous carbon with graphitic structure as the sulfur immobilizer for a high-rate stable Li–S cathode in a carbonate electrolyte. The sulfur was confined in micropores and its stability was tested over 800 cycles in an aggressive carbonate electrolyte. The high-rate capability of this cathode is excellent allowing a fast charge/discharge operation. This high-rate performance is due to the graphitic structure and mesoporous framework which facilitate the transport of both electrons and ions.

## 2.2 Design, Fabrication, and Characterization of Carbon–Sulfur Composite Cathode

### *2.2.1 Synthesis of Hierarchical Porous Carbon (HPC)*

The HPC carbon matrix with microporous-mesoporous texture and graphitic structure was synthesized by mixing phenolic resin solution (100 mL, 20 wt%) with nickel hydroxide suspension. The nickel hydroxide was prepared in advance by adding nickel nitrate (5 g) into sodium hydroxide (100 mL, 10 wt%) solution. Subsequently, 25 g of 20 wt% ethanol solution of phenolic resin was added under intense stirring. The hybrid system was evaporated for 24 h in a glass utensil at 90 °C under ambient pressure to obtain the composite of inorganics and resin. The composite was carbonized in a tubular furnace under argon atmosphere via heating ramps of 10 °C $min^{-1}$ from room temperature to 200 °C and keeping at 200 °C for 2 h, then heating to 600 °C and keeping at 600 °C for 4 h. After carbonization, the inorganic species were etched with 3 M HCl solution and filtrated to wash the samples. The final product was obtained by subsequent drying at 90 °C in a vacuum oven for 24 h. The transmission electron microscopy (TEM) image in Fig. 2.1a reveals the mesoporous texture of the carbon matrix. The graphitic nanoribbons in the carbon matrix can be seen from the high-resolution TEM image in Fig. 2.1b. Micropores are embedded in the amorphous area surrounding the graphitic regions but are hardly visible owing to the small dimensions. The mesoporous texture favors the fast migration of solvated lithium ions, and the graphitic nanoribbons facilitate electron conduction [29].

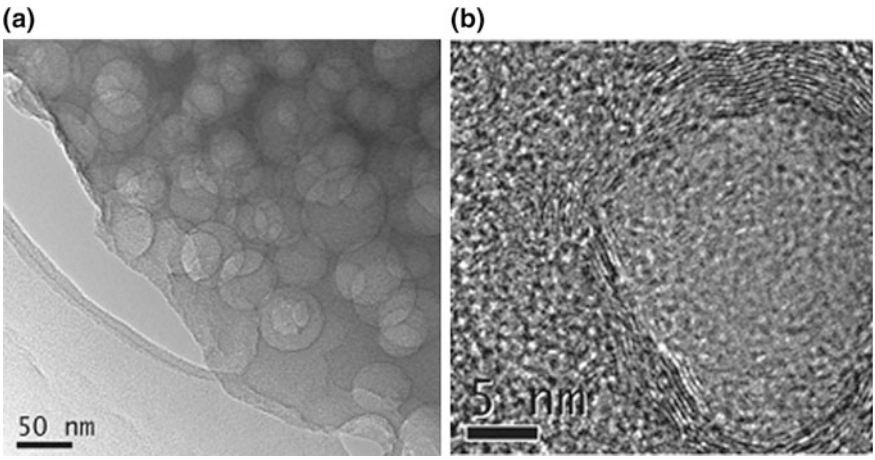


**Fig. 2.1** **a** Low-magnification and **b** high-resolution TEM images of the hierarchical porous carbon

### 2.2.2 Synthesis of Carbon–Sulfur Composite

In order to investigate the pore-dependent confinement mechanism, sulfur was infused into different pore sizes, the detailed synthesis process is as follows: HPC and sulfur powders at a mass ratio of 1:1 were ground together and heated at 155 °C for 12 h in argon gas. At this stage, the sulfur is stored in macro/meso/micropores of HPC and sample is labeled CS-Ad. The selective extraction of sulfur from CS-Ad was carried out using carbon disulfide washing. The as-obtained CS-Ad powder was immersed in 30 mL of carbon disulfide and stirred for 10 min at room temperature. The carbon disulfide containing dissolved sulfur was quickly filtered, and the sample was washed again with clean carbon disulfide. The remaining sample, labeled CS-Ex with sulfur mainly confined in the micropores, was dried in a vacuum oven at 50 °C for 8 h (Fig. 2.2).

### 2.2.3 Structure Characterization of the Carbon–Sulfur Composite

The existence of sulfur in both CS-Ad and CS-Ex was confirmed by X-ray photoelectron spectroscopy (XPS) (Fig. 2.3). The peaks located at 163.6 eV, 228.3 eV,

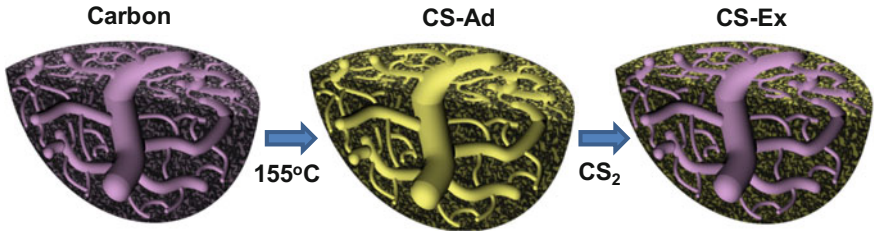


**Fig. 2.2** Schematic of the preparation of CS-Ad and CS-Ex through the adsorption and extraction strategy

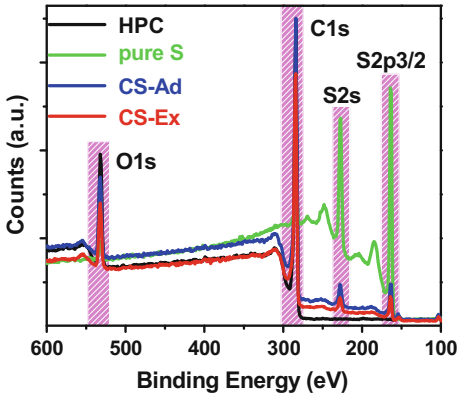


**Fig. 2.3** XPS spectra of the hierarchical porous carbon, sulfur, CS-Ad and CS-Ex

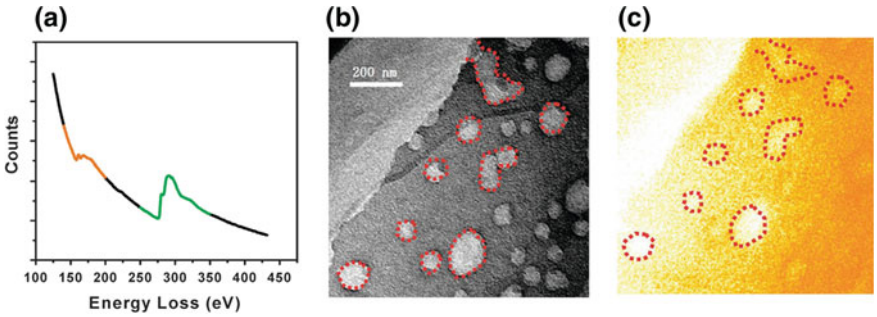


**Fig. 2.4** **a** EELS spectrum of sulfur (165 eV) and carbon (284 eV) edges with an energy window of 20 eV. **b** Zero-loss low-magnification image of the carbon of CS-Ex and **c** EELS elemental mapping image of sulfur in the porous texture of CS-Ex

284.6 eV, and 532.2 eV are attributed to the $S2p_{3/2}$, S2s, C1s, and O1s, which are in agreement with the $S2p_{3/2}$ and S2s peaks in pure sulfur and C1s/O1s peaks in the HPC, indicating the successful immobilization of sulfur in the pores of HPC. The distribution of sulfur was tracked using electron energy loss spectroscopy (EELS) and EELS mapping methods (Fig. 2.4). In CS-Ex, only carbon (284 eV) and sulfur (165 eV) signal peaks can be detected from the EELS, and sulfur is preferentially confined in micropores, which are located around the mesopores highlighted by dotted red lines (Fig. 2.4b and c). The contrasting difference between the micropores and some mesopores suggests significant molecular-level confinement of sulfur in micropores, with only a small amount retained in the mesopores.

The selective immobilization of sulfur in pores with different sizes is evident from the nitrogen adsorption isotherms in Fig. 2.5a and the pore size distributions are shown in Fig. 2.5b. The molten sulfur was embedded in the voids of the carbon matrix by capillary forces, where it solidified causing a significant loss of pore volume (Fig. 2.5a). The pore volume of the carbon matrix is 0.44 $cm^3\ g^{-1}$.

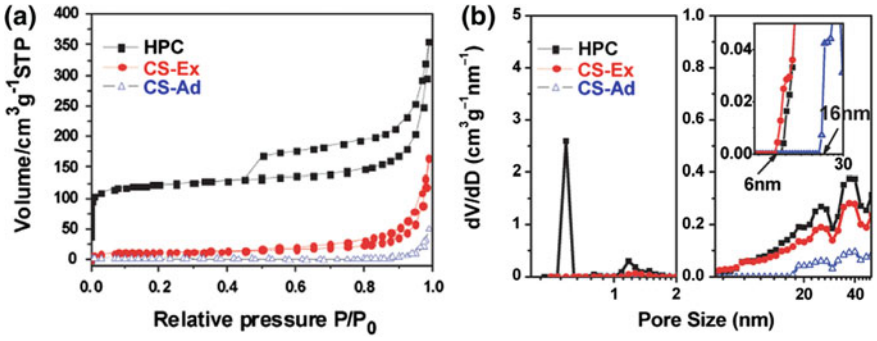


**Fig. 2.5** **a** Liquid nitrogen adsorption–desorption isotherms and **b** pore size distribution of HPC, CS-Ad and CS-Ex composites

The CS-Ad sample has a pore volume less than 0.1 $cm^3\ g^{-1}$ compared to the 0.24 $cm^3\ g^{-1}$ of the CS-Ex sample. Meanwhile, the specific surface area of the carbon matrix is 413 $m^2\ g^{-1}$, while that for CS-Ad and CS-Ex are 8 and 43 $m^2\ g^{-1}$, respectively. The infiltration resulted in the disappearance of 6–16 nm mesopores in the carbon matrix as shown in Fig. 2.5b. Additionally, the pore volume in the range above 16 nm also decreased sharply due to the presence of sulfur. After $CS_2$ extraction, sulfur was removed substantially from mesopores, as was clear from the fact that the pore volume distribution was similar to that of the original carbon matrix, but micropores were still occupied by sulfur in the extracted sample. It is noted that no mesopores in the range between 2 and 6 nm were measured for the carbon matrix based on liquid nitrogen cryosorption analysis. It is clear that $CS_2$ extraction cannot remove sulfur from micropores (0.6–0.7 nm, with a peak value of 0.65 nm), but can effectively extract sulfur from the mesopores with partial sulfur removal from 1 to 1.6 nm pores, named hereafter "super-micropores". Sulfur in super-micropores is in trace amounts. The sulfur residue after $CS_2$ extraction is likely to be surface adsorbed by the mesopores in the carbon scaffold. These results are consistent with the XPS analysis.

X-ray diffraction (XRD) peaks, shown in Fig. 2.6a, reveal the rhombic-monoclinic phase transition of sulfur solidified in CS-Ad from the melt, indicating the crystalline nature of sulfur in mesopores. The well-resolved peaks corresponding to monoclinic sulfur in CS-Ad disappeared completely after $CS_2$ extraction, indicating the amorphous nature of sulfur confined by micropores in CS-Ex [24, 30]. Raman spectroscopy confirms the crystalline nature of sulfur in mesopores and the amorphous nature of sulfur in micropores (Fig. 2.6b).

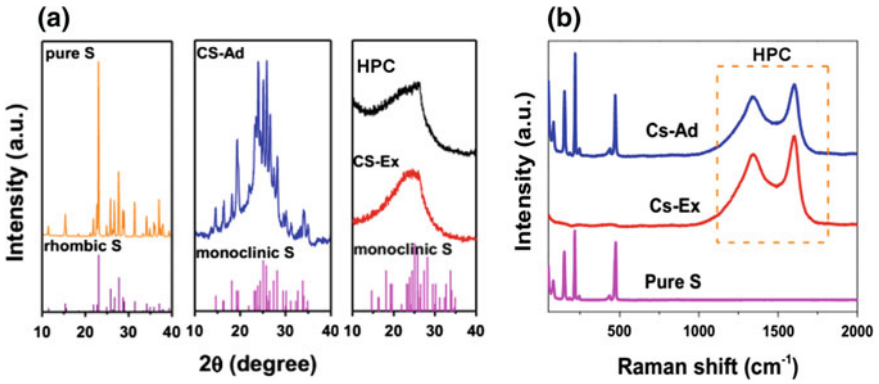


**Fig. 2.6** **a** XRD patterns of HPC, pure sulfur and sulfur confined in pores with different sizes, showing the phase evolution of sulfur (rhombic-monoclinic-amorphous) corresponding to the adsorption-extraction method, and **b** Raman spectra of pure sulfur, CS-Ad and CS-Ex

### 2.2.4 *Electrochemical Performance of the Carbon–Sulfur Composite Cathode*

To understand the effect of pore size in affecting the performance, Li–S cells were assembled with a metallic lithium foil anode and a CS-Ad or CS-Ex cathode. A commercial carbonate electrolyte ($LiPF_6$ in EC/DMC/EMC) was used directly without any modification. Cyclic voltammetry (CV) profiles were recorded to determine the lithiation potential of sulfur confined in pores with different sizes, as given in Fig. 2.7. As seen, there are two peaks in the first reduction process of CS-Ex (Fig. 2.7a). The small peak at 2.43 V (vs. $Li^+/Li^0$) corresponds to the conversion from elemental sulfur ($S_8$) to lithium polysulfide anions ($Li_2S_x$, $4 \leq x \leq 8$) [2, 24]. However, this peak is not observed in the second reduction cycle (Fig. 2.7b). The small peak is most likely caused by the reduction of a trace of sulfur in pores larger than 6 nm in CS-Ex, which is weakly adsorbed and easily dissolved into the electrolyte. The tiny magnitude of this reaction with respect to the strong reduction peak at 1.62 V (vs. $Li^+/Li^0$) suggests the considerable confinement of sulfur in micropores. The cathodic peak at 1.62 V is in accordance with the deep

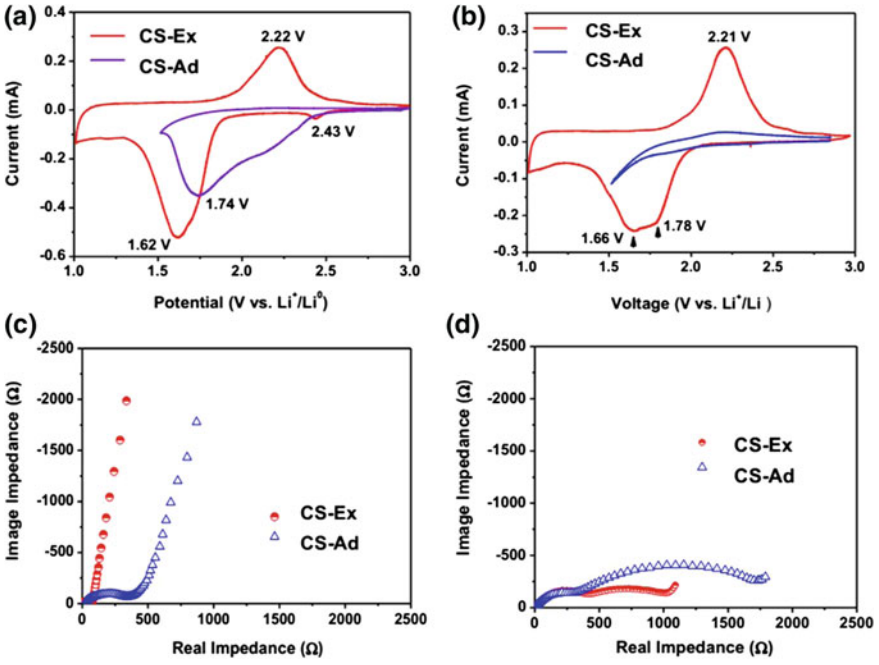


**Fig. 2.7** **a** First cycle CV and **b** second cycle CV curves of CS-Ex and CS-Ad cathodes recorded at 0.5 mV $s^{-1}$ at room temperature. EIS Nyquist profiles of CS-Ex and CS-Ad cathodes recorded from 10 kHz to 10 MHz at room temperature at cathode polarization potentials of **c** open circuit potential (2.8 V vs. $Li^+/Li^0$) and **d** full discharge potential (1.5 V vs. $Li^+/Li^0$) after discharge but before charge in the first cycle

reduction of polysulfide ions to insoluble $Li_2S_2$/$Li_2S$. In the CS-Ex cathode, the conversion of polysulfides to lithium sulfide occurs at around 1.8 V. The low potential reduction could be due to the extra electrode polarization required to overcome the nanoconfinement barrier of strong adsorption energy. In stark contrast, the cathodic reaction of CS-Ad initiates at 2.4 V and reaches the peak current at 1.74 V. Two slow plateaus are noticed with a transition point of about 2.2 V. The upper branch (2.4–2.2 V) indicates the formation of polysulfide ions from sulfur located in large pores. The lower oblique branch (2.2–1.74 V) originates from the slow kinetics of lithium sulfide formation on the outer surface [31]. The probable surface coverage by exterior lithium sulfide limits the full reduction of polysulfide ions and hinders the approach of electrons and ions to sulfur confined in micropores. The incomplete conversion of confined sulfur could be responsible for its higher peak potential (1.74 V, compared to 1.62 V of CS-Ex), where the reaction is actually terminated. As indicated in Fig. 2.7b, the second cycle of CS-Ad shows no current response, and clearly confirms the terminated cathode activity by exterior lithium sulfides. During the second cathodic reaction process, the major 1.62 V peak of CS-Ex was shifted to a higher potential within 1.66–1.78 V. This potential shifting is mainly attributed to the formation of complexes with lower adsorption energy after the first anodic oxidation of lithium sulfides.

The varying cathode performance is related to the pore size dependence of confinement, and is better understood by employing electrochemical impedance spectroscopy (EIS). As seen in Fig. 2.7c, the open circuit (2.8 V vs. $Li^+/Li^0$) EIS spectra of CS-Ad and CS-Ex both comprise a semicircle at high frequency and an inclined tail in the low-frequency region. The interfacial charge-transfer resistance recognizable from the semicircle is due to the redox formation of high-order polysulfides and low-order lithium sulfides. The monolayer adsorption of sulfur in micropores realizes a molecular-level intimate electronic contact with the carbon scaffold [32], while the bulky loading of sulfur in mesopores restricts efficient electron conduction with the carbon matrix. As a consequence, the CS-Ad cathode displays nearly four times greater resistance than the CS-Ex cathode. The mass transfer kinetics, mainly of lithium ions, inside the porous cathode can be compared qualitatively with reference to the slope of the low-frequency tail. The $CS_2$ extraction frees the occupied mesopores, and results in the facilitated ion transfer in the CS-Ex cathode with an increased tail slope. The combination of intimate electric connection and fast ionic transport as a result of selective confinement of sulfur in micropores is promising for developing a stable cathode with high-rate capability. EIS spectra recorded after discharge confirm the superior cathode kinetics of CS-Ex to those of CS-Ad, which is reasonably attributed to the absence of surface lithium sulfides due to the confined lithium sulfide formation in micropores (Fig. 2.7d).

The unconstrained dissolution of polysulfides in mesopores of the CS-Ad cathode caused the absolute loss of capacity in the second cycle (Fig. 2.8a). In contrast, the maximum discharge capacity of 1067 mAh $g_{sulfur}^{-1}$ was obtained from the CS-Ex cathode (Fig. 2.8b). Despite the reversible delithiation of the CS-Ex cathode, the discharge capacity in the second cycle is still higher than the charge capacity. Since the dissolution of polysulfide causes the active mass loss in the

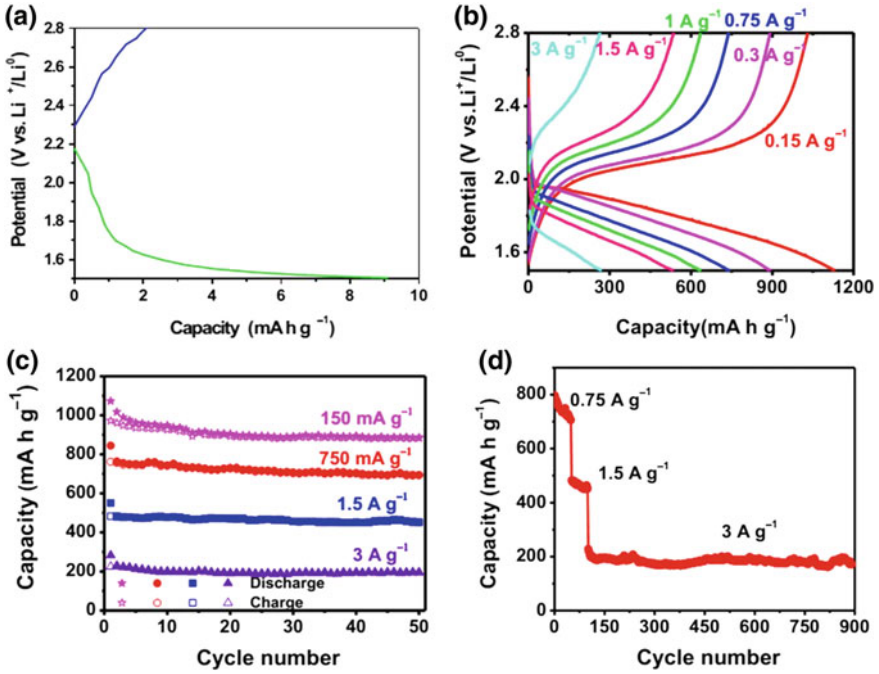


**Fig. 2.8** **a** The second cycle discharge–recharge profiles of CS-Ad, **b** the second cycle charge-discharge profiles of a CS-Ex at different current densities, **c** cycle stability of the CS-Ex cathode at high rates, and **d** cycling discharge capacity tested at 0.75 A $g^{-1}$, 1.5 A $g^{-1}$ and 3 A $g^{-1}$ for 900 cycles

cathode, this phenomenon suggests the presence of residual sulfur in mesopores of CS-Ex. As seen from Fig. 2.8c, however, the discharge–charge capacity remains nearly identical after the first few cycles and retains a Coulombic efficiency close to 100%. This implies that the majority of the sulfur was removed from mesopores by $CS_2$ and only trace amounts remained that formed polysulfides during the very initial cycles and dissolved. It is noticeable that no potential plateau exists in the discharge–charge profiles recorded at different current densities. This is very likely due to the use of carbonate electrolyte and the micropore confinement [24]. In addition, the micropore confinement formed sub-nanometre sulfur clusters. This extreme sizing effect might alter the normal physicochemical properties of sulfur which is relevant to the anomalous lithiation–delithiation behavior. The cycling stability of sulfur cathodes is shown in Fig. 2.8c. The capacity fade at the initial cycles is most likely due to the dissolution of the sulfur residue in mesopores as described above. Most importantly, a high-rate capacity of around 200 mAh $g_{sulfur}^{-1}$ under an ultrahigh current density of 3 A $g^{-1}$ for nearly 800 cycles was observed (Fig. 2.8d). This operation corresponds to a calculated discharge or recharge C rate of 1.8 C. It is evident that the micropores confer the stable performance of the sulfur cathode over the greatest number of cycles reported [33],

particularly in this aggressive carbonate electrolyte, while the graphitic structure and mesoporous texture contribute to the high-rate performance. We here emphasize that the micropore confinement and the combination of graphitic structure and mesoporous framework are critical to achieve such advanced performance. The micropore confinement effect is twofold. First, the micropores restrict the highly soluble polysulfides. Second, the polysulfides/lithium sulfide formed in micropores retains intimate electric contact with the mesoporous and conducting carbon matrix, and enhances reaction kinetics.

## 2.3 Mechanism Analysis of the Pore Size Dependence of Confinement on Electrochemical Performance in Li–S Batteries

Scanning electron microscopy (SEM) images of the CS-Ex cathode after discharge demonstrate the porous structure due to the confined lithium sulfides in micropores (Fig. 2.9a). However, the solid insulating lithium sulfide layer formed by the reduction of dissolved polysulfides covers the CS-Ad cathode surface (Fig. 2.9b). XPS analysis was used to study the surface composition of lithium sulfides confined in micropores and deposited on the outer surface. The $S2p_{3/2}$ spectra confirm the formation of lithium sulfide after the first discharge (Fig. 2.9c and d). The negative shifts of $S2p_{3/2}$ binding energy are observed for both cathodes. However, the lithium sulfides confined in micropores show a higher binding energy than the surface lithium sulfides. This difference could possibly indicate the short bond length of the lithium sulfide deposited in micropores compared to that on the outer surface without confinement.

We suggest a possible mechanism to understand the physical origin of the superior stability of micropore-confined sulfur even in the carbonate electrolyte. As generally accepted, the sulfur reduction is a solid (S)-liquid (polysulfide ions)-solid ($Li_2S_2/Li_2S$) process, and the mesopores stabilize sulfur through the adsorption of dissolved polysulfide ions (Fig. 2.10, left). The solvent-restricted environment and the solvent shell distortion of electrolyte ions in pores close to or less than 1 nm have recently been reported [34]. Here, we consider that micropores below 1 nm cause the desolvation of the electrolyte ions, and probably will prevent or at least slow the dissolution of polysulfide as the solvent concentration is very low or likely to be close to zero in these micropores (Fig. 2.10, right). This suggests a quasi-solid-state reaction of the sulfur under solvent-deficient conditions. Furthermore, the micropore confinement will also distort the solvation shells of polysulfide anions even if they are solvated and reduce the mobility of solvated polysulfide anions. Consequently the reduction of sulfur still produces polysulfides as intermediates, but the polysulfides remain in the pores instead of being dissolved. This inside micropore lithiation of sulfur gives rise to the micropore-confined lithium sulfides, and is the reason for the ultra-long cycling life with nearly 100% Coulombic efficiency.

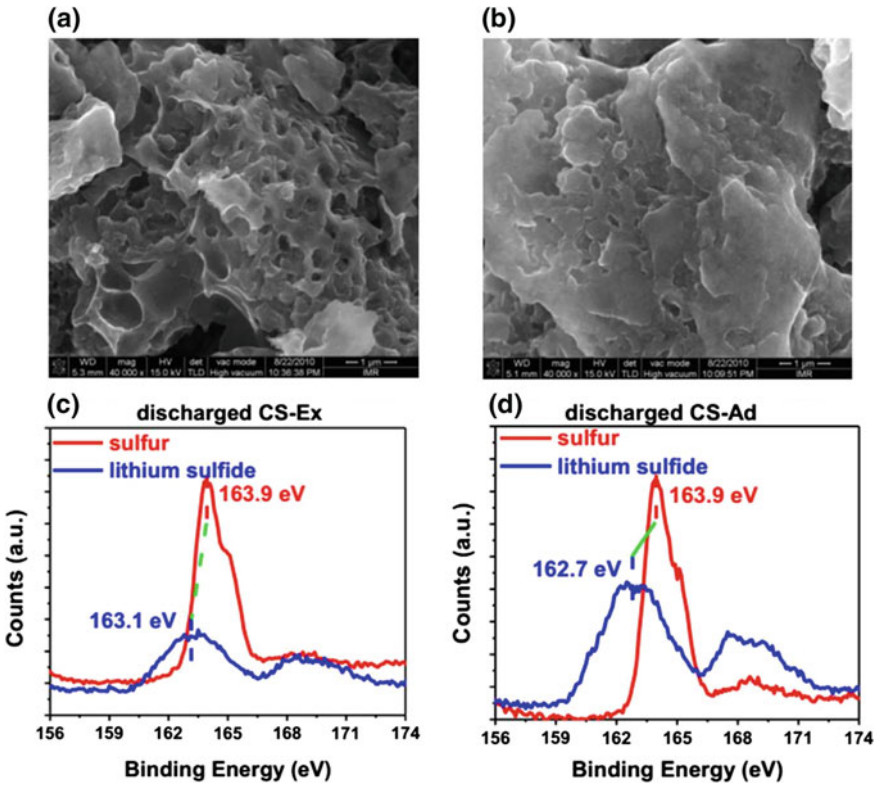


**Fig. 2.9** SEM images of **a** CS-Ex and **b** CS-Ad cathodes after the first discharge, and XPS $S2p_{3/2}$ profiles of **c** CS-Ex and **d** CS-Ad cathodes compared to the raw cathodes before discharge

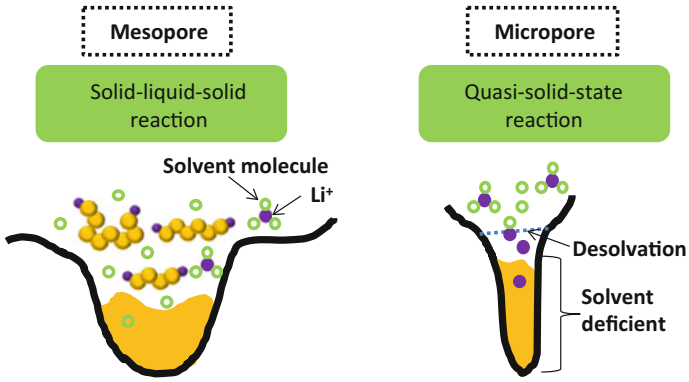


**Fig. 2.10** Illustration of the different reaction process of sulfur confined in mesopores and micropores. Reprinted with permission from Ref. [35]. Copyright 2013, Royal Society of Chemistry

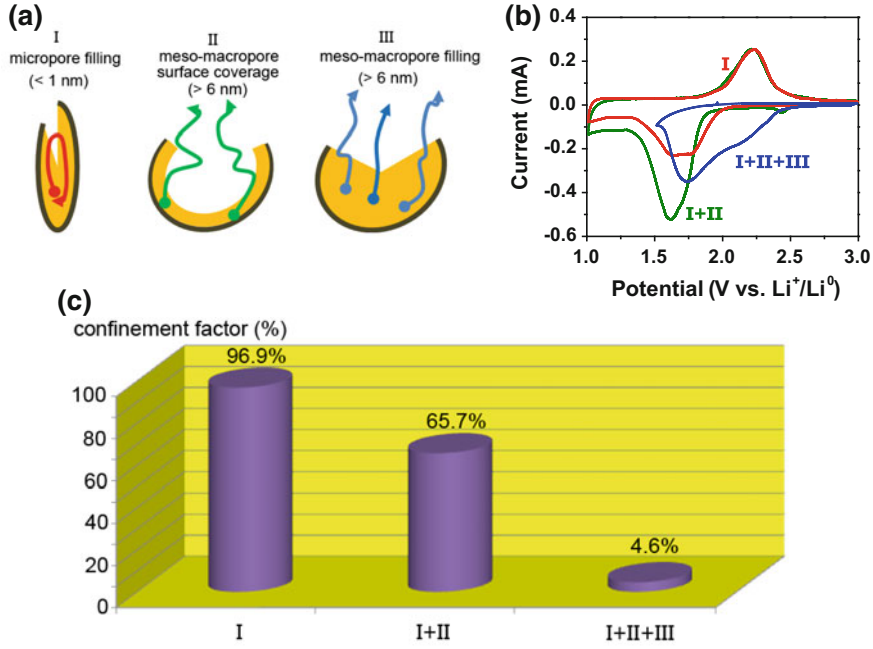


**Fig. 2.11** **a** Scheme showing three different confinement systems, **b** CV curves of sulfur cathodes with three different confinement systems, **c** confinement factors for the three typical confinement systems (color figure online)

We propose three modes of confinement of sulfur occur in these systems (Fig. 2.11a): (I) the micropore filling (<1 nm), (II) the meso/macropore surface coverage (>6 nm), and (III) the meso/macropore filling (>6 nm). CS-Ex exhibits I + II, while CS-Ad is regarded as showing I + II + III. Sulfur in super-micropores is neglected here due to its occurrence only in trace amounts which can be electrochemically removed. According to Fig. 2.11b, the nearly reversible reaction is observed for sulfur confined in sub-nanometre micropores (red line), while the sulfur located in meso/macropores caused the absolute loss of reversibility due to formation of an insulating layer on the electrode surface [36] (blue line). Sulfur adsorbed on the surfaces of meso/macropores also lacks reversibility (green line). Cyclic voltammetry can determine the amount of each sulfur species participating in the reactions. The ratio of anodic peak area to cathodic peak area, representative of the population of effectively confined polysulfides that can react reversibly, is defined here as the "confinement factor" to evaluate the capability of each condition to constrain polysulfides. It is obvious that a filling system comprising solely of micropores (I) gives a near-perfect confinement level (96.9%) compared to the other confinement systems (I + II, I + II + III) (Fig. 2.11c).

## 2.4 Conclusion

In this chapter, we have demonstrated the immobilization of sulfur in micropores of a mesoporous carbon framework with graphitic structure and the confined electrochemical transition of sulfur-polysulfides-lithium sulfides that promises durable sulfur cathodes for Li–S batteries. The beneficial integration of the micropores for sulfur lithiation, mesopores for ion transport, and graphitic structures for electron conduction substantially improves the performance in terms of the high-rate capacity and stability. It is remarkable that stable high-rate performance was attained in a mixed carbonate electrolyte that easily dissolves polysulfides. The main conclusions are as follows:

(1) Sulfur was selectively immobilized into the micropores of hierarchical porous carbon by a melt adsorption-solvent extraction process.
(2) Micropores in the hierarchical porous carbon have strong adsorption potential to confine sulfur, which acts as solvent-restricted reactors for sulfur lithiation.
(3) The localized electrochemical transition of "solid–solid" reaction instead of "sulfur-polysulfides-lithium sulfides" reaction was proposed through the desolvation effect in sub-nanometre pores.
(4) A "confinement factor" was defined for the capability to constrain polysulfides. It is obvious that a filling system comprising solely of micropores gives a near-perfect confinement level (96.9%) compared to the meso/macropore confinement systems (4.6%). The micropores restrict the highly soluble polysulfides and improve the sulfur utilization, and the cathode is able to operate reversibly over 800 cycles with marginal capacity loss at a rate of 3 A $g^{-1}$.

## References

1. Bruce PG, Freunberger SA, Hardwick LJ, Tarascon J-M (2012) Li–$O_2$ and Li–S batteries with high energy storage. Nat Mater 11(1):19–29
2. Ji XL, Lee KT, Nazar LF (2009) A highly ordered nanostructured carbon–sulphur cathode for lithium–sulphur batteries. Nat Mater 8(6):500–506
3. Manthiram A, Fu Y, Su Y-S (2012) Challenges and prospects of lithium–sulfur batteries. Acc Chem Res 46(5):1125–1134
4. Evers S, Nazar LF (2013) New approaches for high energy density lithium–sulfur battery cathodes. Acc Chem Res 46(5):1135–1143
5. Yang Y, Zheng G, Cui Y (2013) Nanostructured sulfur cathodes. Chem Soc Rev 42(7):3018–3032
6. Zhang C, Wu HB, Yuan C, Guo Z, Lou XW (2012) Confining sulfur in double-shelled hollow carbon spheres for lithium–sulfur batteries. Angew Chem Int Ed 51(38):9592–9595
7. Chung S-H, Manthiram A (2014) Carbonized eggshell membrane as a natural polysulfide reservoir for highly reversible Li–S batteries. Adv Mater 26(9):1360–1365
8. Shim J, Striebel KA, Cairns EJ (2002) The lithium/sulfur rechargeable cell—effects of electrode composition and solvent on cell performance. J Electrochem Soc 149(10):A1321–A1325

9. Marmorstein D et al (2000) Electrochemical performance of lithium/sulfur cells with three different polymer electrolytes. J Power Sources 89(2):219–226
10. Ryu HS et al (2006) Discharge behavior of lithium/sulfur cell with TEGDME based electrolyte at low temperature. J Power Sources 163(1):201–206
11. Shin JH, Cairns EJ (2008) N-Methyl-(n-butyl)pyrrolidinium bis(trifluoromethanesulfonyl) imide-LiTFSI-poly(ethylene glycol) dimethyl ether mixture as a Li/S cell electrolyte. J Power Sources 177(2):537–545
12. Choi YJ et al (2007) Electrochemical properties of sulfur electrode containing nano $Al_2O_3$ for lithium/sulfur cell. Phys Scripta T129:62–65
13. Song MS et al (2004) Effects of nanosized adsorbing material on electrochemical properties of sulfur cathodes for Li/S secondary batteries. J Electrochem Soc 151(6):A791–A795
14. Wang JL, Yang J, Xie JY, Xu NX (2002) A novel conductive polymer-sulfur composite cathode material for rechargeable lithium batteries. Adv Mater 14(13–14):963–965
15. Yang Y et al (2011) Improving the performance of lithium–sulfur batteries by conductive polymer coating. ACS Nano 5(11):9187–9193
16. Ji LW et al (2011) Porous carbon nanofiber-sulfur composite electrodes for lithium/sulfur cells. Energy Environ Sci 4(12):5053–5059
17. Zheng GY, Yang Y, Cha JJ, Hong SS, Cui Y (2011) Hollow carbon nanofiber-encapsulated sulfur cathodes for high specific capacity rechargeable lithium batteries. Nano Lett 11 (10):4462–4467
18. Elazari R, Salitra G, Garsuch A, Panchenko A, Aurbach D (2011) Sulfur-impregnated activated carbon fiber cloth as a binder-free cathode for rechargeable Li–S batteries. Adv Mater 23(47):5641–5644
19. Guo JC, Xu YH, Wang CS (2011) Sulfur-impregnated disordered carbon nanotubes cathode for lithium–sulfur batteries. Nano Lett 11(10):4288–4294
20. Cao YL et al (2011) Sandwich-type functionalized graphene sheet-sulfur nanocomposite for rechargeable lithium batteries. Phys Chem Chem Phys 13(17):7660–7665
21. Wang HL et al (2011) Graphene-wrapped sulfur particles as a rechargeable lithium-sulfur battery cathode material with high capacity and cycling stability. Nano Lett 11(7):2644–2647
22. Schuster J et al (2012) Spherical ordered mesoporous carbon nanoparticles with high porosity for lithium–sulfur batteries. Angew Chem Int Ed 51(15):3591–3595
23. Wang J et al (2008) Sulfur-mesoporous carbon composites in conjunction with a novel ionic liquid electrolyte for lithium rechargeable batteries. Carbon 46(2):229–235
24. Zhang B, Qin X, Li GR, Gao XP (2010) Enhancement of long stability of sulfur cathode by encapsulating sulfur into micropores of carbon spheres. Energy Environ Sci 3(10):1531–1537
25. Lai C, Gao XP, Zhang B, Yan TY, Zhou Z (2009) Synthesis and electrochemical performance of sulfur/highly porous carbon composites. J Phys Chem C 113(11):4712–4716
26. Gao J, Lowe MA, Kiya Y, Abruna HD (2011) Effects of liquid electrolytes on the charge–discharge performance of rechargeable lithium/sulfur batteries: electrochemical and in-situ X-ray absorption spectroscopic studies. J Phys Chem C 115(50):25132–25137
27. Aurbach D et al (2009) On the surface chemical aspects of very high energy density, rechargeable li–sulfur batteries. J Electrochem Soc 156(8):A694–A702
28. Hassoun J, Scrosati B (2010) A high-performance polymer tin sulfur lithium ion battery. Angew Chem Int Ed 49(13):2371–2374
29. Wang DW, Li F, Liu M, Lu GQ, Cheng HM (2008) 3D aperiodic hierarchical porous graphitic carbon material for high-rate electrochemical capacitive energy storage. Angew Chem Int Ed 47(2):373–376
30. Xin S et al (2012) Smaller sulfur molecules promise better lithium–sulfur batteries. J Am Chem Soc 134(45):18510–18513
31. Cheon SE et al (2003) Rechargeable lithium sulfur battery-II. Rate capability and cycle characteristics. J Electrochem Soc 150(6):A800–A805
32. Shinkarev VV, Fenelonov V, Kuvshinov GG (2003) Sulfur distribution on the surface of mesoporous nanofibrous carbon. Carbon 41(2):295–302

33. Wang D-W et al (2012) A microporous-mesoporous carbon with graphitic structure for a high-rate stable sulfur cathode in carbonate solvent-based Li–S batteries. Phys Chem Chem Phys 14(24):8703–8710
34. Chmiola J et al (2006) Anomalous increase in carbon capacitance at pore sizes less than 1 nanometer. Science 313(5794):1760–1763
35. Wang D-W et al (2013) Carbon–sulfur composites for Li–S batteries: status and prospects. J Mater Chem A 1(33):9382–9394
36. Cheon SE et al (2003) Rechargeable lithium sulfur battery-II. Rate capability and cycle characteristics. J Electrochem Soc 150(6):A800–A805

# Chapter 3
# Flexible Nanostructured Sulfur–Carbon Nanotube Cathode with High-Rate Performance for Li–S Batteries

## 3.1 Research Background

Flexible and wearable electronics, such as roll-up displays and implantable devices, have been emerging as an advanced technology for next-generation, high-performance portable electronic devices that require mechanical flexibility [1–4]. However, the use of these devices cannot be realized unless suitable flexible power sources are developed. LIBs are widely used in portable electronic devices due to their advantages of long life, high safety, and good environmental benignity, and are considered potential energy storage devices for flexible electronics [4–6]. Currently, flexible LIBs are limited by their poor mechanical properties and low energy density, due to the use of a metallic current collector, complex electrode fabrication processes, and intercalation electrode materials with low capacity [7–9]. For example, slurry-casting is commonly used for electrode fabrication, in which active materials, binders, and carbon conductive additives are cast onto a metallic foil current collector (Fig. 3.1a). Metallic foil is heavy and inactive and thus increases the weight and reduces the gravimetric energy density of batteries [4, 10]. For future flexible electronics, one of the major challenges is to achieve a mechanically robust, lightweight electrode without the compromise of electrochemical performance under frequent mechanical deformation for long time use [11–13]. Thus, the novel structural design of flexible electrodes and the choice of suitable substrate materials are urgently required (Fig. 3.1b).

On the other hand, the state-of-the-art electrode materials for LIBs with an energy density of less than 300 Wh $kg^{-1}$ are difficult to keep up with the increasing demand for high energy density [14, 15]. Therefore, there is an urgent need to develop novel battery structures by reducing the amount of inactive components in the electrodes and to explore new battery systems with multi-electron reactions to improve the energy density [3, 4, 16, 17]. Li–S batteries, with a two-electron



G. Zhou, *Design, Fabrication and Electrochemical Performance of Nanostructured Carbon Based Materials for High-Energy Lithium–Sulfur Batteries*, Springer Theses,
DOI 10.1007/978-981-10-3406-0_3

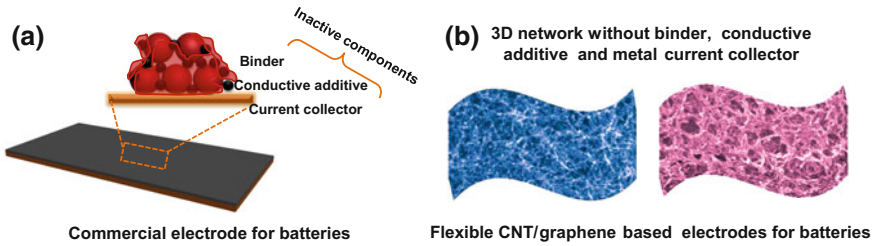


**Fig. 3.1** Schematic of **a** conventional and **b** flexible electrode components in lithium secondary batteries [4]

reaction during the electrochemical process, possess a high theoretical specific capacity and a high specific energy [18, 19] and are therefore regarded as one of the most promising energy storage devices in the near future [14, 20, 21]. However, in order to realize the practical applications of Li–S batteries, especially for flexible electronic devices, many challenges exist, such as the low sulfur utilization resulting from the insulation of sulfur/$Li_2S$, and lightweight, flexible electrode structure design [4, 22, 23]. For flexible electrode design, Aurbach et al. impregnated sulfur into the micropores of activated carbon fiber cloth to restrict polysulfide dissolution and used it as a free-standing electrode [24]; Hagen et al. prepared a high sulfur-loaded film electrode based on carbon nanotube-coated conductive carbon fibers to increase its energy density [25]; Zhang et al. proposed a flexible all-carbon structure of interlinked nanotubes as a cathode scaffold for high-rate Li–S batteries [13]; and Kaskel et al. reported a solvent-free, pressing/thermal treatment to produce highly flexible free-standing carbon–sulfur composite cathode membranes with a tunable sulfur loading and improved cycling stability [26]. However, to date, electrode materials with excellent mechanical properties and flexible prototype Li–S devices have been rarely demonstrated and realized.

Here, we report the synthesis of a nanostructured carbon–sulfur cathode, which consists of CNTs containing elemental sulfur (S-CNTs). We further demonstrate the excellent performance of the S-CNT cathode for Li–S batteries. Template-directed CVD of carbon and carbothermal reduction of sulfate were integrated to grow the S-CNTs, which were assembled into a membrane to be used as a binder-free, flexible cathode that requires no metal current collector. The adjustment of sulfate concentration allows tuning the sulfur content (23 and 50 wt% of sulfur) in final S-CNT cathodes (denoted as S-CNT-23 and S-CNT-50 in the following content). The S-CNT cathode is highly conductive (800 S $m^{-1}$, ~30 orders of magnitude higher than sulfur ($5 \times 10^{-28}$ S $m^{-1}$) and ~11 orders of magnitude higher than $LiFePO_4$ ($10^{-8}$ S $m^{-1}$) [27]) and mechanically strong (able to withstand a 10 MPa stress). The S-CNT cathode is mesoporous (15–20 nm) and has a high specific surface area (>600 $m^2$ $g^{-1}$). At a fast charge and discharge rate (6 A $g^{-1}$, equivalent to 36C for $LiFePO_4$), the overall cathode (considering the mass of both sulfur

and carbon) can deliver 163 mA h $g^{-1}$ (23 wt% S) and 260 mAh $g^{-1}$ (50 wt% S), which is comparable or higher than the theoretical capacity of 170 mAh $g^{-1}$ of $LiFePO_4$ [27]. Moreover, because sulfur is confined in the walls of the nanotubes, dissolution of polysulfides is restricted, which gives the material good cyclability. Combining the flexible S-CNT cathode with the flexible prelithiated silicon/graphene composite anode, we demonstrate a flexible prototype Li–S battery device for future practical application.

## 3.2 Design and Fabrication of Flexible Nanostructured S-CNT Cathode

### *3.2.1 Synthesis of S-Containing Anodic Aluminum Oxide (AAO) Template*

Free-standing AAO films were prepared by a typical two-step anodic oxidation method [28]. In the first step, a thin film of AAO was formed by anodizing an Al foil (purity: 99.99%) under 20 V in a 15 wt% sulfuric acid solution at 10 °C for 2 h. The as-formed AAO film was removed in a phosphochromic acid solution (6 wt% $H_3PO_4$ + 1.8 wt% $H_2CrO_4$ aqueous solution) at 60 °C. The remaining Al foil was anodized again for 4 h under the same conditions as in the first step. After the second step anodic oxidation, a free-standing AAO film was separated from the Al substrate by reversing the polarity of the cell voltage [29]. Finally, an AAO film with an average channel diameter of 25 nm was obtained with one face open that allows it to adsorb a large amount of sulfate.

### *3.2.2 Synthesis of S-CNTs Composites*

A film obtained using the above procedure was placed in a quartz tube which was inserted into a vertical tube furnace followed by heating to 650 °C under a high purity $N_2$ flow of 100 $cm^3$ $min^{-1}$. An acetylene gas flow was then introduced into the furnace at a rate of 10 $cm^3$ $min^{-1}$ for chemical vapour deposition of carbon and, at the same time, sulfate adsorbed in the film was reduced to sulfur (Fig. 3.2a). After 2 h deposition, the acetylene gas was turned off, and the temperature was gradually increased to 800 °C where it was held for 30 min. Subsequently, the furnace was cooled to room temperature under the protection of a $N_2$ flow. The resulting material was immersed in a HF aqueous solution to remove the AAO template leaving the S-CNTs.

### 3.2.3 Synthesis of CNTs

The synthesis process of CNTs is similar to that of S-CNTs, but the AAO template is synthesized in an aqueous containing 3 wt% oxalic acid at 40 V.

### 3.2.4 Fabrication of Flexible S-CNT Membranes

An ethanol evaporation-induced assembly technique was developed to produce flexible membranes from the S-CNTs. A dispersion of the S-CNTs in ethanol (0.5–2 mg $ml^{-1}$) was agitated with ultrasonication for 1 h. The evaporation of ethanol was slowly performed in an oven at 50 °C and an S-CNT membrane was collected from the bottom of the vessel.

## 3.3 Sulfur Formation Mechanism

The incorporation of sulfur in the AAO-templated CNTs is due to the carbothermal reduction of sulfate ($SO_4^{2-} + C \rightarrow S + CO + CO_2$) [30]. SEM images demonstrate the structural integrity of the S-CNTs, indicating a full replication from the AAO template (Fig. 3.2b). XPS S 2p profiles of the sulfate-containing AAO template, S-CNTs/AAO and S-CNTs are compared in Fig. 3.2c. Pure sulfur was used as a reference to show the S 2p binding energy of $S^0$. CNTs thermally reduce the sulfate ($SO_4^{2-}$) and forms pure sulfur ($S^0$) in the S-CNTs. The zero valence of elemental S in the S-CNTs suggests the absence of C–S bonds. It is worth noting that Kurmaev

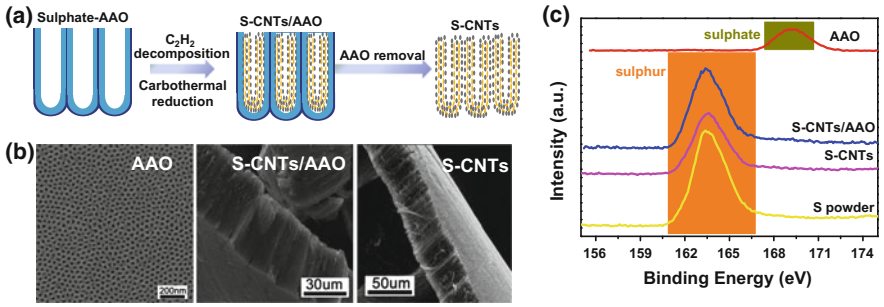


**Fig. 3.2** **a** Scheme showing the thermal decomposition of $C_2H_2$ in a sulfate-containing AAO template and the formation of S-CNTs after AAO removal. **b** SEM images showing the top view of a sulfate-containing AAO template, side views of S-CNTs/AAO and S-CNTs. **c** XPS spectra showing the change in composition from a sulfate-containing AAO to S-CNTs

et al. prepared sulfur-intercalated graphite at 400°C [31] and Guo et al. suggested the intercalation of sulfur into AAO-templated disordered CNTs by annealing sulfur with CNTs at 500 °C [32]. However, un-indexed peaks in the XRD profiles may suggest that some carbon–sulfur compounds are produced in Guo's sample [32]. In contrast, the S-CNTs prepared by the template-directed carbothermal approach are free from carbon–sulfur bonding and only consist of elemental carbon and sulfur without the formation of any carbon–sulfur compounds.

## 3.4 Characterization of S-CNTs

To elucidate the effect of the carbothermal formation of sulfur on the microstructure of carbon, Raman spectroscopy was used to study the D-/G-modes of the carbon lattice in the S-CNTs. As compared in Fig. 3.3a, the intensity of the D band in the S-CNT is much higher than that of sulfur-free CNTs that were prepared using sulfate-free AAO template (see Sect. 3.2.3), indicating that the structure of the S-CNTs is highly defective. The defects in graphene layers of the S-CNTs are formed due to the oxidation of carbon when reducing the sulfate. It is interesting that no vibration modes can be assigned to sulfur in the S-CNTs. This is quite distinct from pure sulfur powder, which has several signals below 500 $cm^{-1}$. This result agrees with XRD analysis (Fig. 3.3b), and both reveal the noncrystalline nature of sulfur in the S-CNTs.

Sulfur is prone to be amorphous or nanocrystalline when trapped in 3-nm mesopores [18] or in micropores [33], and this is consistent with our results. High-resolution transmission electron microscopy (HRTEM) was used to characterize the structure and the mesopores of the S-CNT (Fig. 3.4a). It is evident that the

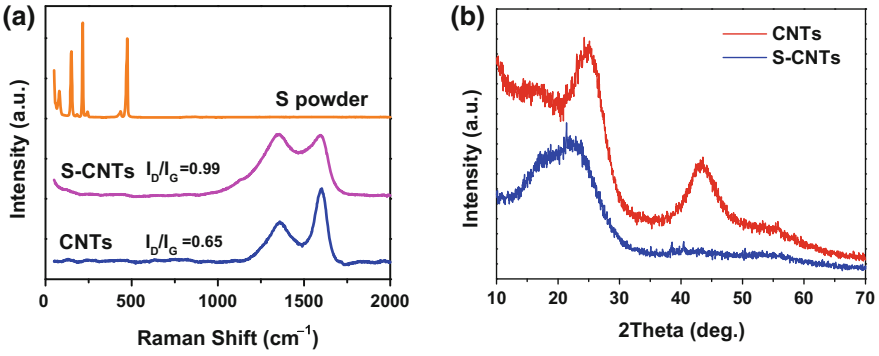


**Fig. 3.3** **a** Raman spectra of CNTs, pure sulfur powder, and the S-CNTs. **b** XRD patterns of the S-CNTs and the CNTs

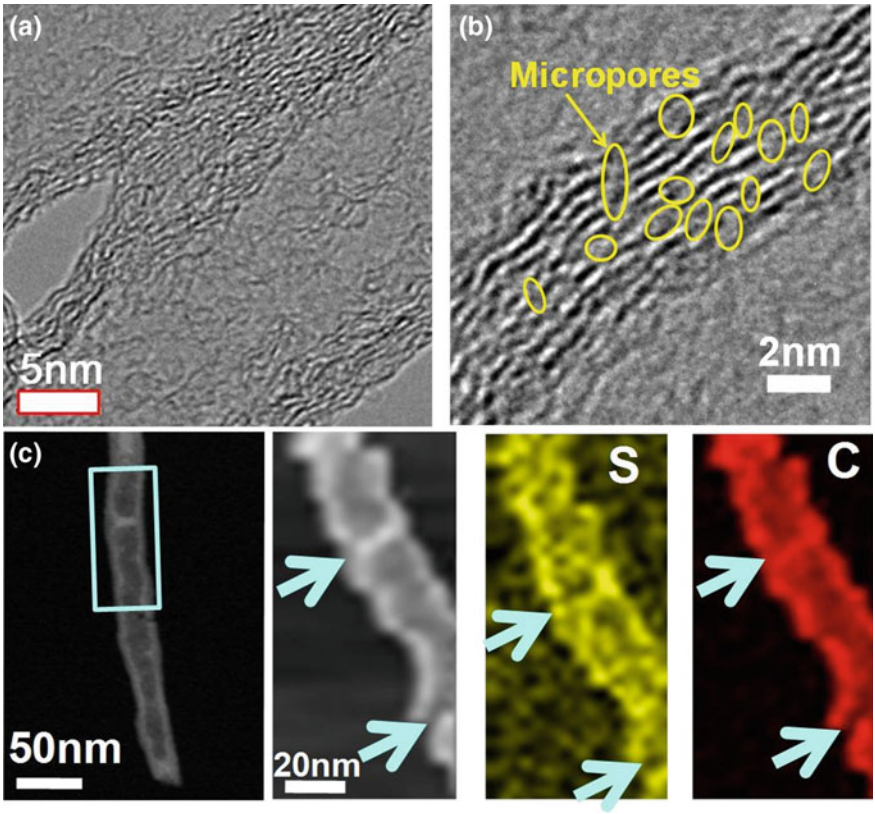


**Fig. 3.4** **a** HRTEM image of the microstructure of the S-CNT. **b** HRTEM image showing micropores (*circled*). **c** STEM analysis of a single S-CNT, the elemental mapping of sulfur and carbon

S-CNTs have defective walls as well as localized graphitic areas, and the mesoporous structure of the S-CNTs is confirmed. Meanwhile, micropores in S-CNT walls were observed, which are likely formed due to the oxidation of carbon, and sulfur is considered to be located inside these micropores in the walls (Fig. 3.4b). A scanning transmission electron microscope (STEM) was used to track the elemental distribution of carbon and sulfur in the S-CNT (Fig. 3.4c). The elemental mapping images show matched spatial distributions of sulfur and carbon (as marked by light blue arrows in Fig. 3.4c). The STEM intensity profiles across the projection of the S-CNT also show similar distributions of C-K edge and S-K edge signals (Fig. 3.5). Therefore, we consider that elemental sulfur is homogeneously distributed in the walls of the S-CNTs.

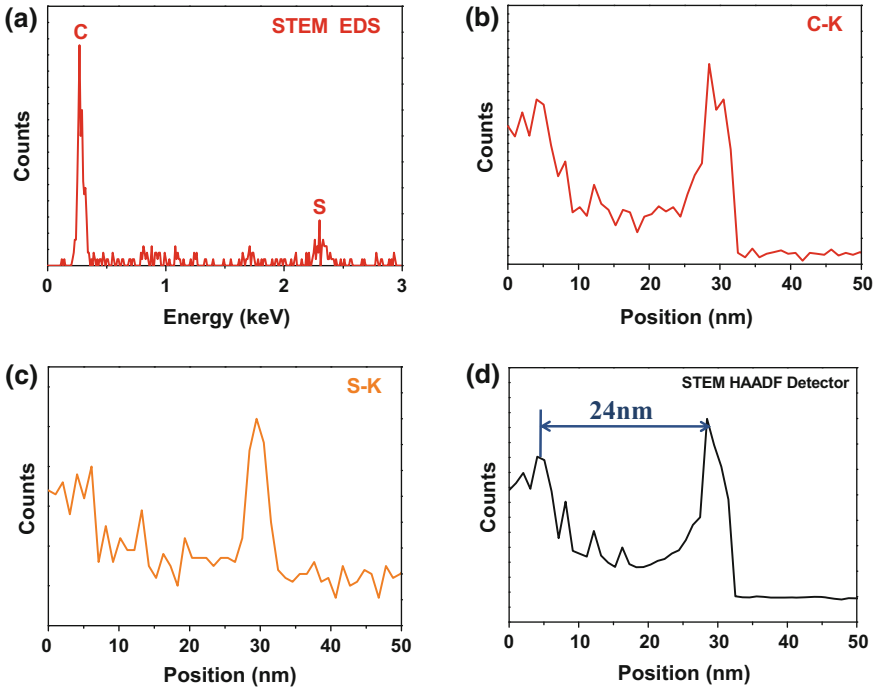


**Fig. 3.5** **a** EDS analysis of an S-CNT showing the presence of carbon and sulfur. **b**, **c** EDS line scanning of carbon and sulfur across an S-CNT. **d** HAADF line canning of an S-CNT

## 3.5 Control of the Sulfur Content in the S-CNTs

The weight percentages of sulfur in S-CNTs were 23 and 50% according to thermogravimetric analysis (Fig. 3.6) when the concentrations of sulfuric acid solution used were 15 wt% and 40 wt%, respectively.

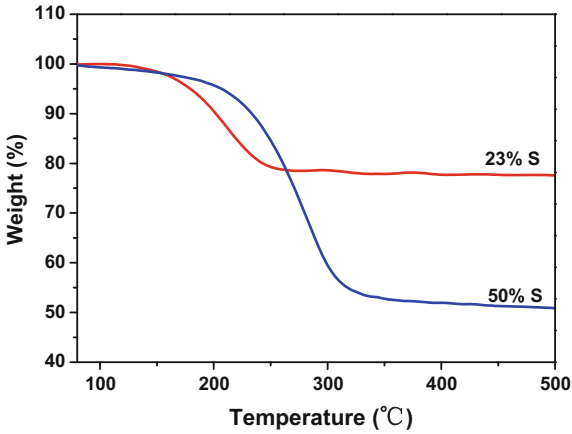


**Fig. 3.6** Thermogravimetric curve of the S-CNTs in Ar with a heating rate of 10 °C $min^{-1}$, indicating the sulfur content of 23.0 and 50.0 wt%

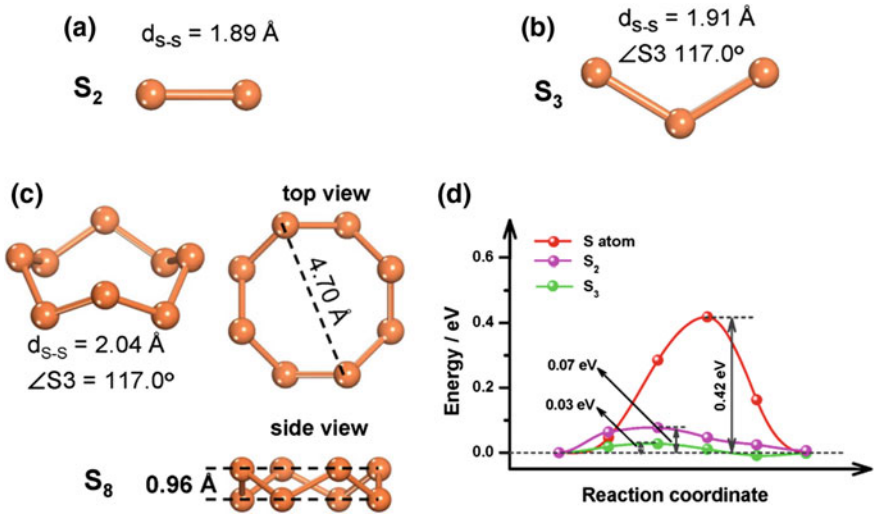


**Fig. 3.7** Structures of **a** $S_2$, **b** $S_3$, **c** $S_8$ molecules, and **d** the minimum energy paths for S atom (*red ball-line*), $S_2$ (*purple ball-line*) and $S_3$ (*green ball-line*) molecules diffusion within the nanoslits of 0.58–0.62 nm

## 3.6 First-Principles Calculations of the Sulfur Molecules Diffusion Within the Micropores

The sulfur insertion results in the formation of nanoslits and an expanded interlayer distance of graphene in S-CNT walls compared to the sulfur-free AAO-templated CNTs confirmed from XRD peak shift at around 26° (Fig. 3.3b). High temperature vaporized stable forms of sulfur are generally linear $S_2$ and planar $S_3$ molecules [34], which can freely infiltrate and near-freely diffuse within the nanoslits of 0.58–0.62 nm with negligible energy barriers (0.07 and 0.03 eV for $S_2$ and $S_3$, respectively) based on our first-principles calculations, subsequently form $S_8$ molecules when cooled down (Fig. 3.7), which are consistent with recent reported small sulfur molecule results [35].

## 3.7 Synthesis, Structure, and Performance of Flexible S-CNT Electrode

A flexible membrane made of the S-CNTs was prepared by ethanol evaporation-induced assembly (Fig. 3.8a). An S-CNT membrane with an interwoven nanotube network is of centimeter width and a few tens of micrometers thick (Fig. 3.8b, c), and is ready for use as a binder-free, flexible cathode that requires no metal current collector (inset of Fig. 3.8b). It can sustain a 10 MPa stress with a 9%

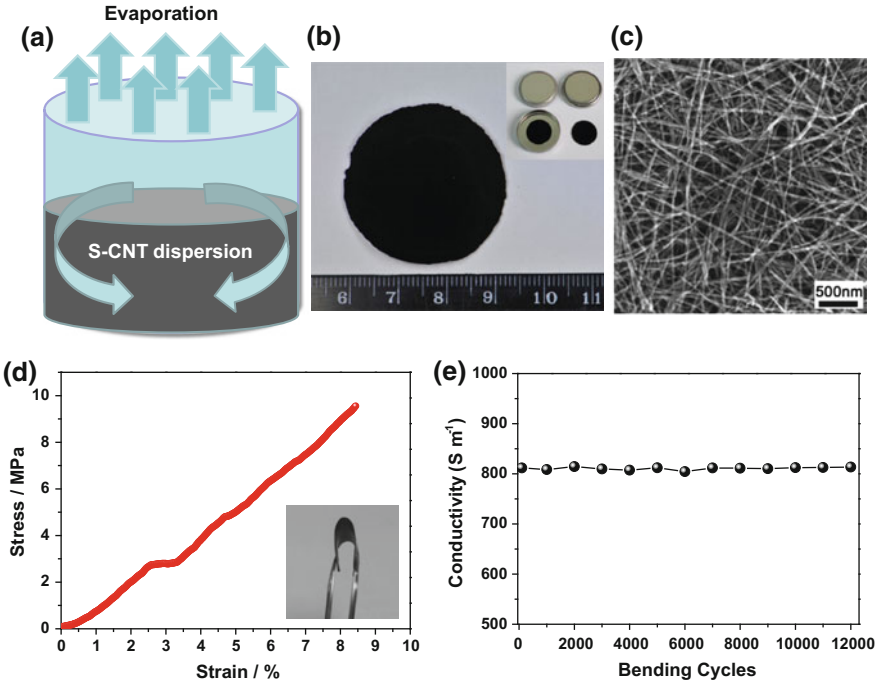


**Fig. 3.8** **a** Scheme showing the assembly of a flexible membrane by the evaporation of the S-CNT ethanol slurry. **b** Photograph of the S-CNT membrane. *Inset* photographs of a shaped circular S-CNT binder-free cathode in a 2032-type coin cell. **c** SEM image showing the interwoven S-CNT network in the membrane. **d** Stress–strain curve of a flexible S-CNT membrane cathode. Inset shows a bent S-CNT membrane. **e** Stability of the membrane in terms of electrical conduction over 12000 cycles

strain (Fig. 3.8d) and shows a high electrical conductivity of 800 S $m^{-1}$, which remains unchanged after 12,000 bend cycles (Fig. 3.8e). After bending 12,000 times, no cracks in the S-CNT membrane were observed, indicating an excellent flexibility and long-term durability of the conductive membrane. This flexible S-CNT cathode has the following advantages compared to pore-filled carbon–sulfur cathodes: (1) its capillary mesoporous structure can provide reservoirs to adsorb dissolved polysulfides [36, 37]; (2) its high surface area can reduce electrode polarization; (3) its high electrical conductivity can promote fast electron transfer from carbon to sulfur and improve the reduction kinetics of sulfur; (4) the micropore confinement of S in the S-CNT walls hinders polysulfide dissolution and results in long stability [17, 33]; and (5) its flexible and mechanically robust structure allows the fabrication of a binder-free and metal-current-collector-free electrode, which has the significant advantage of improving the energy density of the electrodes.

## 3.8 Electrochemical Performance of Flexible Nanostructured S-CNT Cathode

Coin cells with a lithium foil anode and a flexible S-CNT cathode were assembled to evaluate the electrochemical performance of S-CNTs. A model of and the structure of an S-CNT cathode are shown in Fig. 3.9. The kinetic processes of sulfur reduction and sulfide oxidation of the S-CNT-23 were studied using cyclic voltammetry (CV), as shown in Fig. 3.10a. There are three peaks in the first cathodic reduction process. The peak at 2.35 V (vs. $Li^+/Li^0$) corresponds to the reduction of elemental sulfur ($S_8$) to polysulfide anions ($S_x^{2-}$; $2 < x < 8$). A strong cathodic peak at 2.01 V (vs. $Li^+/Li^0$) suggests a strong reduction of soluble polysulfide anions to an insoluble low-order $Li_2S_2/Li_2S$ deposit. The small peak between the two main reduction peaks indicates the formation of medium-order polysulfides from high-order $S_x^{2-}$ [32]. The equilibrium lithiation potential of the S-CNT-23 is consistent with that of $S_8$, which confirms that zero valence sulfur in the S-CNT-23 has an 8-member crown structure [18]. The high reduction potential of $S_8$ indicates improved kinetics compared to the reduction potential of a micropore-filled $S_8$ cathode that has a high hysteresis [33]. The improved kinetics is caused by the conductive mesoporous structure that minimizes the barrier of electron transfer and lithium-ion migration. Cathodic reduction from the first to the fifth cycles remains almost constant despite a slight positive shift of potential, showing the excellent reduction kinetics of lithium sulfides from polysulfides. During the anodic oxidation of lithium sulfides to polysulfides, partial unconstrained dissolution of polysulfide ions causes a reduction in anodic current, which is stabilized after two cycles.

The galvanostatic charge/discharge behavior of the S-CNT-23 membrane cathode was evaluated at different current densities (from 0.15 to 6 A $g^{-1}$) within a potential window of 1.5–2.8 V versus $Li^+/Li^0$ (Fig. 3.10b). The membrane cathode can deliver a capacity of 1438 mAh $g^{-1}$ in sulfur and an overall capacity of

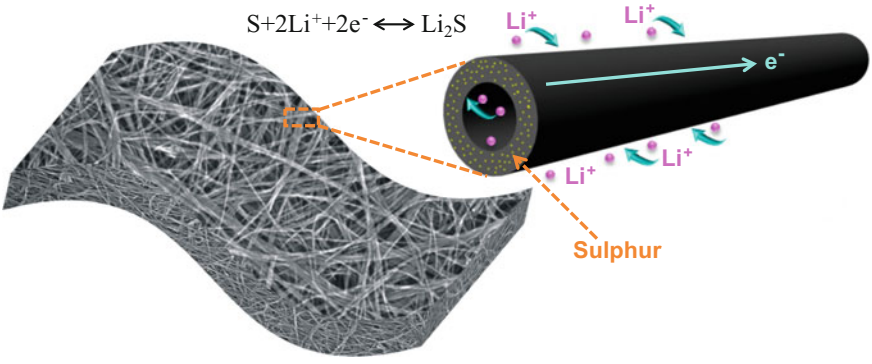


**Fig. 3.9** A model structure of the S-CNT cathode

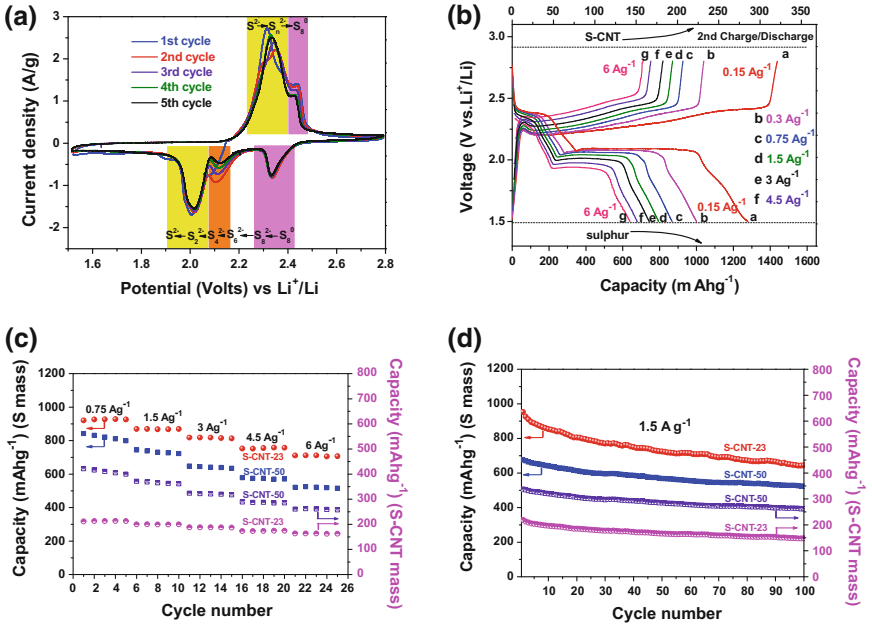


**Fig. 3.10** **a** Cyclic voltammograms at 0.1 mV $s^{-1}$ in the potential window from 1.5 to 2.8 V versus $Li^+/Li^0$. **b** Galvanostatic charge–discharge curves showing its rate-dependent specific capacity. **c** Rate capacity at different current densities of the S-CNT membrane cathodes. **d** Cycling stability of the S-CNT membrane cathodes at 1.5 A $g^{-1}$ for 100 cycles after the high-rate ability test, capacities shown in panels **c** and **d** are based on the sulfur weight (*left axis*) and S-CNT weight (*right axis*)

332 mAh $g^{-1}$ in sulfur and carbon at 0.15 A $g^{-1}$. As the discharge current density increases, the overall capacity gradually decreases and remains at 163 mAh $g^{-1}$ at 6 A $g^{-1}$, while the capacity at 6 A $g^{-1}$ based on the mass of sulfur is as high as 712 mAh $g^{-1}$ (Fig. 3.10c). The amount of sulfur in the S-CNT composites can be increased to 50 wt% by increasing the concentration of sulfuric acid solution. The capacity of sulfur in the S-CNT-50 is above 800 mAh $g^{-1}$ at 0.75 A $g^{-1}$ and can retain 520 mAh $g^{-1}$ at a high rate of 6 A $g^{-1}$. Although the capacity of this sample calculated on the sulfur content is lower than that of the S-CNT-23, its overall capacity is higher than that of the S-CNT-23 sample (Fig. 3.10c). This is due to the intimate contact of sulfur with carbon and the excellent electrical conductivity of the membrane that enables fast electron transfer. The entrapment of sulfur/(poly)-sulfides during cycling is vitally important for the stable utilization of sulfur cathodes. As demonstrated in Fig. 3.10d, the sulfur cathode can maintain reversible cathodic discharge/charge in the range of 1.5–2.8 V. After a 100-cycle stability test, the capacity of sulfur at 1.5 A $g^{-1}$ preserves as high as 653 and 524 mAh $g^{-1}$ (their overall capacities of the cathode are 150 and 262 mAh $g^{-1}$) for the S-CNT-23 and S-CNT-50, respectively.

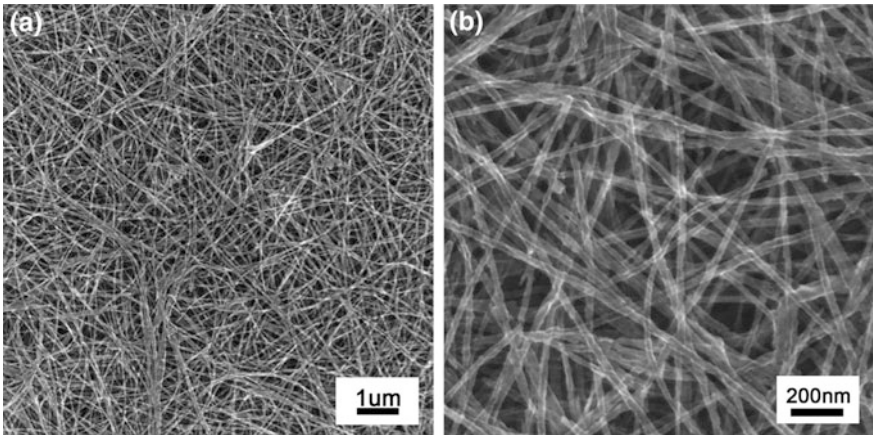


**Fig. 3.11** **a**, **b** SEM images of the S-CNT-50 membrane cathode after 100 charge–discharge cycles

To reveal the structural stability of the S-CNT membrane cathode, one cell of the S-CNT-50 was disassembled in the glove box, and the working electrode was taken out and washed three times using a dimethyl carbonate solution. Then it was transferred using a sealed container into the vacuum chamber of the SEM for structure characterization. As shown in Fig. 3.11, the overall morphology and structure of the S-CNT cathode material were well preserved, implying the excellent structural stability of the membrane electrode. Moreover, no precipitation from lithium sulfides was observed, which indicates the stability of sulfur confined in the walls of CNTs during lithiation/de-lithiation.

## 3.9 Fabrication of Flexible Silicon/Graphene Anode and Assembly of Flexible Li–S Full Battery Prototype

### *3.9.1 Fabrication of Flexible Silicon/Graphene Composite Film*

Graphene was prepared from natural flake graphite powder by chemical exfoliation as reported in our previous work [38]. Then graphene was placed in a quartz tube which was inserted into a tube furnace followed by heating to 500 °C under vacuum with a high purity $H_2$ flow of 40 $cm^3$ $min^{-1}$. A silane gas flow (10% $SiH_4$ + 90% $H_2$) was then introduced into the furnace at a rate of 10 $cm^3$ $min^{-1}$ for chemical vapour deposition of Si for 20 min. The silane gas was turned off, and the furnace was cooled to room temperature under the protection of a $H_2$ flow. The resulting material was Si/graphene composite with silicon nanoparticles (10 nm in

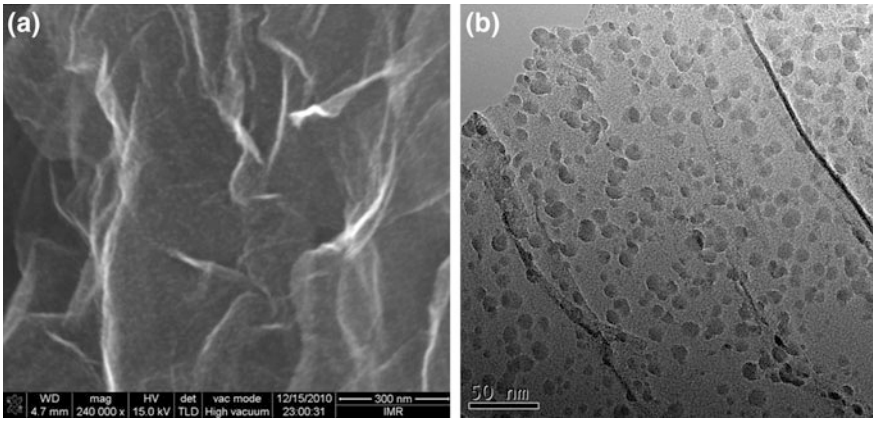


**Fig. 3.12** **a**, **b** SEM and TEM images of the Si/graphene composites

size) uniformly anchored on the surface of graphene, as confirmed by SEM and TEM (Fig. 3.12). The Si/graphene composite powder (30 mg) was dispersed in 50 mL N-methyl-2-pyrrolidone to form a suspension. The suspension was subsequently vacuum filtered using a Nylon membrane with a pore size of 0.44 μm. After fully drying at 90 °C for 30 min, the Si/graphene membrane could be easily peeled from the filter surface and used as a flexible anode material (Fig. 3.13).

### *3.9.2 Fabrication of Flexible Prelithiated Silicon/Graphene Composite Film*

The prelithiated silicon/graphene composite film was prepared according to the reported method [39] to provide lithium source for the full battery device. Prelithiation and cell assembly were carried out inside an Ar-filled glovebox. The silicon/graphene composite film was directly attached to a piece of Li metal foil (0.38 mm thick, Sigma-Aldrich Co.) and several drops of electrolyte were added between them. The electrolyte was made by adding 1 vol.% vinylene carbonate (Novolyte Technologies) into 1.0 M $LiPF_6$ in 1:1 w/w EC/DEC. Glass slides were used to sandwich the structure, and pressure was applied onto the two sides by using two binder clips. After 12 h of prelithiation, silicon/graphene composite film was peeled off from the Li foil carefully and washed with acetonitrile to remove the residual electrolyte and lithium salts. The obtained prelithiated silicon/graphene composite film can be used to assemble flexible Li–S full battery prototype.

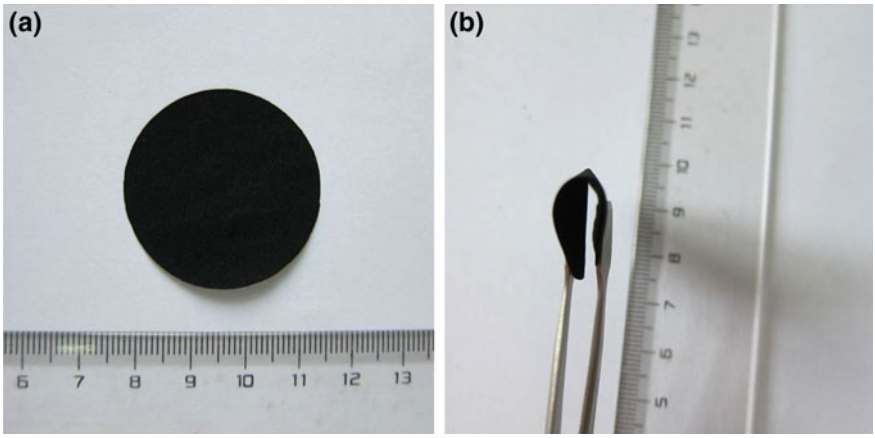


**Fig. 3.13** **a** Photograph of the Si/graphene composite film. **b** Photograph of a bent Si/graphene composite film

### *3.9.3 Assembly of Flexible Li–S Full Battery Prototype*

In order to verify the feasibility of this flexible electrode design, we fabricated a flexible prototype Li–S battery with S-CNT cathode and prelithiated silicon/graphene composite anode with separator between them. Both electrodes were sealed in adhesive tape packaging, Al foil and Cu foil were used as the electrode tabs (0.5 cm × 8 cm), as shown in Fig. 3.14a. The battery was light and flexible, and able to power a red light-emitting diode (LED) when it was flatted or bent (Fig. 3.14b, c), showing its great potential for powering flexible electronics.

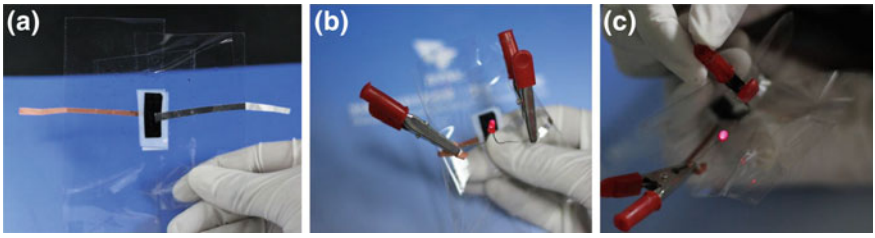


**Fig. 3.14** **a** Photograph of an assembled CNT-S//Si/graphene full battery, lighting a *red* LED device under flat **b** and bending **c** state

## 3.10 Conclusion

In this chapter, we developed a flexible cathode made from CNTs containing elemental sulfur which were synthesized by template-directed chemical vapour deposition, carbon thermo-reduction, and ethanol evaporation-induced assembly. This binder-free and metal-current-collector-free flexible cathode demonstrates the beneficial integration of a highly conductive CNT matrix, the strong confinement of elemental sulfur in CNT walls, and a mesoporous structure for fast ion migration. More significantly, it demonstrates a high-rate performance due to greatly improved cathode kinetics. We proposed a flexible Li–S full cell consisting of flexible pre-lithiated silicon/graphene membrane anode material and S-CNT cathode material. The main conclusions are as follows:

(1) Template-directed chemical vapour deposition and carbon thermo-reduction of sulfate strategy were developed for synthesizing CNTs with sulfur in the wall.
(2) Combined with first-principles calculations, it was found that sulfur exists as short-chain-like molecules ($S_{2–4}$) in sub-nanometre pores rather than cyclo-$S_8$ molecules in the pores with a size larger than 1 nm.
(3) A binder-free and metal-current-collector-free flexible cathode was prepared by ethanol evaporation-induced assembly for Li–S batteries. The membrane cathode can sustain a 10 MPa stress with a 9% strain and shows a high electrical conductivity of 800 S $m^{-1}$, which remains unchanged after 12,000 bend cycles.
(4) The micropore confinement of sulfur in the S-CNT walls hinders polysulfide dissolution and accommodates the large volumetric expansion of sulfur during lithiation, resulting in long cycling stability.
(5) The flexible full cell with S-CNT cathode and prelithiated silicon/graphene composite anode can work well under flat and bent states, indicating this S-CNT cathode material and the assembly are potentially adaptable for flexible Li–S batteries and other flexible energy storage devices.

## References

1. Kwon YH et al (2012) Cable-type flexible lithium ion battery based on hollow multi-helix electrodes. Adv Mater 24(38):5192–5197
2. Gwon H et al (2014) Recent progress on flexible lithium rechargeable batteries. Energy Environ Sci 7(2):538–551
3. Lee S-Y et al (2013) Progress in flexible energy storage and conversion systems, with a focus on cable-type lithium-ion batteries. Energy Environ Sci 6:2414–2423
4. Zhou G, Li F, Cheng H-M (2014) Progress in flexible lithium batteries and future prospects. Energy Environ Sci 7:1307–1338
5. Tarascon JM, Armand M (2001) Issues and challenges facing rechargeable lithium batteries. Nature 414(6861):359–367

6. Bruce PG, Scrosati B, Tarascon JM (2008) Nanomaterials for rechargeable lithium batteries. Angew Chem Int Ed 47(16):2930–2946
7. Bruce PG, Freunberger SA, Hardwick LJ, Tarascon J-M (2012) Li-$O_2$ and Li-S batteries with high energy storage. Nat Mater 11(1):19–29
8. Nishide H, Oyaizu K (2008) Materials science—toward flexible batteries. Science 319 (5864):737–738
9. Xiao Q, Zhang Q, Fan Y, Wang X, Susantyoko RA (2014) Soft silicon anodes for lithium ion batteries. Energy Environ Sci 7(7):2261–2268
10. Hu LB, Wu H, La Mantia F, Yang YA, Cui Y (2010) Thin, flexible secondary Li-ion paper batteries. ACS Nano 4(10):5843–5848
11. Liu S et al (2013) A flexible $TiO_2$(B)-based battery electrode with superior power rate and ultralong cycle life. Adv Mater 25(25):3462–3467
12. Zhou GM et al (2014) A graphene–pure-sulfur sandwich structure for ultrafast, long-life lithium-sulfur batteries. Adv. Mater 26(4):625–631
13. Huang J-Q et al (2014) Flexible all-carbon interlinked nanoarchitectures as cathode scaffolds for high-rate lithium-sulfur batteries. J Mater Chem A 2(28):10869–10875
14. Noorden RV (2014) The rechargeable revolution: a better battery. Nature 507:26–28
15. Zu CX, Li H (2011) Thermodynamic analysis on energy densities of batteries. Energy Environ Sci 4(8):2614–2624
16. Gao XP, Yang HX (2010) Multi-electron reaction materials for high energy density batteries. Energy Environ Sci 3(2):174–189
17. Wang D-W et al (2012) A microporous-mesoporous carbon with graphitic structure for a high-rate stable sulfur cathode in carbonate solvent-based Li-S batteries. Phys Chem Chem Phys 14(24):8703–8710
18. Ji XL, Lee KT, Nazar LF (2009) A highly ordered nanostructured carbon-sulphur cathode for lithium-sulphur batteries. Nat Mater 8(6):500–506
19. Wang D-W et al (2013) Carbon-sulfur composites for Li-S batteries: status and prospects. J Mater Chem A 1(33):9382–9394
20. Yang Y, Zheng G, Cui Y (2013) Nanostructured sulfur cathodes. Chem Soc Rev 42 (7):3018–3032
21. Manthiram A, Fu Y, Chung S-H, Zu C, Su Y-S (2014) Rechargeable lithium-sulfur batteries. Chem Rev 114(23):11751–11787
22. Evers S, Nazar LF (2013) New approaches for high energy density lithium-sulfur battery cathodes. Acc Chem Res 46(5):1135–1143
23. Manthiram A, Fu Y, Su Y-S (2012) Challenges and prospects of lithium-sulfur batteries. Acc Chem Res 46(5):1125–1134
24. Elazari R, Salitra G, Garsuch A, Panchenko A, Aurbach D (2011) Sulfur-impregnated activated carbon fiber cloth as a binder-free cathode for rechargeable Li-S batteries. Adv Mater 23(47):5641–5644
25. Hagen M et al (2013) Development and costs calculation of lithium–sulfur cells with high sulfur load and binder free electrodes. J Power Sources 224:260–268
26. Thieme S et al (2013) High capacity micro-mesoporous carbon-sulfur nanocomposite cathodes with enhanced cycling stability prepared by a solvent-free procedure. J Mater Chem A 1(32):9225–9234
27. Yuan LX et al (2011) Development and challenges of $LiFePO_4$ cathode material for lithium-ion batteries. Energy Environ Sci 4(2):269–284
28. Masuda H, Satoh M (1996) Fabrication of gold nanodot array using anodic porous alumina as an evaporation mask. Jpn J Appl Phys 35(1B):L126–L129
29. Kyotani T, Tsai LF, Tomita A (1996) Preparation of ultrafine carbon tubes in nanochannels of an anodic aluminum oxide film. Chem Mater 8(8):2109–2113
30. Cameron JH, Grace TM (1983) Kinetic-study of sulfate reduction with carbon. Ind Eng Chem Fund 22(4):486–494
31. Kurmaev EZ, Galakhov AV, Moewes A, Moehlecke S, Kopelevich Y (2002) Interlayer conduction band states in graphite-sulfur composites. Phys Rev B 66(19)

32. Guo JC, Xu YH, Wang CS (2011) Sulfur-impregnated disordered carbon nanotubes cathode for lithium-sulfur batteries. Nano Lett 11(10):4288–4294
33. Zhang B, Qin X, Li GR, Gao XP (2010) Enhancement of long stability of sulfur cathode by encapsulating sulfur into micropores of carbon spheres. Energy Environ Sci 3(10):1531–1537
34. Meyer B (1976) Elemental sulfur. Chem Rev 76(3):367–388
35. Xin S et al (2012) Smaller sulfur molecules promise better lithium-sulfur batteries. J Am Chem Soc 134(45):18510–18513
36. Ji X, Evers S, Black R, Nazar LF (2011) Stabilizing lithium–sulphur cathodes using polysulphide reservoirs. Nat Commun 2:325–331
37. Schuster J et al (2012) Spherical ordered mesoporous carbon nanoparticles with high porosity for lithium-sulfur batteries. Angew Chem Int Ed 51(15):3591–3595
38. Wu ZS et al (2009) Synthesis of high-quality graphene with a pre-determined number of layers. Carbon 47(2):493–499
39. Liu NA, Hu LB, McDowell MT, Jackson A, Cui Y (2011) Prelithiated silicon nanowires as an anode for lithium ion batteries. ACS Nano 5(8):6487–6493

# Chapter 4
# Fibrous Hybrid of Graphene and Sulfur Nanocrystals for High-Performance Lithium–Sulfur Batteries

## 4.1 Research Background

As discussed in the previous chapters, the practical application of Li–S batteries is greatly hampered by high solubility of the reaction polysulfide products which can shuttle between the anode and cathode forming deposits of solid $Li_2S_2$ and $Li_2S$ on the cathode [1, 2]. Extensive studies, including our previous two chapters, have been carried out to physically confine the sulfur in the pores of carbon matrix to alleviate the impact of the polysulfide shuttle. However, physical confinement has some limitations, these porous carbon materials show good interaction with sulfur, while weak interaction with lithium polysulfides and $Li_2S$ is observed where the final $Li_2S$ detaches from the carbon materials [3], leading to low utilization of the sulfur and a severe degradation of cycle life, this means physical confinement alone is not sufficient.

It is worth noting that the surface chemistry of carbonaceous materials has been recently recognized as another important aspect affecting the performance of Li–S batteries. Therefore, we introduce chemical interaction with sulfur species to improve the performance of Li–S battery. The core of this idea is change "sulfiphobic" conductive matrix to "sulfiphilic" conductive matrix. Oxygen functional groups are commonly used to improve the hydrophobic properties of carbon materials, such as oxygen plasma and acid treatment. Inspired by these, our consideration is to hold sulfur through oxygen functional group. As we know, GO has a lot of oxygen-containing functional groups, but the electric conductivity is relatively low [4]. Moreover, graphene layers are prone to agglomerate during the reduction and drying process because of strong π-π stacking and hydrophobic interactions [5]. Consequently, many unique properties of graphene are significantly compromised or even unavailable. Self-assembly of graphene into macroscopic materials can translate the intriguing properties of graphene into the resulting



G. Zhou, *Design, Fabrication and Electrochemical Performance of Nanostructured Carbon Based Materials for High-Energy Lithium–Sulfur Batteries*, Springer Theses,
DOI 10.1007/978-981-10-3406-0_4

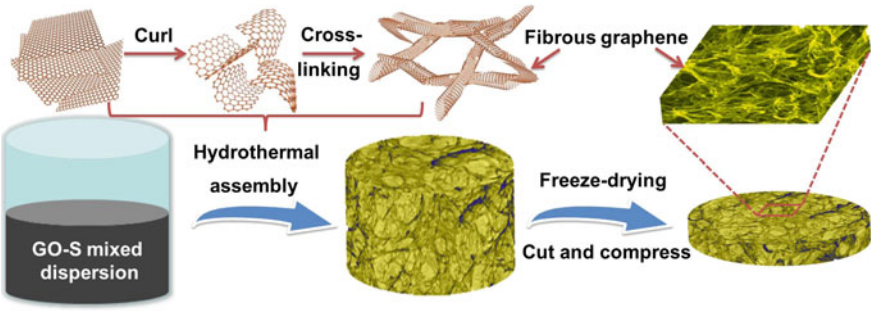


**Fig. 4.1** Illustration of the formation process of the G–S hybrid as a self-supporting electrode

macrostructures for practical applications [6, 7]. When used as electrodes, these well-defined interpenetrating structures provide macroscopic graphene materials with a large surface area, high mechanical strength, and fast mass and electron transport due to the combination of a porous structure and excellent intrinsic properties of graphene [8–11].

In this chapter, we have prepared a cathode, which is a self-supporting fibrous graphene–sulfur (G–S) hybrid with good electrical conductivity. We developed a one-pot strategy using the hydrothermal reduction of GO and its self-assembly with sulfur nanocrystals precipitated from a sulfur/carbon disulfide ($CS_2$)/alcohol mixed solution. This method has the merit of easy control over the amount of sulfur, uniform distribution of the sulfur nanocrystals, and tight contact of the sulfur with graphene. It can be cut and pressed into plates for direct use as Li–S battery electrodes without metal current-collector, binder and conductive additive, as illustrated in Fig. 4.1. The fibrous graphene facilitates electron transfer, and porous networks resulting from the interconnected graphene allow for rapid ion transport and the sulfur nanocrystals provide short $Li^+$ diffusion distances. Our experimental observations, combined with first-principles calculations, demonstrate that the dissolution/diffusion of polysulfide anions in the electrolyte can be greatly reduced by the strong binding of sulfur to the oxygen-containing (mainly hydroxyl/epoxide) groups on reduced graphene oxide, resulting in improved cyclic stability.

## 4.2 Material Fabrication and Structure

### *4.2.1 Synthesis of GO*

GO was synthesized from natural flake graphite by a modified Hummers' method [12]. The concentration of the GO suspension obtained was 1.8 mg $mL^{-1}$, which was determined by drying the suspension at 90 °C under vacuum for 24 h and then weighing the dried GO.

### 4.2.2 Synthesis of Intercalation Exfoliated Graphene

Intercalation exfoliated graphene powder was fabricated by Sichuan Jinlu Group Co., Ltd. using a solid-state intercalation and liquid-phase expansion and exfoliation method, and was used as-received in this work [13].

### 4.2.3 Synthesis of the Thermal Exfoliated-Reduced Graphene

Thermal exfoliated-reduced graphene was prepared as reported in our previous work [14].

### 4.2.4 Preparation of G–S Hybrids

G–S hybrids were prepared by hydrothermal reduction-assembly of GO with a sulfur-dissolving $CS_2$ and alcohol solution. In brief, 50 mL of the GO aqueous dispersion and 15 mL alcohol were mixed, and then 3 mL $CS_2$ containing 100, 150, and 200 mg of dissolved sulfur (tuning the sulfur content in the samples) was added to the GO dispersion. The mixture was stirred for 90 min and then sealed in an 80 mL Teflon-lined stainless steel autoclave for a hydrothermal reaction at 180 °C for 10 h. The black cylinder of G–S hydrogel was washed by ethanol and distilled water and the wet hydrogel was then freeze-dried to obtain the G–S hybrids (Fig. 4.1).

### 4.2.5 Preparation of G–S Hybrids (Powder)

G–S hybrids (powder) were prepared by mixing 90 mg intercalation exfoliated graphene and thermal exfoliated-reduced graphene with 150 mg sulfur under the same hydrothermal conditions as the G–S hybrids.

### 4.2.6 Preparation of G–$S_{mix}$

The G–$S_{mix}$ was prepared by mixing 50 mL of the GO aqueous dispersion, 15 mL alcohol, and 150 mg sulfur under the same conditions but without $CS_2$.

## 4.2.7 Structure Characterization of the Composites

### 4.2.7.1 Effect of Graphene Precursor on Tuning the Morphology and Sulfur Contents

Figure 4.2 shows typical photographs of the as-prepared materials. Sample I, made from GO and sulfur as precursors without the addition of a $CS_2$ solution shows a rough surface, and yellow sulfur agglomerates can be clearly observed on the surface of the G–S mixture (G–$S_{mix}$). In contrast, for samples II to IV, the G–S assembled hybrids fabricated from GO, sulfur-dissolving $CS_2$ (adding 100, 150, and 200 mg sulfur, respectively) and alcohol dispersion show a smooth surface, and their volume is almost independent of sulfur loading. The sulfur contents in the sample II–IV are 55, 63, and 71 wt% according to thermogravimetric analysis (TGA, Fig. 4.3, denoted as G–S55, G–S63, and G–S71). These results indicate that the alcohol acts to improve the miscibility of the sulfur/$CS_2$ and the GO aqueous solution and plays an important role in the formation of homogeneous G–S hybrids.

### 4.2.7.2 Effect of Oxygen Functional Groups on Tuning the Material Morphology and Structure

GO is also an important precursor because if we synthesize G–S hybrids from intercalation exfoliated graphene with a very small amount of oxygen functional groups (C/O = 38.9) and from thermal exfoliated-reduced graphene with a medium amount of oxygen functional groups (C/O = 10.6) after the hydrothermal process with the same amount of sulfur in the mixed solution, only G–S hybrids (powder) were obtained (Fig. 4.4a). After freeze-drying, the G–S hybrids (powder) were collected and the weight percentage of sulfur in the hybrid powder tested by TGA was 60 and 59 wt% [Fig. 4.4b, denoted as G–S60 hybrid (powder) and G–S59 hybrid (powder)].

The G–S hybrid materials have an interconnected porous network resulting from the fibrous graphene, as shown in Fig. 4.5a–c. The width of the fibrous graphene is


**Fig. 4.2** Photographs of the as-prepared (*I*) G–$S_{mix}$ using GO and sulfur as precursors and (*II*)–(*IV*) G–S hybrids using GO, sulfur-dissolving $CS_2$, and alcohol dispersion as precursors, after hydrothermal treatment at 180 °C for 10 h

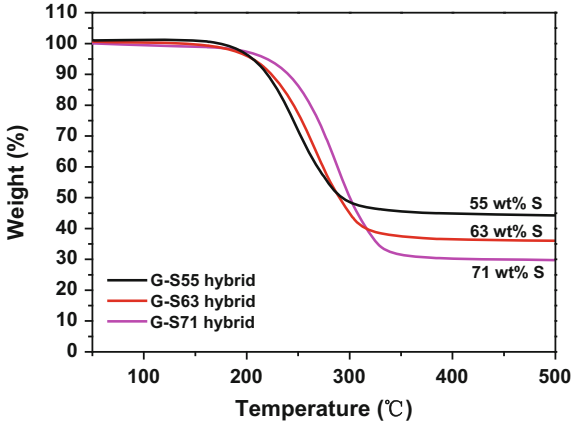


**Fig. 4.3** Thermogravimetric curves of the G–S hybrids in Ar with a heating rate of 10 °C $min^{-1}$, indicating the sulfur contents of 55, 63, and 71 wt%

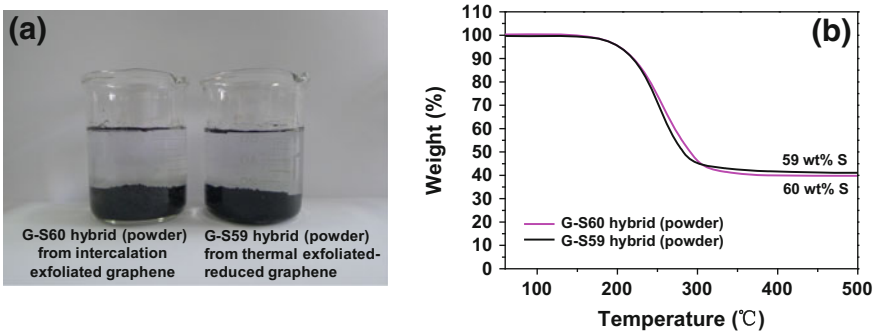


**Fig. 4.4** **a** Photograph of the as-prepared G–S hybrids (powder) using intercalation exfoliated graphene and thermal exfoliated-reduced graphene with sulfur-dissolving $CS_2$ and alcohol dispersion as precursors after hydrothermal treatment at 180 °C for 10 h. **b** Thermogravimetric curves of the G–S hybrids (powder) in Ar with a heating rate of 10 °C $min^{-1}$

1–2 micrometers, and the porous networks consist of stacked graphene flakes indicating that GO sheets were rolled up into a cross-linking fibrous structure during the hydrothermal process (Fig. 4.1). In contrast, the SEM image of the G–$S_{mix}$ (sample I) shows strongly aggregated graphene with a loose structure and many large pores (several tens of micrometers in diameter, Fig. 4.5d). However, the sulfur tends to spontaneously agglomerate and form several micrometer-size particles on the intercalation exfoliated graphene with a very small oxygen content (Fig. 4.5e). As for the thermal exfoliated-reduced graphene with a moderate oxygen content, the sulfur particles show a size of several tens to several hundreds of nanometers (Fig. 4.5f). Figure 4.6a, b show the TEM images of the G–S hybrids, in which sulfur nanocrystals with a particle size in the range of 5–10 nm are uniformly distributed on

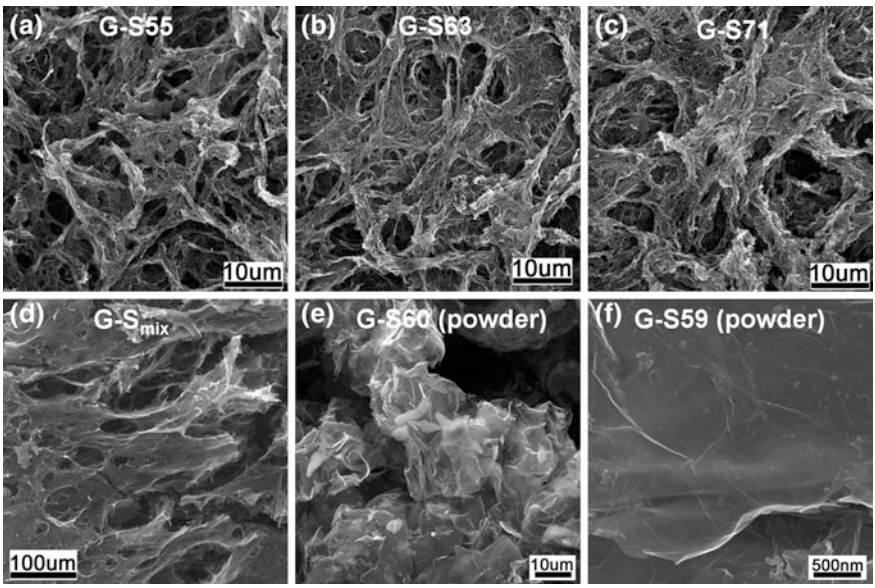


**Fig. 4.5** SEM images of **a** G–S55, **b** G–S63, and **c** G–S71 hybrids, **d** G–$S_{mix}$, **e** G–S60 hybrid (powder), and **f** G–S59 hybrid (powder)

the surface of graphene. The high-resolution TEM (HRTEM) image in Fig. 4.6b shows the edge of a graphene sheet with a tightly anchored sulfur nanocrystal. The adjacent fringe spacing of the aligned lattice fringes was about 0.34 nm, corresponding to the (026) plane of sulfur. Energy-dispersive X-ray spectroscopy (EDS) reveals the presence of C, O, and S in the G–S63 hybrid (Fig. 4.6c). It is worth noting that even after strong ultrasonication to disperse samples for TEM characterization, the sulfur nanocrystals are still anchored to the surface of the graphene with a high surface concentration, suggesting a strong interaction between graphene and sulfur. A STEM image (Fig. 4.6d) and corresponding carbon and sulfur maps (Fig. 4.6e, f) of the region indicated in Fig. 4.6d provide additional evidence to confirm the homogeneous distribution of sulfur on the surface of graphene. These results suggest that the presence of oxygen-containing functional groups plays an important role in anchoring and preventing the sulfur from growing into bulk crystalline particles [15, 16].

#### 4.2.7.3 Crystal Structure and Surface Functionality Analysis

X-ray diffraction (XRD) patterns of the G–S hybrids are shown in Fig. 4.7. The hybrids exhibit a broad diffraction peak at around 25°, confirming the reduction of GO with irregular layer stacking during the hydrothermal reaction. The sulfur

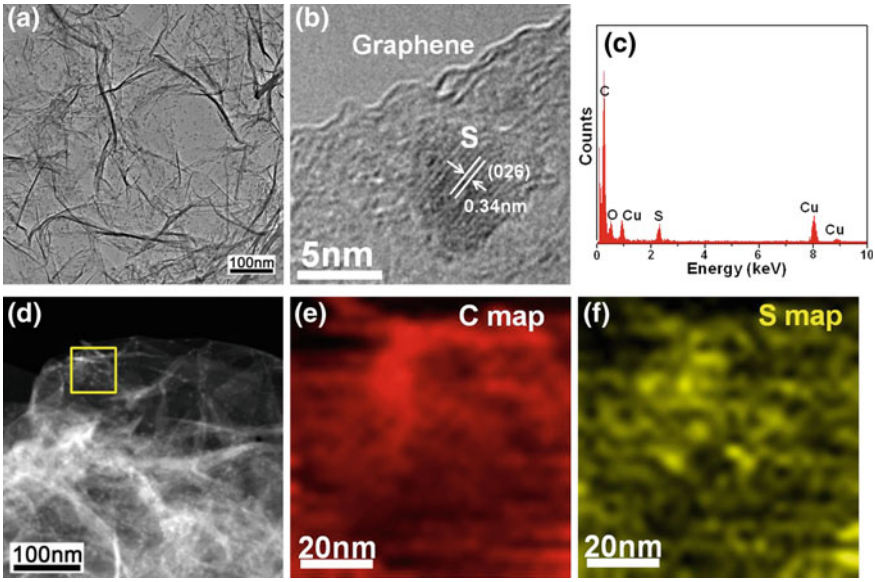


**Fig. 4.6** **a** TEM image, **b** HRTEM image, **c** EDS spectrum, **d** STEM image, **e** carbon mapping, and **f** sulfur mapping of the region indicated by the yellow square in **d**, of the G–S63 hybrid

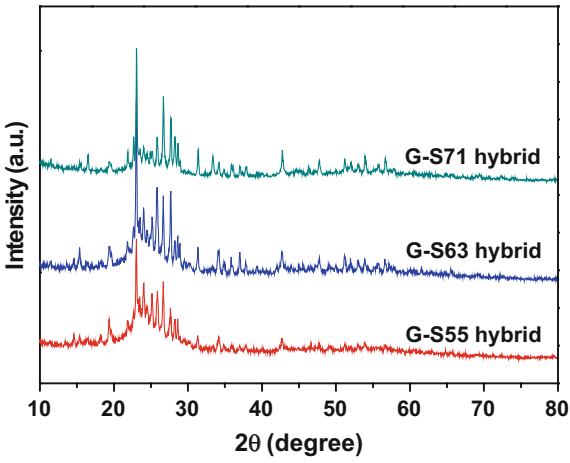


**Fig. 4.7** XRD patterns of the G–S55, G–S63, and G–S71 hybrids

shows sharp and strong peaks indicating a well-defined crystal structure, which is consistent with the TEM analysis.

To elucidate the extent of the binding between the graphene and sulfur nanocrystals, XPS measurements were performed. Gaussian fits to the C1s spectra of GO and the G–S63 hybrid both show four peaks, but in different ratios. The C1s signal of GO in Fig. 4.8a consists of component peaks at 284.6, 286.7, 288.0, and

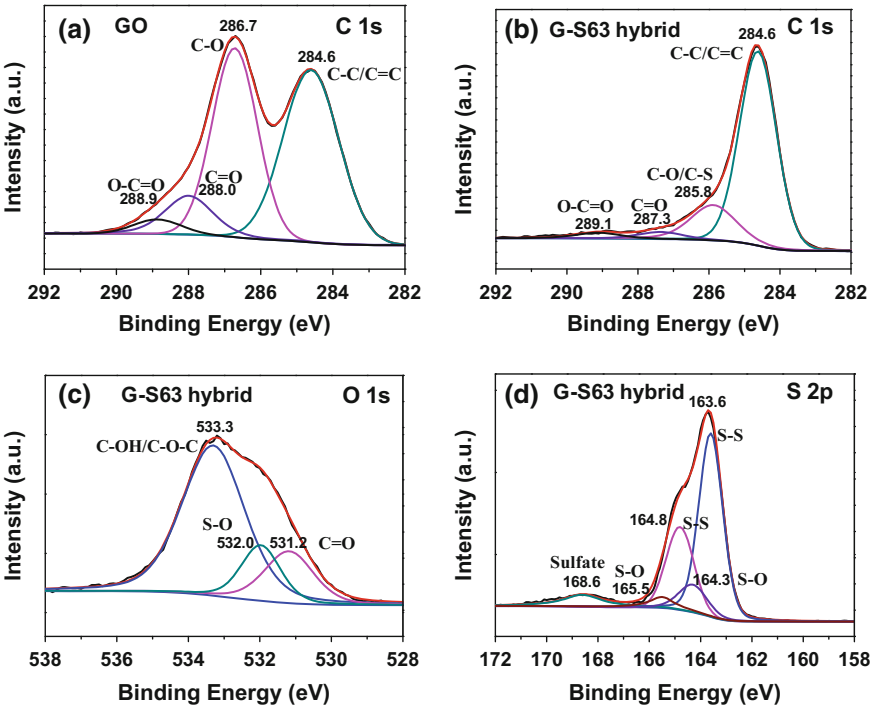


**Fig. 4.8** C 1s XPS spectra of the **a** GO and **b** G–S63 hybrid, **c** O 1s XPS spectrum of the G–S63 hybrid, and **d** S 2p XPS spectrum of the G–S63 hybrid

288.9 eV, corresponding to carbon species of C–C/C=C, C–O, C=O, and O–C=O, respectively [17]. After hydrothermal treatment, the hydroxyl and epoxide peaks were greatly reduced, as were those for the carbonyl and carboxyl groups to a lesser extent, while the peak corresponding to the $sp^2$ carbon increased and became narrower. This indicates that these oxygen-containing functional groups are removed and converted to C–O–S bonds during the reduction-assembly process (Fig. 4.8b). Meanwhile, the shifts in the binding energies of carbon bonded to oxygen (such as C–O and C=O) compared to GO suggest a different chemistry. The O1s spectrum of the G–S63 hybrid (Fig. 4.8c) can be deconvoluted into three peaks. The peak at 531.2 eV is assigned to C=O groups and the peak at 533.3 eV is ascribed to C–OH and/or C–O–C groups (hydroxyl and/or epoxide) [15, 18]. The peak centered at 532.0 eV is attributed to the formation of an S–O bond [19, 20]. The O/C ratios are 0.48 and 0.10 for the GO and G–S hybrids, which also implies the partial reduction of GO in the hybrids (Fig. 4.9). In the S 2p spectrum of the G–S63 hybrid (Fig. 4.8d), the S $2p_{3/2}$ (163.6 and 164.8 eV) and $2p_{1/2}$ (164.3 and 165.5 eV) spin-orbit levels with an energy separation of 1.2 eV are attributed to the S–S bond and S–O species, respectively [20, 21]. With the increase of sulfur loading, the proportion of S–S increases while S–O in S 2p is similar for G–S55,

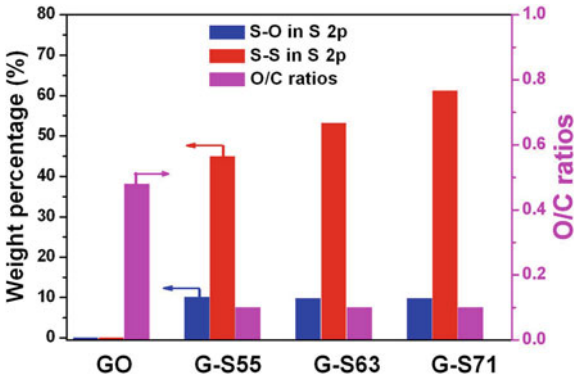


**Fig. 4.9** Relationship of the O/C ratio and weight percentage of S–O and S–S in S 2p in the GO, G–S55, G–S63, and G–S71

G–S63, and G–S71 hybrids (Fig. 4.9). The other small peak at 168.6 eV can be ascribed to the sulfate species formed by the oxidation of sulfur in air [22]. The above analysis indicates that the sulfur nanocrystals maintain intimate contact with graphene through S–O bonding, which could immobilize sulfur and the corresponding polysulfides produced during the discharge/charge process, preventing the loss of active materials and stabilizing the cyclic life of Li–S batteries.

## 4.3 Interaction Mechanism Between Oxygen-Containing Groups and Sulfur/Polysulfides

To better understand the possible functionality of oxygen-containing groups on the performance of Li–S batteries during cycling, especially for the polysulfides produced, we performed density functional theory (DFT) calculations to explore the interaction between oxygen-containing species and polysulfides. All calculations were performed with the plane wave-based VASP code [23, 24], applying projector augmented wave (PAW) [25] pseudopotentials to describe electron-ion interactions, and the local density approximation functional (LDA) [26] for the electronic exchange correlation effect. Kohn–Sham one-electron valence states were expanded on the basis of plane waves with a cutoff energy of 400 eV. A large polyaromatic hydrocarbon (PAH) molecule consisting of 54 C atoms and 18 H atoms was constructed to represent the graphene within a cubic supercell (20 Å × 20 Å × 20 Å). The graphene oxide with hydroxyl (epoxide) groups was modeled by adding two OH groups (four O atoms) on both sides of the PAH surface. The *k*-space sampling was restricted to the Γ-point for all calculations. All atomic positions were relaxed to a force convergence of $10^{-2}$ eV/Å, and a dipole correction [27] to the total energy was used to improve the energy convergence for charged systems. For an isolated $S_3^{1-}$ anion, the vertical detachment energy is calculated to be 2.47 eV, which is slightly less than the previously determined theoretical results (2.64 eV) and well reproduces the experimental value (2.50 eV) [28]. The charge population was calculated using Bader charge analysis [29].

Based on the above experimental results, the residual oxygen-containing functional groups on graphene are mainly hydroxyl and epoxide, which is in accordance with the recent theoretical prediction [30]. Here, we focused on $S_3$ clusters and multiply charged $S_3$ anions (mono-anion, $S_3^{1-}$ and di-anion, $S_3^{2-}$) with a chain-like structure, since other multiply charged S anions ($S_n^{\sigma-}$, $n$ = 4–8, σ = 1, 2) take chain-like structures based on DFT studies [28, 31] and should behave similarly to $S_3$ anions on a graphene surface. Smaller sulfur molecules ($S_{2–4}$) were also reported with good electrochemical performance in Li–S batteries recently [32]. Figure 4.10a presents the fully relaxed geometric structures of the neutral $S_3$ clusters and polyanions ($S_3^{1-}$ and $S_3^{2-}$). The calculated S–S bond length and bond angle of $S_3^{1-}$ are almost the same as those of $S_3^{2-}$, and are respectively longer and smaller than those for a neutral $S_3$ cluster. The longer S–S bond length and reduced bond angle of $S_3^{1-}$ and $S_3^{2-}$ are the result of a charge redistribution as shown in Fig. 4.10a. For example, the two terminal sulfur atoms are negatively charged (−0.14 e) while the center sulfur atom is positively charged (+0.28 e) for a neutral $S_3$ cluster, however, in the case of $S_3^{1-}$ ($S_3^{2-}$), two terminal sulfur atoms are more negatively charged, −0.5 e (−1.0 e), while the center sulfur atom remains in a neutral state. In order to compare the interaction between a charged $S_3$ cluster ($S_3^{1-}$ and $S_3^{2-}$) and graphene with that between a neutral $S_3$ cluster and graphene, we define the binding energy ($E_b$) as follows:

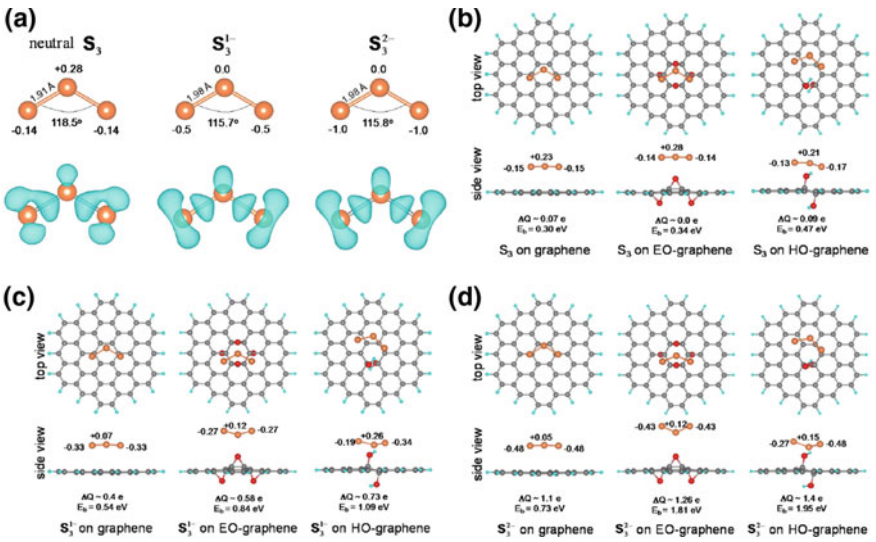


**Fig. 4.10** **a** Geometric structures of a fully relaxed neutral $S_3$ and charged $S_3^{1-}$ ($S_3^{2-}$) clusters, and corresponding charge density plots with a charge isocontour of 0.002 e/Å$^3$ (lower panel), side and top view of **b** a neutral $S_3$ cluster, **c** $S_3^{1-}$ and **d** $S_3^{2-}$ on graphene, EO-graphene, and HO-graphene surfaces

$$E_b = E\left(S_3^{\sigma} @ \text{Graphene}\right) - E(\text{Graphene}) - E\left(S_3^{\sigma}\right) \quad \sigma = 0, -1, \text{and} -2$$

Here, $E(\text{Graphene}), E\left(S_3^{\sigma}\right)$ and $E\left(S_3^{\sigma} @ \text{Graphene}\right)$ are total energies of graphene, an isolated $S_3$ cluster and graphene bound to a $S_3$ cluster, respectively. Using the above definition, we observe a moderate binding effect (0.30 eV) between a neutral $S_3$ cluster and the pristine graphene surface, which slightly increases to 0.34 (0.47) eV after introducing epoxide (hydroxyl) groups on the graphene surface, EO-graphene (HO-graphene), as described in Fig. 4.10b. This implies that epoxide and hydroxyl groups remaining on the graphene surface do not greatly improve the binding between graphene and a neutral $S_3$ cluster. However, as shown in Fig. 4.10c and d, hydroxyl and epoxide groups can remarkably increase the binding between graphene and the charged $S_3$ clusters ($S_3^{1-}$ and $S_3^{2-}$). For example, the binding energy of $S_3^{1-}$ ($S_3^{2-}$) on the HO-graphene is calculated to be 1.09 (1.95) eV, which is about 2–3 times larger than that of $S_3^{1-}$ ($S_3^{2-}$) on the pristine graphene surface. Charge population analysis indicates that oxygen-containing functional groups on the graphene surface can induce a larger charge transfer ($\Delta Q$) from the polysulfide ($S_3^{1-}$ and $S_3^{2-}$) anions to graphene. For instance, the calculated $\Delta Q$ from $S_3^{1-}$ ($S_3^{2-}$) to HO-graphene increases from 0.4 (1.1) to 0.73 (1.4) electrons, as shown in Fig. 4.10c and d. Therefore, the increased binding effect can be ascribed to the larger $\Delta Q$ between $S_3^{1-}$ ($S_3^{2-}$) and graphene due to the existence of epoxide or hydroxyl groups on the graphene surface. It was also found that the HO-graphene shows stronger binding effects on the polysulfide ($S_3^{1-}$ and $S_3^{2-}$) anions than does the EO-graphene, and the binding energies are calculated to be 1.09 (1.95) eV and 0.84 (1.81) eV for $S_3^{1-}$($S_3^{2-}$) on the HO-graphene and EO-graphene, respectively. This mainly results from the fact that hydroxyl groups on the graphene surface can induce an asymmetrical charge distribution on the two end sulfur atoms of a $S_3$ cluster, resulting in larger polarization and consequently stronger electrostatic interaction between a $S_3$ cluster and the HO-graphene. Here, taking $S_3^{2-}$ on the HO-graphene as an example, a larger partial charge (0.48 electrons) for the end sulfur atom closer to the hydroxyl group than that (0.27 electrons) for the sulfur atom at the other end is observed, as shown in Fig. 4.10d.

## 4.4 Properties of Sulfur Nanocrystal/Graphene Composites

### *4.4.1 Electrical Property and Mechanical Flexibility*

The sulfur nanocrystal/graphene composites have high electrical conductivity (Fig. 4.11a) and good mechanical flexibility, which can be directly used as a binder-free, flexible cathode that requires no metal current-collector (Fig. 4.11b). The electrical conductivity of G–S55, G–S63, and G–S71 can reach 730, 660, and

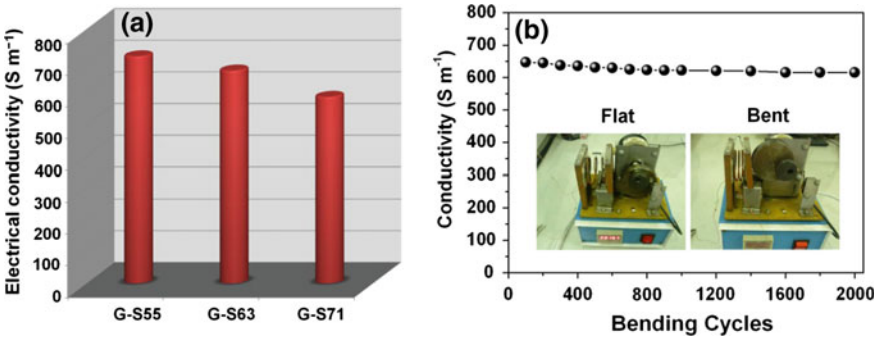


**Fig. 4.11** **a** Electrical conductivity of the G–S55, G–S63, and G–S71 hybrids. **b** Stability of the G–S63 membrane in terms of electrical conduction over 2000 cycles

600 S $m^{-1}$ respectively (Fig. 4.11a). Even after bending 2000 times with a bending radius of 1.5 mm, the G–S63 shows a high electrical conductivity of 628 S $m^{-1}$ (Fig. 4.11b), indicating an excellent flexibility and long-term durability of the conductive electrode.

### *4.4.2 Electrochemical Performance*

In order to demonstrate the structural benefits of G–S hybrids and the bonding between graphene and sulfur nanocrystals for improving cathode performance, a series of electrochemical measurements were carried out. The G–S hybrids were cut into slices, compressed and shaped into circular pellets, and then directly used as electrodes. Cyclic voltammetry (CV) was used to reveal the electrochemical reaction mechanism of the G–S cathode measured between 1.5 and 2.8 V at a sweep rate of 0.1 mV $s^{-1}$, as shown in Fig. 4.12a. During the first cathodic reduction process, two peaks at approximately 2.3 and 2.0 V (vs. $Li^+/Li^0$) were observed. The peak at 2.3 V corresponds to the reduction of sulfur to higher order polysulfides ($Li_2S_x$, $4 < x < 8$) [33]. The peaks at 2.0 V is related to the reduction of higher order polysulfides to lower order polysulfides (such as $Li_2S_4$, $Li_2S_3$) and $Li_2S$ [34, 35]. In the subsequent anodic scan, one asymmetric oxidation peak (which can be divided into two peaks) is observed at about 2.5 V, and is attributed to the conversion of lithium sulfides to polysulfides and sulfur. These results are in agreement with galvanostatic charge-discharge curves (Fig. 4.12b). From the second cycle, both the CV peak positions and areas remain almost unchanged, suggesting relatively good capacity retention.

The rate capability of the G–S cathodes is shown in Fig. 4.13a, measured using a coin cell configuration with a lithium metal anode. The G–S63 cathode can deliver a capacity of 1160 mAh $g^{-1}$ at 0.3 A $g^{-1}$ and the overall capacity of the cathode

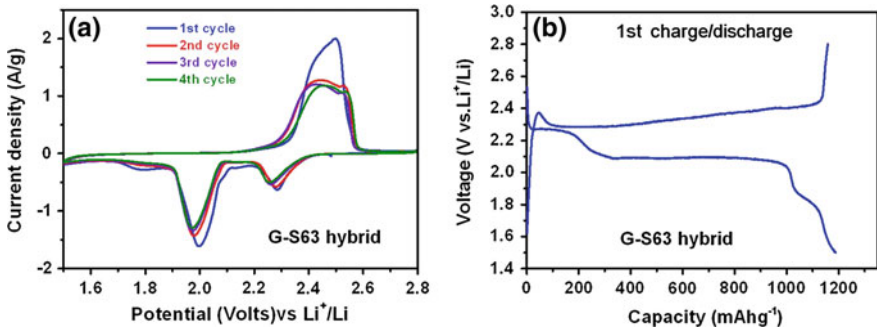


**Fig. 4.12** **a** CVs of the G–S63 cathode at 0.1 mV $s^{-1}$ in a potential window from 1.5 to 2.8 V. **b** First galvanostatic charge-discharge curve of the G–S63 cathode at 0.3 A $g^{-1}$

(including sulfur and graphene) is 731 mAh $g^{-1}$ calculated using the known sulfur weight ratio. The capacity of the G–S63 hybrid can be maintained at ~700 mAh $g^{-1}$ after 50 cycles, much higher than those of the G–S59 hybrid (powder) with ~410 mAh $g^{-1}$ and G–S60 hybrid (powder) with ~350 mAh $g^{-1}$ after 50 cycles (Fig. 4.13b). The sulfur content can be easily tuned by the initial sulfur addition, and the properties of G–S55 and G–S71 cathodes were compared in Fig. 4.13a. With the increase of the current density to 1.5 and 4.5 A $g^{-1}$, the specific capacity of the G–S63 cathode is 670 and 390 mAh $g^{-1}$ with the overall capacity of 422 and 246 mAh $g^{-1}$, demonstrating a high-rate performance. Moreover, the material recovered most of the original capacity when the cycling current was restored to 0.75 A $g^{-1}$, implying that the structure of the sulfur electrode remains stable even under high-rate cycling. The high-rate performance of the G–S cathodes is attributed to the thin graphene and nanosized sulfur which lead to short $Li^+$ diffusion distances, while the open porous structure provides rapid ion transport pathways. The immobilization of sulfur/(poly)sulfides by oxygen-containing groups during cycling is vitally important for the stable utilization of sulfur in the cathodes based on first-principles calculations, which is also verified by the existing S–O species in the S 2p region after discharged to the end of the second plateau (Fig. 4.14). As demonstrated in Fig. 4.13c, the sulfur cathode can maintain a capacity as high as 541 mAh $g^{-1}$ at 0.75 A $g^{-1}$ for the G–S63 over 100 cycles even after the rate capability test, much better than those of G–S hybrids (powder) as shown in Fig. 4.13d. Furthermore, its Coulombic efficiency is around 98% for all the G–S cathodes during cycling (Fig. 4.13c). It should be noted that the entrapment of sulfur by the large surface areas and many functional groups of the graphene ensures a complete redox process, prevents sulfur from dissolving into the electrolyte and results in improved cycling performance.

To reveal the structural stability of the G–S cathode, the discharged and recharged G–S63 electrodes were disassembled in the glovebox, washed using a dimethyl carbonate solution, sonicated and transferred to the vacuum chamber of the TEM for structure characterization. The STEM and TEM images after discharging are shown in Fig. 4.15a, b. The morphology and structure of the G–S

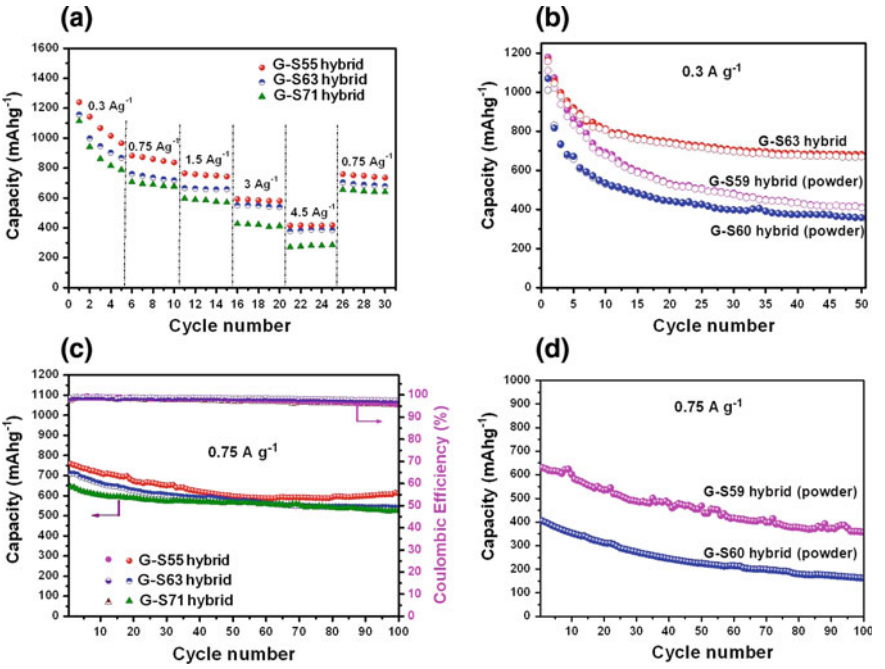


**Fig. 4.13** **a** Capacity of the G–S55, G–S63, and G–S71 cathodes at different current densities. **b** Cycling stability of the G–S63 hybrid, G–S59 hybrid (powder) and G–S60 hybrid (powder) cathodes at 300 mA $g^{-1}$ for 50 cycles. **c** Cyclic performance and Coulombic efficiency of the G–S55, G–S63, and G–S71 cathodes at 0.75 A $g^{-1}$ for 100 cycles. **d** Cyclic performance of the G–S59 hybrid (powder) and G–S60 hybrid (powder) cathodes at 0.75 A $g^{-1}$ for 100 cycles

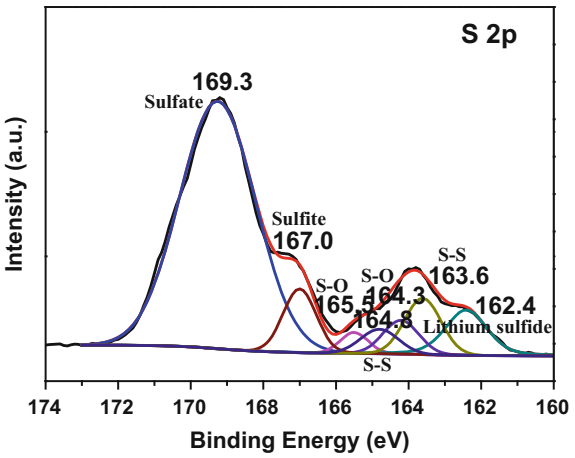


**Fig. 4.14** S 2p XPS spectra of the G–S63 hybrid electrode after discharged to the end of the second plateau

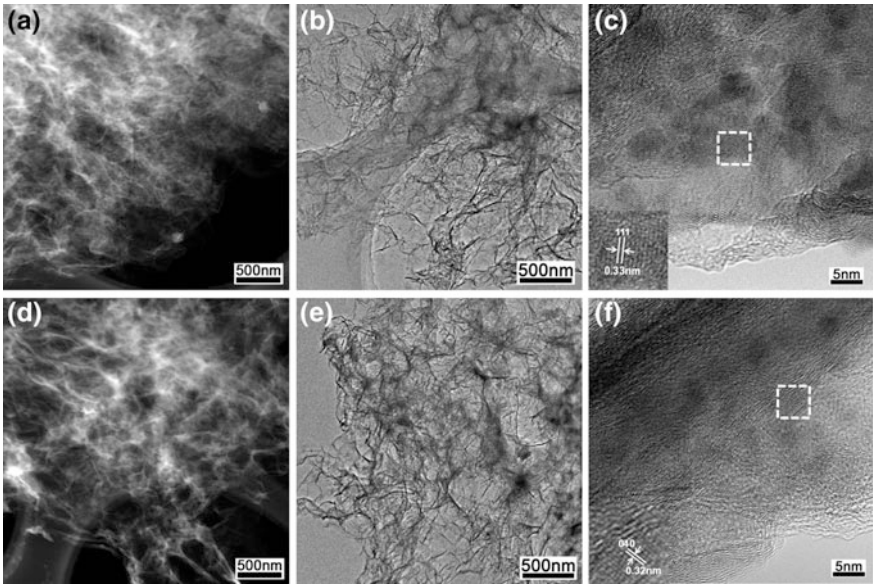


**Fig. 4.15** **a** STEM, **b** TEM and **c** HRTEM images of the G–S63 electrode after discharging to 1.5 V. **d** STEM, **e** TEM, and **f** HRTEM images of the G–S63 electrode recharged to 2.8 V (Insets are two enlarged nanocrystals marked in **c** and **f**)

cathode materials were well preserved and there are many nanocrystals uniformly dispersed on the surface of crumpled graphene, similar to the fresh sample (Fig. 4.6a, d). From the HRTEM image of the sample (Fig. 4.15c), the size of the nanocrystals was still between 5 and 10 nm. The stripe-width of the nanocrystals was 0.33 nm (inset of Fig. 4.15c, enlarged image marked in white square) and 0.28 nm (Fig. 4.16), which correspond to the interplanar spacing of the $Li_2S$ (111) and (200) planes (cubic, Fm-3 m, $a = b = c = 5.72$ Å). After being recharged

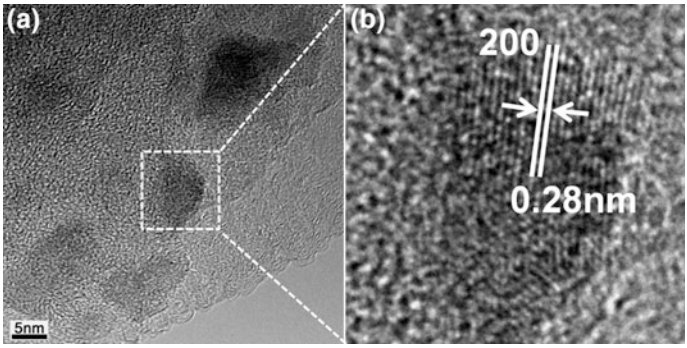


**Fig. 4.16** **a** HRTEM image and **b** an enlarged nanocrystal marked in **a** of the G–S63 electrode after discharged to 1.5 V

to 2.8 V, the nanocrystals have the same size as the discharge product (Fig. 4.15d, e), and the HRTEM image reveals the adjacent fringe spacing of 0.32 nm related to the (040) plane of S (orthorhombic, Fddd, $a$ = 10.45, $b$ = 12.84, and $c$ = 24.46 Å, inset of Fig. 4.15f). These observations imply the excellent structural stability of the electrode, which can be ascribed to the highly conductive interwoven fibrous graphene and hydroxyl/epoxide groups that can support and immobilize the S/polysulfides enabling the reversible discharge/charge reactions.

## 4.5 Conclusion

In this chapter, we have designed and prepared fibrous G–S hybrids by a one-pot reduction-assembly method, which is simple, highly efficient, and scalable. The combination of the highly conductive interwoven fibrous graphene and the small size of the sulfur (5–10 nm) greatly improves the kinetics of charge and ion transfer in these G–S hybrid electrodes. Therefore, the G–S hybrid cathodes demonstrate excellent electrochemical performance with high specific capacity, good rate performance, and stable cyclability. The main conclusions are as follows:

(1) Different sulfur contents of 55, 63 and 71 wt% in G–S hybrid are obtained through controlling the sulfur amount added into the precursors.
(2) The surface oxygen-containing functional groups of graphene promote the distribution of sulfur nanocrystals and tight contact of the sulfur with graphene.
(3) The G–S hybrid can be cut and pressed into plates for using as Li–S battery electrodes without metal current-collector, binder, and conductive additive, and demonstrate excellent flexibility even after bending 2000 times.
(4) The fibrous graphene facilitates electron transfer, the porous network of interconnected graphene allows rapid ion transport, and the sulfur nanocrystals provide short $Li^+$ diffusion distances.
(5) The strong absorption and interaction of oxygen-containing functional groups on graphene with sulfur/polysulfides effectively reduce the dissolution of polysulfide intermediates into the electrolyte and improve the cycling performance.
(6) DFT calculations reveal that the performance improvement results from the strong binding between the oxygen-containing functional groups on the graphene and sulfur/polysulfides, which reduces the irreversible loss of sulfur during discharge/charge.

## References

1. Manthiram A, Fu Y, Su Y-S (2012) Challenges and prospects of lithium-sulfur batteries. Acc Chem Res 46(5):1125–1134
2. Yang Y, Zheng G, Cui Y (2013) Nanostructured sulfur cathodes. Chem Soc Rev 42(7):3018–3032

3. Zheng GY, Yang Y, Cha JJ, Hong SS, Cui Y (2011) Hollow carbon nanofiber-encapsulated sulfur cathodes for high specific capacity rechargeable lithium batteries. Nano Lett 11 (10):4462–4467
4. Segal M (2009) Selling graphene by the ton. Nat Nanotech 4(10):611–613
5. Yang XW, Zhu JW, Qiu L, Li D (2011) Bioinspired effective prevention of restacking in multilayered graphene films: towards the next generation of high-performance supercapacitors. Adv Mater 23(25):2833–2838
6. Li C, Shi GQ (2012) Three-dimensional graphene architectures. Nanoscale 4(18):5549–5563
7. Qiu L, Liu JZ, Chang SLY, Wu Y, Li D (2012) Biomimetic superelastic graphene-based cellular monoliths. Nat Commun 3:1241
8. Choi BG, Yang M, Hong WH, Choi JW, Huh YS (2012) 3D macroporous graphene frameworks for supercapacitors with high energy and power densities. ACS Nano 6(5):4020–4028
9. Chen WF, Li SR, Chen CH, Yan LF (2011) Self-assembly and embedding of nanoparticles by in situ reduced graphene for preparation of a 3D graphene/nanoparticle aerogel. Adv Mater 23 (47):5679–5683
10. Xu YX, Sheng KX, Li C, Shi GQ (2010) Self-assembled graphene hydrogel via a one-step hydrothermal process. ACS Nano 4(7):4324–4330
11. Mukherjee R, Thomas AV, Krishnamurthy A, Koratkar N (2012) Photothermally reduced graphene as high-power anodes for lithium-ion batteries. ACS Nano 6(9):7867–7878
12. Zhao J, Pei S, Ren W, Gao L, Cheng H-M (2010) Efficient preparation of large-area graphene oxide sheets for transparent conductive films. ACS Nano 4(9):5245–5252
13. Zhou GM et al (2014) A graphene–pure-sulfur sandwich structure for ultrafast, long-life lithium-sulfur batteries. Adv Mater 26(4):625–631
14. Wu ZS et al (2009) Synthesis of high-quality graphene with a pre-determined number of layers. Carbon 47(2):493–499
15. Zhou GM et al (2012) Oxygen bridges between NiO nanosheets and graphene for improvement of lithium storage. ACS Nano 6(4):3214–3223
16. Wu ZS et al (2010) Anchoring hydrous $RuO_2$ on graphene sheets for high-performance electrochemical capacitors. Adv Funct Mater 20(20):3595–3602
17. Stankovich S et al (2007) Synthesis of graphene-based nanosheets via chemical reduction of exfoliated graphite oxide. Carbon 45(7):1558–1565
18. Lv W et al (2009) Low-temperature exfoliated graphenes: vacuum-promoted exfoliation and electrochemical energy storage. ACS Nano 3(11):3730–3736
19. Zhang GX, Sun SH, Yang DQ, Dodelet JP, Sacher E (2008) The surface analytical characterization of carbon fibers functionalized by $H_2SO_4/HNO_3$ treatment. Carbon 46 (2):196–205
20. Zhang L et al (2012) Electronic structure and chemical bonding of a graphene oxide-sulfur nanocomposite for use in superior performance lithium-sulfur cells. Phys Chem Chem Phys 14(39):13670–13675
21. Demir-Cakan R et al (2011) Cathode composites for Li-S batteries via the use of oxygenated porous architectures. J Am Chem Soc 133(40):16154–16160
22. Schaufuß AG et al (1998) Incipient oxidation of fractured pyrite surfaces in air. J Electron Spectrosc Relat Phenom 96(1–3):69–82
23. Kresse G, Furthmuller J (1996) Efficient iterative schemes for ab initio total-energy calculations using a plane-wave basis set. Phys Rev B 54(16):11169–11186
24. Kresse G, Furthmuller J (1996) Efficiency of ab-initio total energy calculations for metals and semiconductors using a plane-wave basis set. Comput Mater Sci 6(1):15–50
25. Blochl PE (1994) Projector augmented-wave method. Phys Rev B 50(24):17953–17979
26. Perdew JP, Zunger A (1981) Self-interaction correction to density-functional approximations for many-electron systems. Phys Rev B 23(10):5048–5079
27. Makov G, Payne MC (1995) Periodic boundary-conditions in ab-initio calculations. Phys Rev B 51(7):4014–4022

28. Hunsicker S, Jones RO, Gantefor G (1995) Rings and chains in sulfur cluster anions S- to $S-_9(-)$—theory (simulated annealing) and experiment (photoelectron detachment). J Chem Phys 102(15):5917–5936
29. Henkelman G, Arnaldsson A, Jonsson H (2006) A fast and robust algorithm for Bader decomposition of charge density. Comput Mater Sci 36(3):354–360
30. Bagri A et al (2010) Structural evolution during the reduction of chemically derived graphene oxide. Nat Chem 2(7):581–587
31. Berghof V, Sommerfeld T, Cederbaum LS (1998) Sulfur cluster dianions. J Phys Chem A 102 (26):5100–5105
32. Xin S et al (2012) Smaller sulfur molecules promise better lithium-sulfur batteries. J Am Chem Soc 134(45):18510–18513
33. Xiao LF et al (2012) A soft approach to encapsulate sulfur: polyaniline nanotubes for lithium-sulfur batteries with long cycle life. Adv Mater 24(9):1176–1181
34. Ji LW et al (2011) Graphene oxide as a sulfur immobilizer in high performance lithium/sulfur cells. J Am Chem Soc 133(46):18522–18525
35. Zhou GM et al (2012) A flexible nanostructured sulphur-carbon nanotube cathode with high rate performance for Li–S batteries. Energy Environ Sci 5(10):8901–8906

# Chapter 5
# Graphene–Pure Sulfur Sandwich Structure for Ultrafast, Long-Life Lithium-Sulfur Batteries

## 5.1 Research Background

As discussed in the previous chapters, physical confinement and chemical binding have been proposed for preventing the diffusion of polysulfides, improving the utilisation of sulfur, enhancing rate capability and cycling life of Li–S batteries. Great efforts have also been made to alleviate the shuttle effect by changing the properties of the electrolytes. For example, researchers have attempted to replace organic liquid electrolytes with ionic-liquid-based electrolytes, polymer electrolytes or "solvent-in-salt" electrolytes, which inhibit the mobility of polysulfide anions [1–5]. However, the change in electrolyte usually results in a degradation of the kinetic properties of the battery, which is caused by the lowering of ion mobility in the electrolyte. Besides, a nonporous aluminium (Al) foil current collector is usually used in Li–S batteries. This component accounts for approximately 5–9% of the weight of the battery and reduces its gravimetric energy density [6–8]. In addition, the Al foil suffers oxidation and corrosion at the high operating voltages of the sulfur cathode, which can cause sulfur to lose electrical contact with the current collector and increase the internal resistance of the battery [9]. Therefore, the metallic current collector is another important component that affects the performance of a Li–S battery.

Other than focusing on cathode pore structure design and electrolyte optimization, novel battery configuration in Li–S system is another strategy to address the above challenges where less attention has been placed on. In general, a battery configuration mainly consists of two parts: a cathode and an anode, with a polymer separator. In the conventional Li–S battery configuration, sulfur is easily dissolved into the electrolyte forming lithium polysulfides, which are shuttling between cathode and anode, covering on the cathode and anode surface. If S/lithium



G. Zhou, *Design, Fabrication and Electrochemical Performance of Nanostructured Carbon Based Materials for High-Energy Lithium–Sulfur Batteries*, Springer Theses,
DOI 10.1007/978-981-10-3406-0_5

polysulfides can be localised in the cathode side and be efficiently reused during cycling, the cyclic stability and rate capability of the Li–S battery will be improved.

With these considerations, we designed a unique sandwich structure with pure sulfur between two graphene membranes. One graphene membrane was used as a current collector (GCC) with sulfur coated on it as the active material, and the other graphene membrane was coated on a commercial polymer separator (G-separator) (denoted GCC/S+G-separator, Fig. 5.1a, IV). The design of the G-separator enables good flexibility and strength of the barrier layer, which thus avoids the peeling-off of the membrane and reassembly in the battery that is seen in other studies [10–12]. The flexible and conductive graphene layers on both sides of the sulfur electrode provide excellent electric conductivity, and the sandwich structure can accommodate the large volumetric expansion of sulfur during lithiation. Both these effects can be enhanced during cycling when part of the sulfur migrates inside the graphene membranes, which causes the GCC and G-separator to also act as sulfur reservoirs in addition to current collectors. Therefore, compared to the conventional Li–S battery configuration (Fig. 5.1b), the shuttle effect can be significantly reduced by

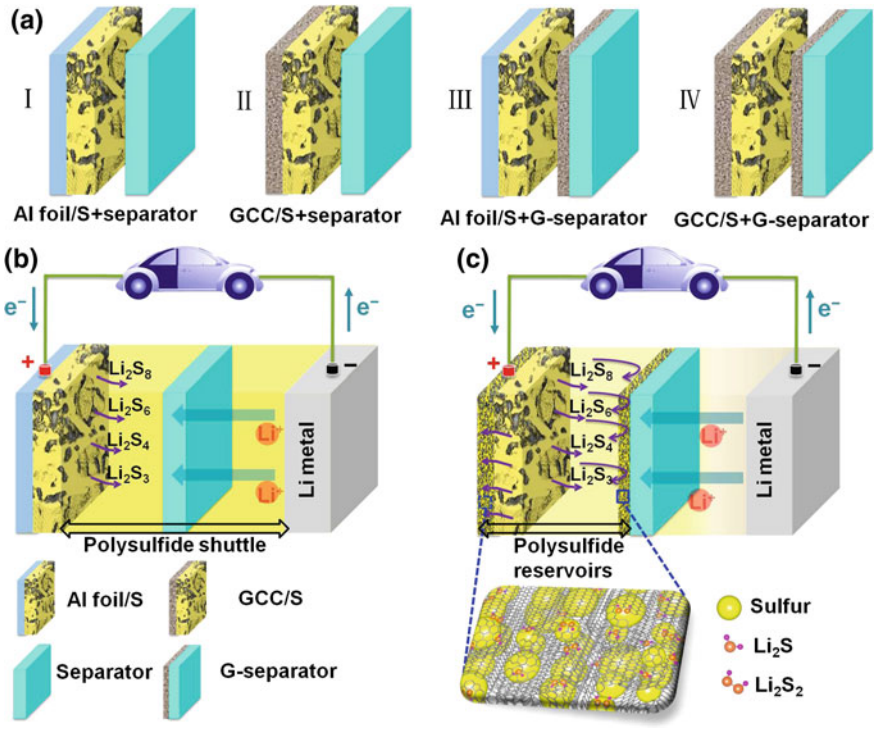


**Fig. 5.1** **a** Schematic of electrode configurations of (*I*) Al foil/S+separator, (*II*) GCC/S + separator, (*III*) Al foil/S+G-separator, and (*IV*) GCC/S+G-separator. **b** Schematic of a Li–S battery with electrode configuration (*I*). **c** Schematic of a Li–S battery with electrode configuration (IV)

this design (Fig. 5.1c). The presence of the graphene layer on the separator surface acts as a good barrier to mitigate the shuttle effect of dissolved polysulfides, which is caused by the moderate binding of the graphene sheets with sulfur and polysulfides through charge transfer [13]. Furthermore, the surface roughness of the GCC can improve the adhesion of sulfur to it and lower the charge-transfer impedance and polarisation of the Li–S battery. These properties provide the newly designed Li–S batteries with long cycling life and excellent rate performance. This design avoids any surface modification of sulfur particles and simplifies the fabrication of sulfur cathodes. Because the density of a GCC is only one quarter of that of an Al foil current collector, the use of GCC can further improve the specific energy density when assembled into a battery. For comparison, the commonly used Al foil with a commercial separator (Al foil/S+separator), GCC/S with a commercial separator (GCC/S+separator) and the commonly used Al foil with a G-separator (Al foil/S+G-separator) configuration were examined (Fig. 5.1a, I–III).

## 5.2 Construction of Sandwich Cathode Structure

### *5.2.1 GCC Fabrication*

The graphene powder used was fabricated by Sichuan Jinlu Group, China, using the patent invented by Pei et al. (Chinese patent No. CN201110282370.5). A GCC was fabricated by a vacuum filtration and peeling-off process. Typically, the graphene powder was dispersed in alcohol to form a suspension with a concentration of 0.2 mg $mL^{-1}$. The suspension was subsequently vacuum filtered using a Nylon membrane with a pore size of 0.44 μm. After fully drying at 90 °C for 30 min, the graphene membrane could be easily peeled from the filter surface and used as a GCC.

### *5.2.2 Fabrication of Sulfur-Coated GCC Electrodes*

For the fabrication of sulfur electrodes, a sulfur slurry (70 wt% sulfur as active material, 20 wt% commercial carbon black (Ketjen black EC-300J) as conductive agent and 10 wt% PVDF as binder) was coated onto a GCC. After drying at 60 °C for 12 h under vacuum oven, the GCC/S electrode is obtained.

### *5.2.3 G-Separator Fabrication*

G-separator was fabricated using the same process as that used for a GCC but with the filter membrane replaced by a polypropylene (PP) membrane, which is a typical

commercial separator widely used in LIBs, and without the need to be peeled from the filter membrane. The graphene-coated PP membrane was used as a G-separator.

Based on these basic processes, large-area GCC and G-separator sheets were fabricated using a homemade continuous vacuum filtration device, which may enable the industrial fabrication of such GCC and G-separators.

## 5.3 Structure Characterization of the Sandwich Cathode Structure

### *5.3.1 Structure Characterization of the Graphene Powder*

It should be noted that the graphene used in this research is produced through an intercalation-exfoliation method from graphite and is commercially available at a low cost (Fig. 5.2a). The as-produced graphene sheets are transparent with sheet size around 2–5 μm (Fig. 5.2b, c), and the thickness indicates the graphene sheets are mainly distributed between 5 and 10 layers (Fig. 5.2d). It has an almost perfect crystal structure with negligible oxidation (Fig. 5.2e, f). As a consequence, the graphene membrane obtained is chemically inert and has a high electrical conductivity. These features give our design and materials strong potential for the industrial production and application of Li–S batteries.

### *5.3.2 Structure Feature of the GCC*

The typical photograph of the as-prepared large-area GCC is shown in Fig. 5.3a. It exhibits robust mechanical stability and is flexible so that it can be bent into arbitrary shapes (Fig. 5.3b). Figure 5.3c shows SEM micrographs of the GCC, showing a rough surface that consists of numerous overlapping and interconnected graphene sheets with a size up to 10 μm. The average roughness (0.98 μm) of the GCC is approximately three times that of an Al foil current collector (0.34 μm), as measured by a surface profiler and shown in Fig. 5.4. The greater roughness can improve the adhesion between the active material and the current collector and reduce the internal impendence and polarisation of a battery [14]. The surface structure and porosity of GCC were measured and reconstructed by three-dimensional (3D) X-ray microtomography (XRM), as shown in Fig. 5.3d, which confirms the rough surface and high porosity of the GCC (marked in blue). The pore structure characteristics and Brunauer–Emmett–Teller (BET) specific surface area of the GCC were investigated by nitrogen ($N_2$) isothermal adsorption (Fig. 5.5). Nitrogen adsorption–desorption isotherms of the GCC were identified as type IV with a typical mesopore hysteresis loop because the graphene sheets are organised to produce an open pore system that contains macropores and mesopores [15, 16]. The GCC exhibited a specific surface

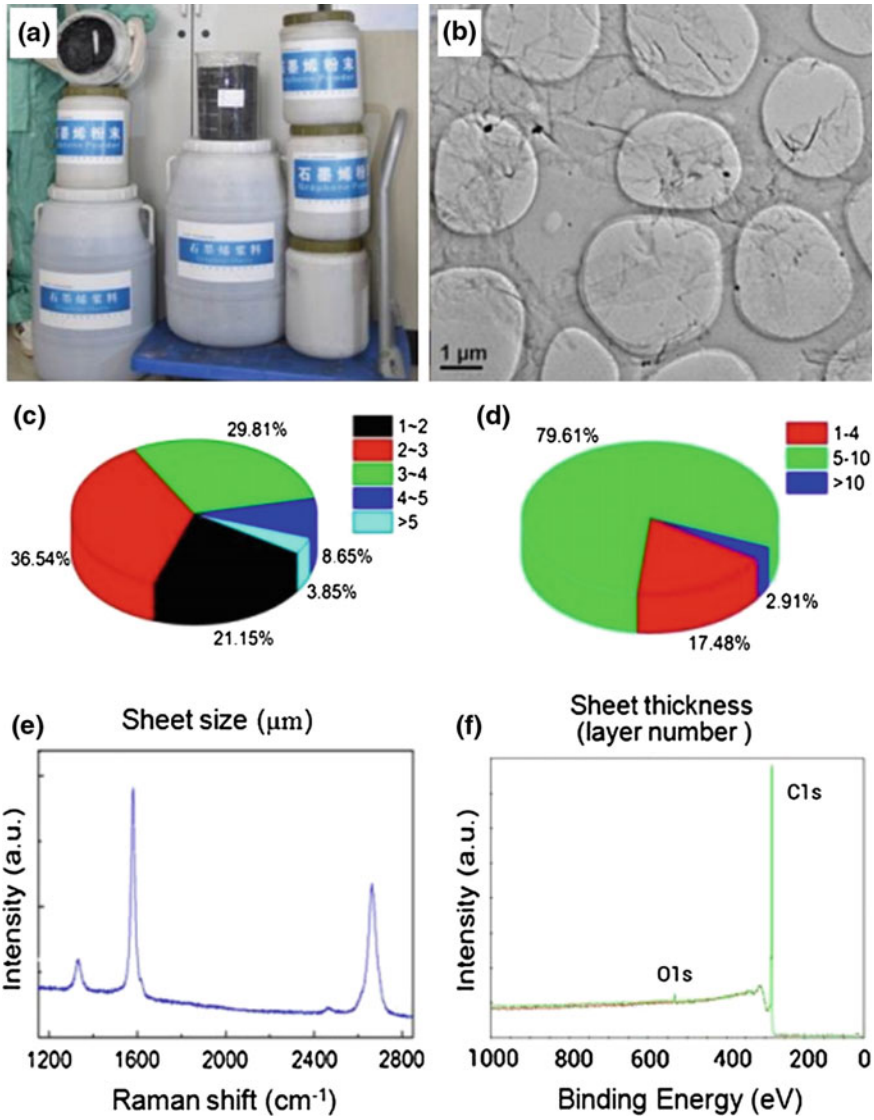


**Fig. 5.2** **a** Photograph of graphene slurry and powder as industrial products. **b** TEM image of the graphene. **c** Sheet lateral size and **d** thickness distribution of the graphene. **e** Raman and **f** XPS spectra of the graphene

area of 27.4 $m^2$ $g^{-1}$. This porous structure and exposed specific surface area are beneficial for the adsorption of sulfur and polysulfides on graphene sheets and for providing tunnels for fast ion transport. The GCC with a 20-μm thickness (Fig. 5.3e) exhibited an excellent electrical conductivity of 830 S $cm^{-1}$, which is substantially greater than that reported for a reduced graphene oxide film (<300 S $cm^{-1}$) [17, 18].

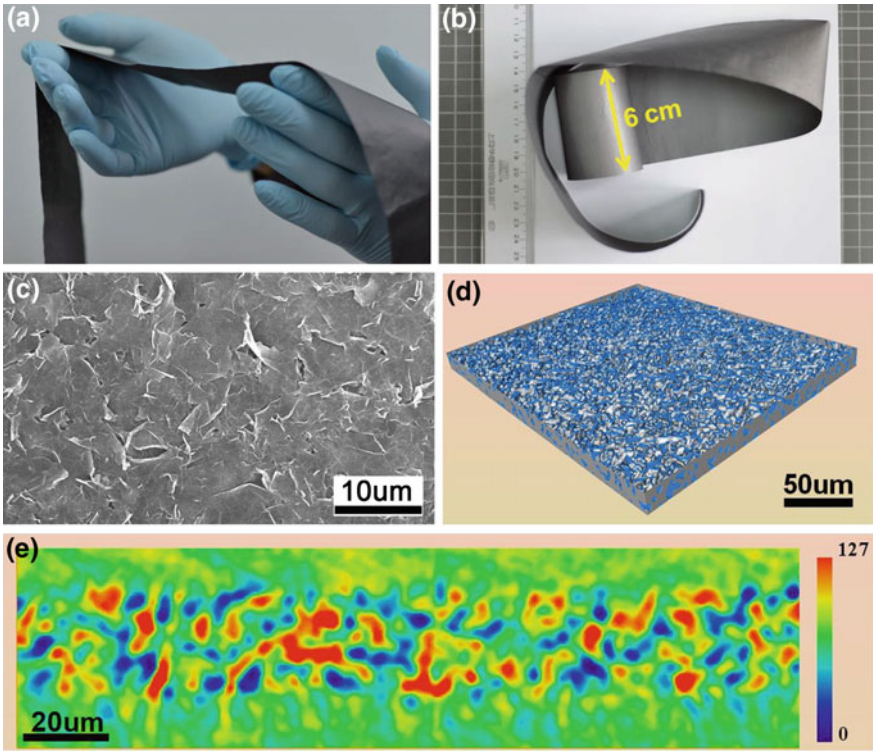


**Fig. 5.3** **a**, **b** Photographs of an as-prepared large-area GCC strip (width: 6 cm). **c** SEM image of the surface of a GCC. **d** 3D image of the reconstructed GCC, including graphene and pores marked in *blue*. **e** Cross section of a slice from the tomographic sequence of the GCC

The thickness of the GCC was close to that of a typical Al foil current collector (20–25 μm, 5.6 mg $cm^{-2}$); however, its light weight (1.3 mg $cm^{-2}$) contributes to the improved energy density of the battery.

### *5.3.3 Structure Characterization of the GCC/S Cathode*

To fabricate the GCC/S electrode, we coated a sulfur slurry [70 wt% sulfur, 20 wt% carbon black and 10 wt% polyvinylidene fluoride (PVDF)] onto a GCC. The slurry formed a compact and homogeneous layer of sulfur on the GCC (Fig. 5.6a, b), and the elemental C, O, S and F (from PVDF) distributions were investigated using energy-dispersive X-ray analysis (EDS, inset of Fig. 5.6b). The EDS elemental mapping confirms the uniform distribution of C and S on the GCC (Fig. 5.6c, d).

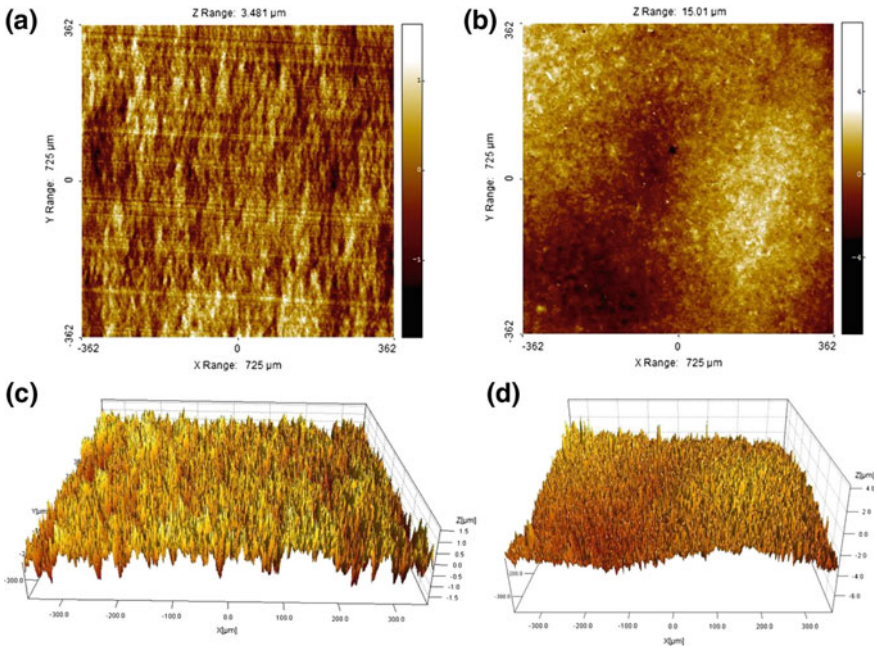


**Fig. 5.4** Surface roughness comparison of **a**, **c** an Al foil current collector and **b**, **d** a GCC with two dimensional and three-dimensional surface morphology

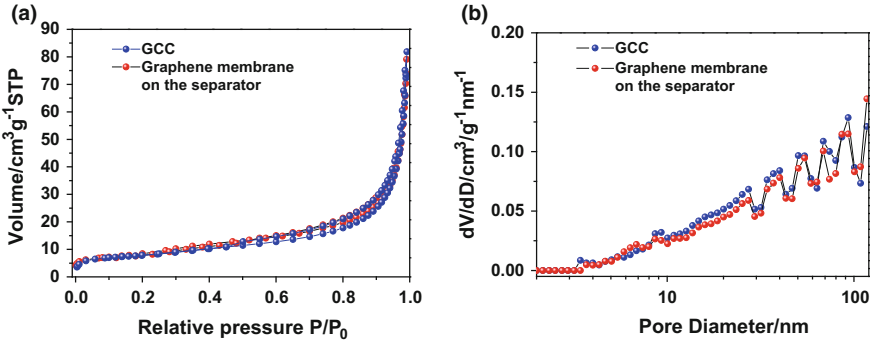


**Fig. 5.5** **a** Nitrogen adsorption–desorption isotherms of the GCC and graphene membrane coated on the separator. **b** Pore-size distributions of the GCC and graphene membrane coated on the separator determined by the DFT method

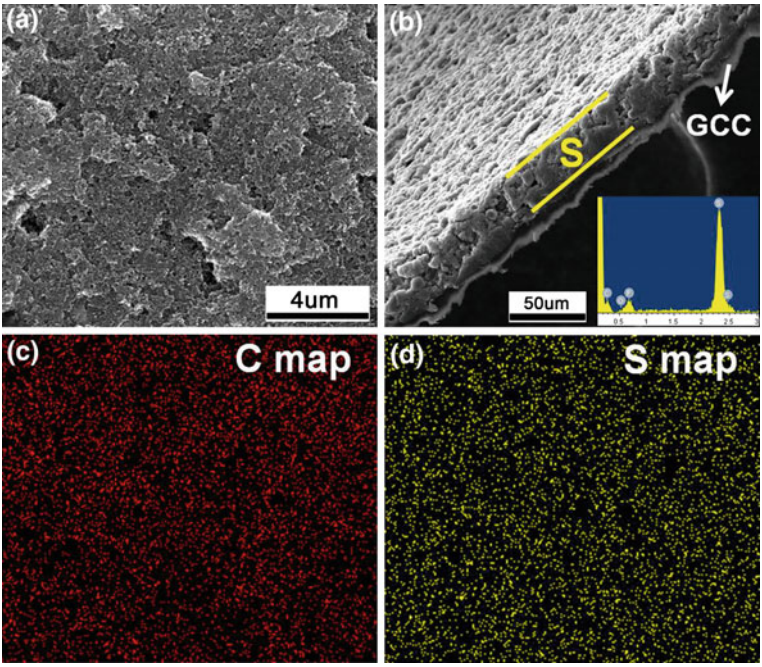


**Fig. 5.6** SEM images of the **a** surface and **b** cross section of a sulfur electrode and the corresponding EDS spectrum (unit: keV). **c**, **d** C and S elemental maps of the area shown in (**a**)

### *5.3.4 Structure Characterization of the G-Separator*

Figure 5.7a shows a photograph of a large-area G-separator prepared by continuous vacuum filtration using a graphene slurry directly coated onto a commercial polymer separator. The graphene membrane coated on the separator has a similar pore structure to GCC (Fig. 5.5). The G-separator can be cut and shaped into any size required for batteries with different shapes (Fig. 5.7b). Because of the excellent flexibility and mechanical strength of the polymer separator, the G-separator can be rolled, twisted and bent into curved forms without irreversible deformation (Fig. 5.7c, d). The cross-sectional XRM image of the G-separator in Fig. 5.7e shows that the graphene membrane with a thickness of approximately 10 μm closely adheres to the polymer separator. Figure 5.7f displays the 3D reconstructed G-separator, in which the graphene membrane serves as an embedded current collector to lower the internal resistance of the electrode and as a barrier to entrap/reutilise the dissolved polysulfide intermediates.

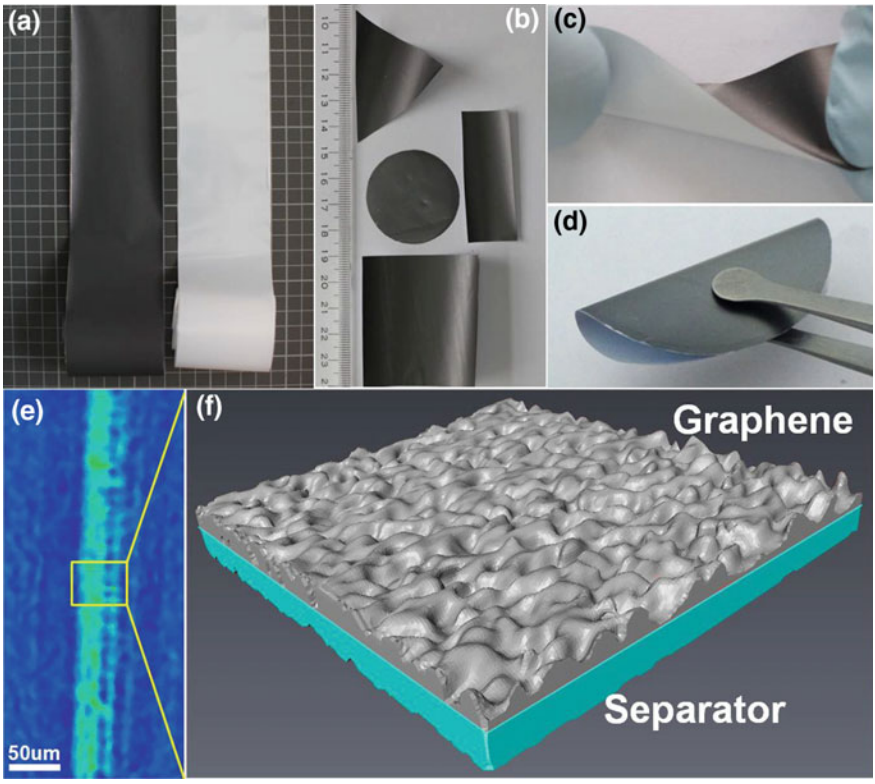


**Fig. 5.7** **a** Photograph of a large-area G-separator (*left*) and a commercial polymer separator (*right*). Photographs showing **b** the processibility and **c**, **d** the flexibility of a G-separator. **e** Cross-sectional XRM image of a G-separator, and **f** a 3D reconstructed G-separator

## 5.4 Electrochemical Performance of the Sandwich Cathode Structure

To demonstrate the effectiveness of this unique sandwich configuration in improving the performance of Li–S batteries, a series of electrochemical measurements were performed with the four different previously described configurations (Fig. 5.1). Electrochemical impedance spectroscopy (EIS) measurements of the four configurations before cycling and after five cycles are shown in Fig. 5.8. The Nyquist plots for these electrodes consist of a single depressed semicircle in the high-to-medium frequency region and an inclined line at low frequency (Fig. 5.8a), which can be ascribed to the charge-transfer resistance $R_{ct}$ and a mass-transfer process [19, 20]. The value of $R_{ct}$ for the GCC/S+G-separator (52.6 Ω) is much lower than those of the Al foil/S+separator (1100.5 Ω), GCC/S+separator (283.8 Ω) and Al foil/S+G-separator (62.8 Ω), which means that the GCC/S +G-separator electrode exhibits faster charge-transfer compared to that of the other

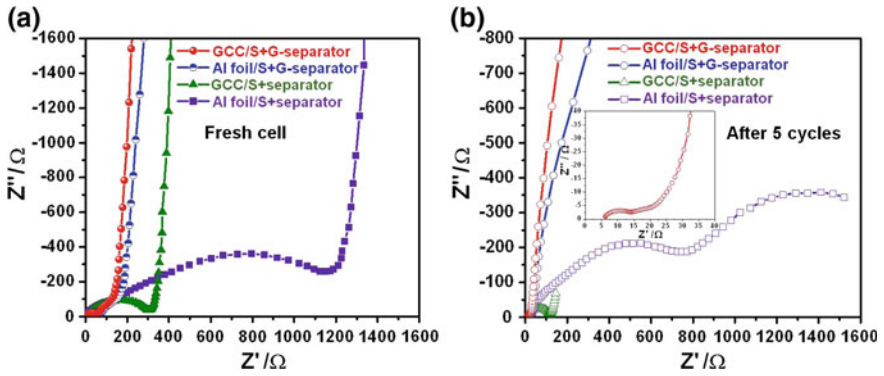


**Fig. 5.8** Nyquist plots of the electrodes with different configurations recorded **a** before cycling and **b** after five cycles from 10 kHz to 10 MHz at room temperature

electrodes. The G-separator functions as an embedded current collector, which significantly reduces the internal resistance of the electrode. The surface roughness of GCC, which can increase the contact surface area and adhesion between sulfur and the current collector, leads to a decrease in the contact resistance, thus further lowering the charge-transfer impedance. EIS spectra recorded after five cycles exhibited two semicircles for the Al foil/S+separator (Fig. 5.8b), which corresponds to a passivation film in the high-frequency region and $R_{ct}$ in the medium-to-low frequency region. These results suggest dissolution of polysulfides followed by their deposition onto the electrodes [21]. In contrast, the appearance of only one semicircle for the GCC/S+separator, GCC/S+G-separator and Al foil/S +G-separator with decreased $R_{ct}$ indicates good electrolyte infiltration and charge transport as well as effective entrapment/reutilisation of dissolved sulfur and polysulfide intermediates between the graphene sheets in the GCC and G-separator.

The galvanostatic charge/discharge behaviour of a Li–S battery was evaluated at different current densities (from 0.3 to 6 A $g^{-1}$) within a potential window of 1.5–2.8 V verus $Li^+/Li^0$. The discharge/charge profiles of a battery with a GCC and a G-separator consist of two plateaus (Fig. 5.9a) even at a very high current rate, which corresponds to the reduction of elemental sulfur ($S_8$) to long-chain lithium polysulfides at 2.3–2.4 V and to the formation of short-chain $Li_2S_2/Li_2S$ at 2.1 V [22, 23]. The two plateaus in the charge curve represent the backward reaction from lithium sulphides to polysulfides and finally to sulfur. The plateaus are flat and stable with a relatively low polarisation of 162 mV at 0.3 A $g^{-1}$, which suggests a kinetically efficient reaction process with a small barrier [22, 24]. In contrast, the discharge potential decreases and the charge potential increases with higher voltage hysteresis (287, 209 and 194 mV at 0.3 A $g^{-1}$) for the Al foil/S+separator, GCC/S +separator and Al foil/S+G-separator (Fig. 5.9b–d). The charge/discharge plateaus obviously shift or even disappear in the case of the Al foil/S+separator at high current rates, which indicates high polarisation and slow redox reaction kinetics with inferior reversibility (Fig. 5.10).

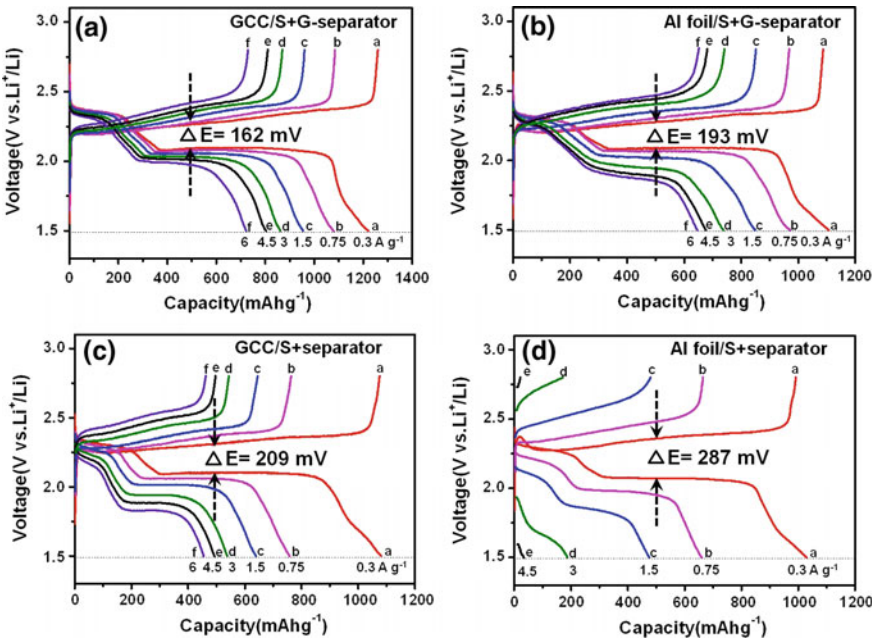


**Fig. 5.9** Galvanostatic charge-discharge profiles of the sulfur electrodes with **a** a GCC/S +G-separator, **b** an Al foil/S+G-separator, **c** a GCC/S+separator, and **d** an Al foil/S+separator at different current densities

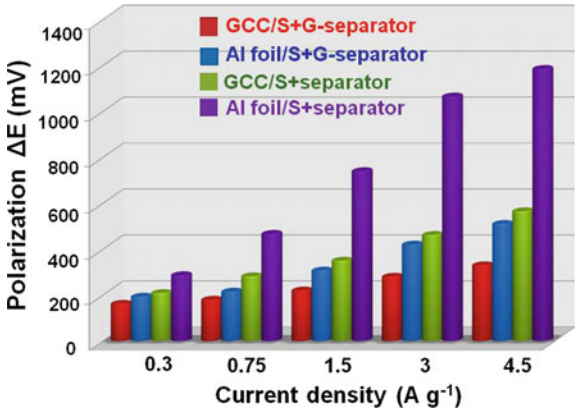


**Fig. 5.10** Comparison of the potential difference between the charge and discharge of four configurations plateaus at different current densities

The cyclic voltammetry (CV) curves of the battery with a GCC/S+G-separator were obtained over a voltage range from 1.5 to 2.8 V at a scan rate of 0.1 mV $s^{-1}$. They show two cathodic peaks and two anodic peaks (Fig. 5.11a), and the peak intensities/positions and integral areas are almost identical from the second to the fifth cycle; these results demonstrate the good cycling stability of this system.

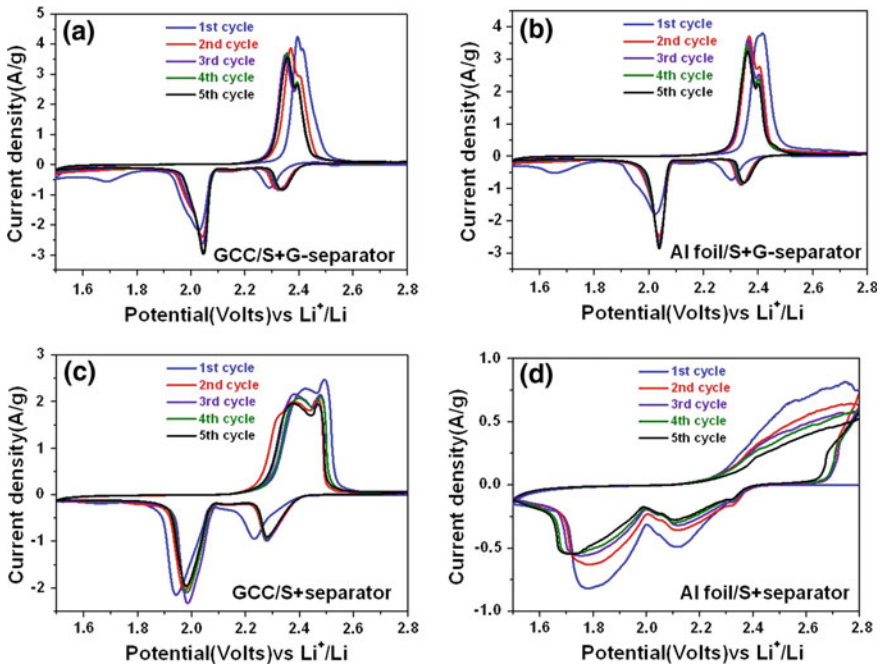


**Fig. 5.11** CVs of the sulfur electrodes with **a** a GCC/S+G-separator, **b** an Al foil/S+G-separator, **c** a GCC/S+separator, and **d** an Al foil/S+separator at a scan rate of 0.1 mV $s^{-1}$ for five cycles

The CV curves from the GCC/S+separator and Al foil/S+G-separator show a slightly lower reduction potential and a slightly higher oxidation potential (Fig. 5.11b, c), and the peaks deform and widen dramatically with significantly decreased integral areas for the cell with an Al foil/S+separator, which suggests a sluggish kinetic process (Fig. 5.11d). The superior properties of the GCC/S +G-separator can be ascribed to the good GCC/sulfur/G-separator/electrolyte contact with excellent electrical conductivity, which promotes the reaction kinetics of the cathode. These results are consistent with the galvanostatic charge–discharge measurements.

When the discharge current density was increased to 1.5 and 6 A $g^{-1}$, the battery with a GCC/S+G-separator still delivered capacities as high as 1000 and 750 mAh $g^{-1}$, which indicates an ultrafast charge/discharge capability; these capacities are 2 and 50 times higher, respectively, than those of the battery with a Al foil/S+separator tested under the same conditions (Fig. 5.12a). If the weights of the Al foil and GCC are taken into account, the advantage of using a GCC is more evident. The GCC/S+G-separator exhibits a much higher specific capacity than those configurations with Al foil. When the current density was changed back to 0.75 A $g^{-1}$, the battery with a GCC/S+G-separator resumed its capacity of 1052 mAh $g^{-1}$ and maintained a capacity of 950 mAh $g^{-1}$ with a Coulombic efficiency greater than 97% over 100 cycles, even after the rate capability test.

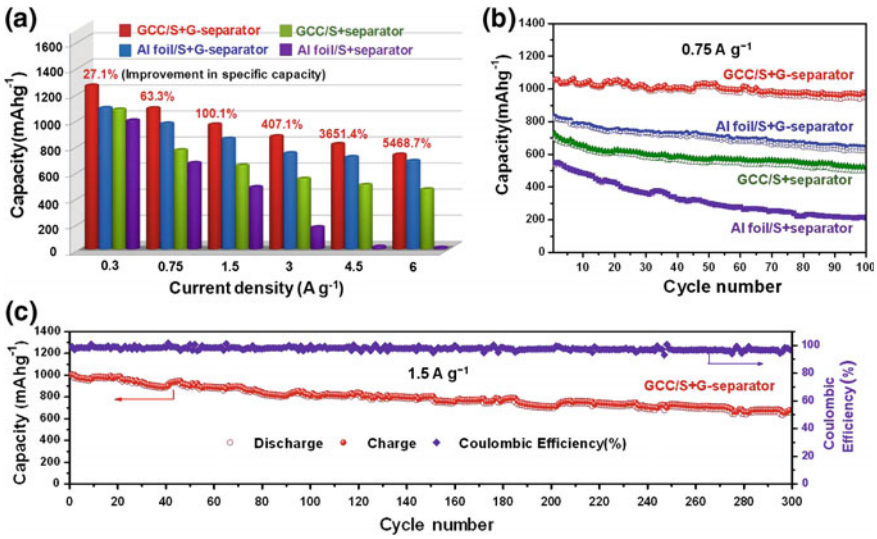


**Fig. 5.12** **a** Rate performance of the Li–S batteries with different configurations at different current densities. **b** Cycling stability of the Li–S batteries with different configurations at 0.75 A $g^{-1}$ for 100 cycles after the high current density test, **c** cycling stability of the Li–S batteries with GCC/S+G-separator at 1.5 A $g^{-1}$ for 300 cycles

These results demonstrate that batteries with a GCC/S+G-separator exhibit better capacity retention upon cycling compared to the other configurations (Fig. 5.12b). The long-term cycling stability of the Li–S battery with the GCC/S+G-separator was tested at a current density of 1.5 A $g^{-1}$ for 300 cycles. The sulfur electrode exhibited good cyclic performance and retained a capacity of 679 mAh $g^{-1}$ with a Coulombic efficiency above 97% during cycling, and the capacity decay was only 0.1% per cycle (Fig. 5.12c). The high performance delivered by the battery with the GCC/S+G-separator is ascribed to the two graphene membranes, which effectively reduce the internal resistance of the sulfur cathode and facilitate fast transport of electrons and lithium ions during the redox of sulfur. This fast transport is responsible for the excellent rate behaviour of the electrode.

The GCC and G-separator also store and reuse the dissolved lithium polysulfides to a large degree and accommodate the large volume change involved in the conversion reaction between sulfur and $Li_2S$. The analysis can also be confirmed by the decreased pore volume and pore size distribution as shown in Fig. 5.13 and Table 5.1. The BET of GCC/S and G-separator before cycling are 21.3 and 16.7 $m^2$ $g^{-1}$, which reduced to 12.6 and 5.7 $m^2$ $g^{-1}$ after cycling. The GCC and G-separator thereby alleviate the negative impact of shuttling and improve the utilisation of sulfur, which extends the cycling life of Li–S batteries.

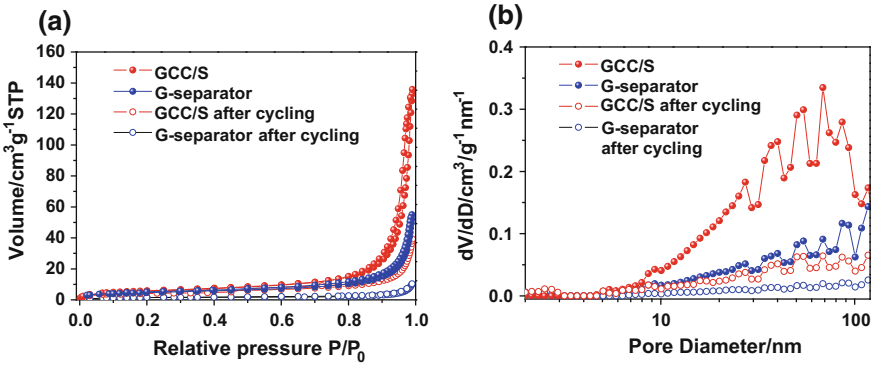


**Fig. 5.13** **a** Nitrogen adsorption–desorption isotherms of the GCC/S and G-separator before and after cycling. **b** Pore-size distributions of the GCC/S and G-separator before and after cycling determined by the DFT method

**Table 5.1** BET surface area and pore volume of the GCC/S electrode and G-separator before and after cycling

| Samples | BET surface area ($m^2$ $g^{-1}$) | Total pore volume ($cm^3$ $g^{-1}$) |
|---|---|---|
| GCC/S | 21.3 | 0.17 |
| GCC/S after cycling | 12.6 | 0.05 |
| G-separator | 16.7 | 0.08 |
| G-separator after cycling | 5.7 | 0.01 |

## 5.5 Interaction Between Graphene and Sulfur Species in Sandwich Cathode Structure

### *5.5.1 Function as a Current Collector*

To further understand the function of the electrode with two graphene membranes, we disassembled a battery after 50 cycles in a glovebox. The GCC/S electrode and the G-separator were removed, washed using a dimethyl carbonate solution and their structure characterised by SEM, TEM and XRM. Figure 5.14a shows a typical SEM image of the cycled GCC/S electrode, and the overall morphology and structure of the electrode are similar to those of the original sample. There is no obvious volume change for the GCC due to its robustness and the small interaction of the graphene sheets with the electrolyte, which cause the structural stability of the GCC during cycling. The EDS elemental maps (Fig. 5.14b) and spectra (Fig. 5.14c) show a uniform distribution of sulfur in the GCC, which suggests that the graphene membrane not only acts as a good current collector but also entraps the dissolved sulfur. These results were further confirmed by the 3D reconstructed

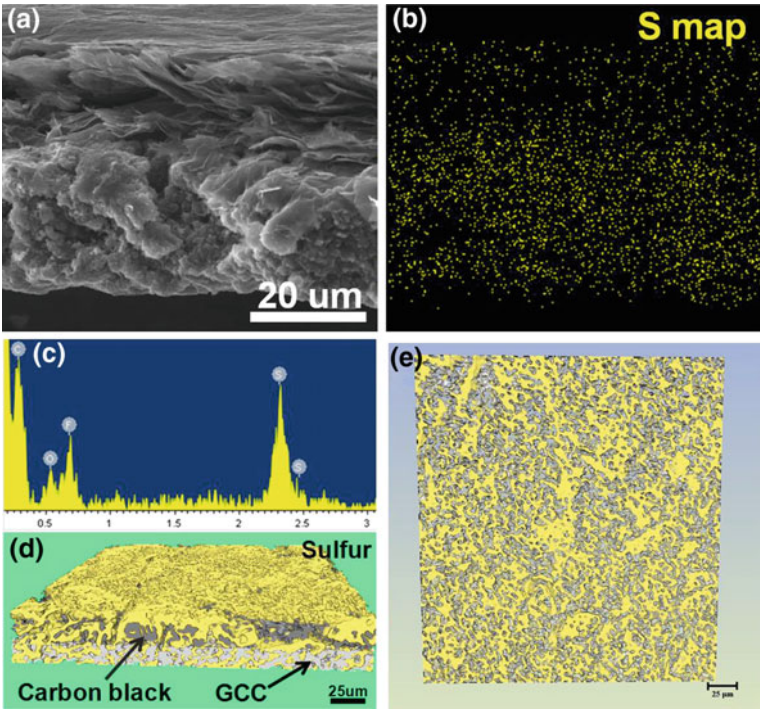


**Fig. 5.14** **a** SEM image and **b** corresponding elemental map of a GCC/S electrode. **c** EDS spectrum of the GCC (unit: keV), **d** 3D image of the reconstructed GCC/S electrode, and **e** cross-sectional XRM image of the GCC

sulfur electrode (Fig. 5.14d) and cross-sectional XRM images (Fig. 5.14e) of the GCC, in which sulfur is captured by graphene nanosheets in a homogeneous state.

### *5.5.2 Function as a Separator Coating Layer*

The G-separator provides effective contact between the sulfur and separator and functions as an embedded conductive network that enables fast electron and lithium-ion transport. The graphene membrane on the separator remains intact without cracks after cycling, which indicates its good structural stability (Fig. 5.15a). The high-magnification SEM image (Fig. 5.15b) and TEM/STEM images combined with EDS spectra (Fig. 5.15c, d) show that sulfur precipitates were anchored on the surface of graphene sheets, which suggests that they were immobilised. A 3D reconstruction of the G-separator (Fig. 5.15e) verifies that the layer-by-layer stacked structure of graphene acts as a strong absorbent to retain

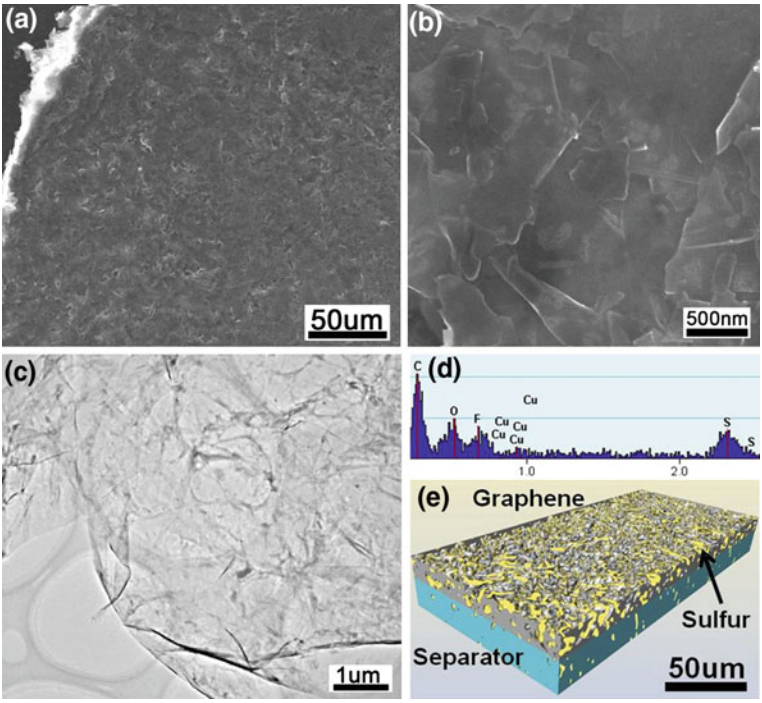


**Fig. 5.15** **a** Low-magnification and **b** high-magnification SEM images of graphene nanosheets on a G-separator. **c** TEM image of graphene from the G-separator and **d** corresponding EDS spectrum (unit: keV). **e** 3D image of the reconstructed G-separator

polysulfide species rather than allowing them to diffuse to the lithium anode, thereby triggering the polysulfide shuttling behaviour.

To reveal the morphology variations of the lithium anode after cycling, the batteries using Al foil/S+separator and GCC/S+G-separator configurations were disassembled, and the lithium plates were taken out and washed using dimethyl carbonate. Then the lithium plates were dried in a glove box, transferred using a sealed container into the vacuum chamber of the SEM for structure observation. A pure lithium plate before cycling was used as a comparison. It can be seen that the surface of metallic lithium before cycling is compact and smooth, as shown in Fig. 5.16a. However, using the Al foil/S+separator (Fig. 5.16b), serious corrosion damage occurred on the lithium surface after 100 cycles with a large number of cracks and the deposition of $Li_2S_2/Li_2S$. This is due to the side reaction between lithium polysulfides and metallic lithium during cycling. In contrast, a relatively smooth, less damaged surface was found on the lithium anode using the GCC/S +G-separator (Fig. 5.16c). These results demonstrate that the GCC and G-separator act as strong absorbents and barriers to alleviate the diffusion of polysulfides into the lithium anode during the charge/discharge process. Thus, the polysulfide shuttle phenomenon and lithium surface corrosion can be reduced.

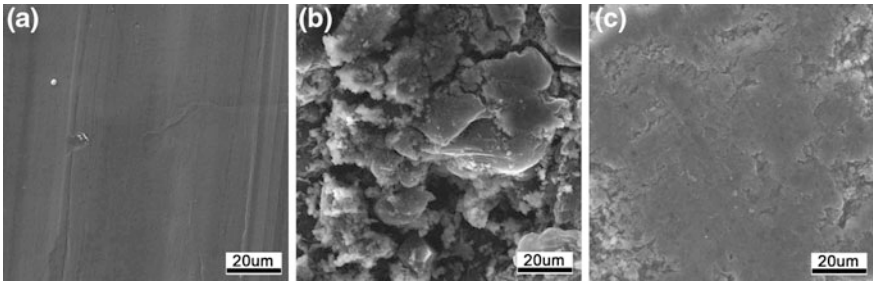


**Fig. 5.16** SEM images of the surface of a **a** pristine metallic lithium anode, **b** lithium anode using Al foil/S+separator after 100 cycles, and **c** lithium anode using GCC/S+G-separator after 100 cycles

From the previously discussed results, we estimated the amount of trapped sulfur in the graphene membranes of the GCC and G-separator by calculating the volume fraction of sulfur from the tomography data and analysing the cycling performance of the sulfur electrode. The battery with a GCC/S+G-separator delivered a high discharge capacity of 1345 mAh $g^{-1}$ and exhibited the best capacity retention of the four investigated configurations (Fig. 5.17a). Unlike the rapid initial decay observed in the cases of the Al foil/S+separator and the GCC/S+separator, the cell with a GCC/S+G-separator showed relatively stable performance and retained a capacity greater than 1000 mAh $g^{-1}$ over the first 50 cycles, with a Coulombic efficiency of approximately 98%. The capacity loss is ascribed to the inevitable polysulfide dissolution into the electrolyte. However, a capacity retention of only 34% was obtained for the electrode with an Al foil/S+separator, and the capacity decreased to less than 400 mAh $g^{-1}$ after 50 cycles, which indicates a high degree of polysulfide dissolution into the electrolyte. To quantitatively illustrate the improvement in electrochemical performance by the graphene membranes, we compared the capacities at the 50th cycles of sulfur electrodes with different configurations in combination with statistical sulfur distributions from tomographic data. The improved capacity $\Delta C_{IV-II}$ ($C_{(GCC/S+G\text{-}separator)} - C_{(GCC/S+separator)}$) from Fig. 5.17a is mainly ascribed to the graphene membrane barrier on the separator, and the ratio $\Delta C_{IV-II}/\Delta C_{(GCC/S+separator)}$ ($\Delta C_{(GCC/S+separator)}$ defines the decreased capacity of the electrode with a GCC/S+separator from the 1st to the 50th cycle, which is ascribed to the sulfur dissolution loss) is approximately 66%, lower than the calculated sulfur fraction in the graphene membrane (71%) of the G-separator determined from XRM, as shown in Fig. 5.17b, because the inevitable dissolution of sulfur into the electrolyte that was not calculated by XRM. The capacity difference $\Delta C_{II-I}$ from Fig. 5.17a between the GCC/S+separator and the Al foil/S +separator represents the contribution from GCC, where $\Delta C_{II-I}/C_{(GCC/S+separator)}$ is approximately 34% and approaches the statistical amount of sulfur (35%) in the GCC of the sulfur electrode determined from the XRM data (Fig. 5.17c).The agreement between the measured capacity difference and the statistical tomographic data related to the sulfur distribution indicates the roles of the graphene membranes

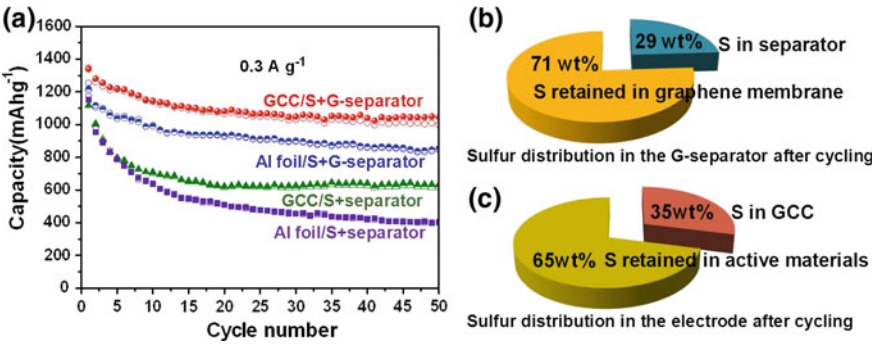


**Fig. 5.17** **a** Cycling performance of the Li–S batteries with different configurations at a current density of 0.3 A $g^{-1}$ for 50 cycles, statistical results from the XRM data of **b** sulfur distributed in the separator and retained in the graphene membrane, and **c** sulfur distributed in the GCC and retained as active material

in trapping and reusing the dissolved sulfur, improving material utilisation and improving Coulombic efficiency. All these results demonstrate the importance of the electrode configuration in improving the performance of Li–S batteries.

## 5.6 Conclusion

In this chapter, we have proposed a very simple but effective strategy for obtaining high-performance Li–S batteries through the use of a unique sulfur electrode that consists of a GCC and a G-separator. In comparison to an Al-foil current collector and commercial separator, the GCC and G-separator efficiently decrease the contact impedance of the current collector, the active material and the electrolyte. The electrode with two graphene membranes can provide rapid ion- and electron-transport paths, accommodate sulfur volumetric expansion and store and reuse migrating polysulfides to alleviate the shuttling effect. The light weight of the GCC can also contribute to a higher energy density of Li–S batteries. The main conclusions are as follows:

1. A unique sandwich structure was designed with pure sulfur between two graphene membranes. One graphene membrane is used as a current collector (GCC) to replace commercial Al foil with sulfur coated on it as the active material, and the other graphene membrane is coated on a commercial polymer separator (G-separator).
2. The flexible and conductive graphene layers on both sides of the sulfur electrode provide excellent electrical conductivity, and the sandwich structure can accommodate the large volumetric expansion of sulfur during lithiation.
3. The graphene layer on the separator surface acts as a good barrier to mitigate the shuttle effect of dissolved polysulfides. When the discharge current density was

increased to 6 A $g^{-1}$, the battery with a sandwich structure can still deliver capacities as high as 750 mAh $g^{-1}$, which indicates an ultrafast charge/discharge capability; and the capacity is 50 times higher than a conventional Li–S battery tested under the same conditions.

4. Sandwiched sulfur electrode exhibits good cyclic performance and retains a capacity of 679 mAh $g^{-1}$ with a Coulombic efficiency nearly 100% during cycling after 300 cycles at a current density of 1.5 A $g^{-1}$, so the capacity decay is only 0.1% per cycle.
5. For the first time, we used three-dimensional X-ray microtomography to explore sulfur diffusion during cycling.
6. It should be noted that the graphene used is produced through an intercalation-exfoliation method from graphite and is commercially available. The fabrication of large-area GCC and G-separators was also demonstrated, which indicates that this sulfur electrode design can be scaled for industrial manufacture.

## References


1. Marmorstein D et al (2000) Electrochemical performance of lithium/sulfur cells with three different polymer electrolytes. J Power Sources 89(2):219–226
2. Shin JH, Cairns EJ (2008) Characterization of N-methyl-N-butylpyrrolidinium Bis (trifluoromethanesulfonyl)imide-LiTFSI-Tetra(ethylene glycol) dimethyl ether mixtures as a Li metal cell electrolyte. J Electrochem Soc 155(5):A368–A373
3. Wang J et al (2008) Sulfur-mesoporous carbon composites in conjunction with a novel ionic liquid electrolyte for lithium rechargeable batteries. Carbon 46(2):229–235
4. Hassoun J, Scrosati B (2010) A high-performance polymer tin sulfur lithium ion battery. Angew Chem Int Ed 49(13):2371–2374
5. Suo L, Hu Y-S, Li H, Armand M, Chen L (2013) A new class of solvent-in-salt electrolyte for high-energy rechargeable metallic lithium batteries. Nat Commun 4:1481
6. Gaines L, Cuenca R [Argon National Laboratory: Argonne, IL] (2000) Technical report: costs of lithium–ion batteries for vehicles
7. Hu LB et al (2009) Highly conductive paper for energy-storage devices. Proc Natl Acad Sci USA 106(51):21490–21494
8. Zhou GM et al (2012) A nanosized $Fe_2O_3$ decorated single-walled carbon nanotube membrane as a high-performance flexible anode for lithium ion batteries. J Mater Chem 22 (34):17942–17946
9. Whitehead AH, Schreiber M (2005) Current collectors for positive electrodes of lithium-based batteries. J Electrochem Soc 152(11):A2105–A2113
10. Li XF et al (2012) Novel approach toward a binder-free and current collector-free anode configuration: highly flexible nanoporous carbon nanotube electrodes with strong mechanical strength harvesting improved lithium storage. J Mater Chem 22(36):18847–18853
11. Su YS, Manthiram A (2012) A new approach to improve cycle performance of rechargeable lithium–sulfur batteries by inserting a free-standing MWCNT interlayer. Chem Commun 48 (70):8817–8819
12. Wang X, Wang Z, Chen L (2013) Reduced graphene oxide film as a shuttle-inhibiting interlayer in a lithium–sulfur battery. J Power Sources 242:65–69

13. Zhou GM et al (2013) Fibrous hybrid of graphene and sulfur nanocrystals for high-performance lithium–sulfur batteries. ACS Nano 7(6):5367–5375
14. Wu H-C, Wu H-C, Lee E, Wu N-L (2010) High-temperature carbon-coated aluminum current collector for enhanced power performance of $LiFePO_4$ electrode of Li–ion batteries. Electrochem Commun 12(3):488–491
15. Zhou GM et al (2010) Graphene-wrapped $Fe_3O_4$ anode material with improved reversible capacity and cyclic stability for lithium ion batteries. Chem Mater 22(18):5306–5313
16. Lv W et al (2009) Low-temperature exfoliated graphenes: vacuum-promoted exfoliation and electrochemical energy storage. ACS Nano 3(11):3730–3736
17. Park S, Ruoff RS (2009) Chemical methods for the production of graphenes. Nat Nanotech 4 (4):217–224
18. Pei S, Cheng H-M (2012) The reduction of graphene oxide. Carbon 50(9):3210–3228
19. Zhou GM et al (2012) Oxygen bridges between NiO nanosheets and graphene for improvement of lithium storage. ACS Nano 6(4):3214–3223
20. Reddy MV et al (2007) α-$Fe_2O_3$ nanoflakes as an anode material for Li–ion batteries. Adv Funct Mater 17(15):2792–2799
21. Zu CX, Su YS, Fu YZ, Manthiram A (2013) Improved lithium–sulfur cells with a treated carbon paper interlayer. Phys Chem Chem Phys 15(7):2291–2297
22. Zhou GM et al (2012) A flexible nanostructured sulphur–carbon nanotube cathode with high rate performance for Li–S batteries. Energy Environ Sci 5(10):8901–8906
23. Elazari R, Salitra G, Garsuch A, Panchenko A, Aurbach D (2011) Sulfur-impregnated activated carbon fiber cloth as a binder-free cathode for rechargeable Li–S batteries. Adv Mater 23(47):5641–5644
24. Zheng GY, Yang Y, Cha JJ, Hong SS, Cui Y (2011) Hollow carbon nanofiber-encapsulated sulfur cathodes for high specific capacity rechargeable lithium batteries. Nano Lett 11 (10):4462–4467

# Chapter 6
# A Graphene Foam Electrode with High Sulfur Loading for Flexible and High-Energy Li–S Batteries

## 6.1 Research Background

Extensive research effort has been paid to solving the challenges of Li–S batteries and significant improvement has been achieved in the past several years [1, 2]. Although these developments are encouraging, sulfur loading in the cathode is inadequate, which greatly offsets the advantageous high-energy density of Li–S batteries [3]. In most reported cases, the areal loading of sulfur on the electrode was less than 2.0 mg $cm^{-2}$ and sulfur-containing composites had a sulfur fraction below 70 wt% [4, 5]. Therefore, it is necessary to develop new strategies that not only can improve the cyclic stability of Li–S batteries but also increase the sulfur loading and hence maintain their energy density advantage. On the other hand, flexible energy storage devices are necessary for next-generation, high-performance flexible, and wearable electronic devices [6, 7]. Therefore, great attention has been paid to the exploration of new battery systems with mechanical flexibility and high-energy density based on a multi-electrons reaction [8, 9].

Aluminum (Al) foil as a current collector and a routine blade-coating procedure are widely used to fabricate Li–S batteries. This traditional battery production process does not allow a high mass loading because a thick electrode tends to delaminate from the Al current collector after coating and drying. Furthermore, the kinetic limitation of lithium diffusion through a thick electrode would induce large polarization and, as a consequence, loss of energy efficiency [10, 11]. In contrast, an interconnected porous current collector, which avoids the peeling off of the thick active material from the current collector, could be used to improve the energy density per unit area [11, 12]. The interconnected structural design would also minimize electron and ion transport resistance, which also plays an important role in improving the electrochemical performance of a battery [13].

In this chapter, we have developed a flexible Li–S battery electrode using graphene foam (GF) as a current collector and host for large sulfur loading through simple slurry infiltration. A well-mixed sulfur slurry (70 wt% pure sulfur, 20 wt%



G. Zhou, *Design, Fabrication and Electrochemical Performance of Nanostructured Carbon Based Materials for High-Energy Lithium–Sulfur Batteries*, Springer Theses,
DOI 10.1007/978-981-10-3406-0_6

carbon black, and 10 wt% PVDF) was simply filtered into a graphene/poly(dimethyl siloxane) (PDMS) foam. The PDMS coating on the GF makes this interconnected network sufficiently robust, guaranteeing the flexibility of the cathode. The interconnected GF provides efficient electron pathways, offers vast void space to accommodate a significant amount of active material and holds sufficient electrolyte. With such a design, the sulfur loading can be as high as 10.1 mg $cm^{-2}$, giving a discharge capacity of 13.4 mAh $cm^{-2}$, values that are much higher than those reported for most Li–S batteries [2, 14, 15]. More importantly, the sulfur-PDMS/GF (S-PDMS/GF) electrode possesses excellent flexibility and electrochemical performance, and the capacity decay after 1000 cycles is as small as 0.07% per cycle.

## 6.2 Fabrication and Characterization of the 3D GF-Based Electrode

### *6.2.1 Preparation of PDMS/GF*

Graphene was grown on a Ni foam (Dalian Alantum Advanced Technology Materials Co. Ltd., ~380 g $m^{-2}$ in areal density) by CVD as previously reported [16, 17]. The Ni foam was heated to 1000 °C in a horizontal tube furnace (Lindberg Blue M, TF55030C, and the outer diameter and inner diameter of the quartz tube were 75 and 72 mm) under $H_2$ and annealed for 15 min to clean its surface and eliminate a thin surface oxide layer. An appropriate amount of $CH_4$ (100 s.c.c.m.), corresponding to a concentration of 29 vol.% in the total gas flow, was then introduced into the reaction tube with $H_2$ (50 s.c.c.m.) and Ar (200 s.c.c.m.) at ambient pressure. After 30 min reaction, the sample was rapidly cooled to room temperature at a rate of ~100 °C $min^{-1}$ under Ar and $H_2$. After CVD growth, a thin layer of PDMS was coated onto the surface of the graphene grown on the Ni foam by dipping the sample into a dilute PDMS solution (a mixture of a PDMS base agent, curing agent (Sylgard 184, Dow Corning) and ethyl acetate in the ratio of 10:1:200) for 30 min followed by curing at 80 °C for 4 h. The Ni substrate was then etched away by a HCl solution (3 M) at 80 °C for 12 h to obtain the PDMS/GF composite.

### *6.2.2 Preparation of S-PDMS/GF Electrode*

A homogeneous sulfur-containing slurry was fabricated by mixing 70 wt% sulfur with 20 wt% conductive carbon black as a conducting agent and 10 wt% PVDF as a binder dissolved in N-methyl-2-pyrrolidone (NMP). The slurry was then cast into

the PDMS/GF with a controlled sulfur loadings ranging from 3.3 to 10.1 mg $cm^{-2}$ to obtain S-PDMS/GF electrodes. The electrodes obtained were then dried in a vacuum drying oven at 60 °C for 24 h.

### 6.2.3 *Structure Characterization of the S-PDMS/GF Electrode*

The synthesis procedure is illustrated in Fig. 6.1a. A nickel (Ni) foam was used as a catalyst template for the CVD growth of graphene [16]. Then a thin layer of PDMS was coated on the surface of the GF. The subsequent removal of the Ni gives rise to a free-standing, robust interconnected PDMS/GF composite. As shown in Fig. 6.1b and c, the PDMS/GF exhibits good flexibility, and can be bent into arbitrary shapes without fracture. An electrode was then prepared by casting a well-mixed sulfur slurry into the PDMS/GF followed by drying. The interconnected graphene network remains intact during the electrode fabrication and the S-PDMS/GF electrode remains flexible after loading with a large amount of sulfur (Fig. 6.1d, e). The sulfur loading in this electrode could reach 10.1 mg $cm^{-2}$. For comparison, we also

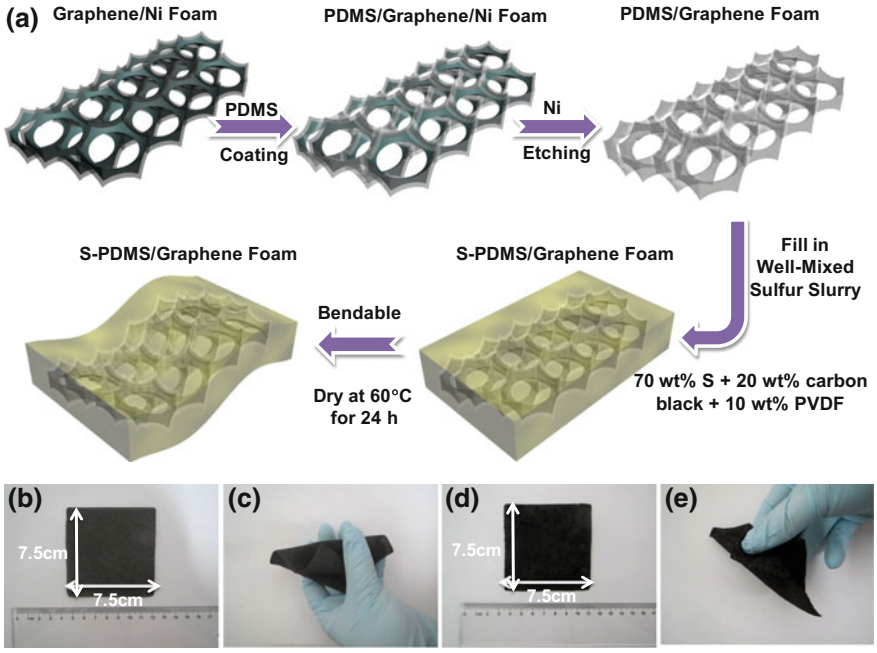


**Fig. 6.1** **a** Schematic of the procedure for fabricating PDMS/GF and S-PDMS/GF electrodes. **b**, **c** Photographs of a PDMS/GF (7.5 cm × 7.5 cm) showing its good flexibility. **d**, **e** Photographs of a flexible S-PDMS/GF electrode (7.5 cm × 7.5 cm) with 10.1 mg $cm^{-2}$ sulfur loading

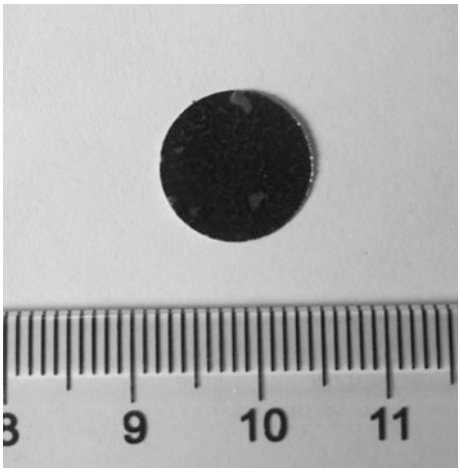


**Fig. 6.2** Photograph of an electrode with sulfur coated onto an Al foil current collector (6.2 mg $cm^{-2}$ sulfur loading)

used traditional blade-coating technology for the preparation of sulfur electrodes. When the sulfur loading reached 6.2 mg $cm^{-2}$, many cracks were observed on the surface of the electrode and the detachment of the active material from an Al current collector occurred (Fig. 6.2). This is due to the weak bonding between the thick sulfur electrode and the Al current collector. These observations show that the porous electrode design can load more active material, because it provides enough 3D space to accommodate sulfur rather than limiting it to the surface of a current collector.

From SEM observations, the PDMS/GF perfectly copied the interconnected network structure of the Ni foam, which is highly porous (Fig. 6.3a). The electrical conductivity of the PDMS/GF was about 480 S $m^{-1}$ measured by the four-point probe method. It could therefore serve as a porous framework that provides active materials with mechanical support and an electrically conductive network, which is confirmed by the following structural analysis. The interconnected network with 50–200 μm macropores could also serve as an electrolyte ion-buffering reservoir, facilitating electrolyte ion diffusion to the active material [18]. The sulfur-containing slurry is a mixture of commercially available sulfur particles, PVDF and carbon black, and homogeneous filling of the PDMS/GF by the sulfur slurry can be observed in Fig. 6.3b–d. By changing the concentration of the slurry, three S-PDMS/GF electrodes with different sulfur loadings, 3.3, 6.1 and 10.1 mg $cm^{-2}$, were obtained. When the sulfur loading was low, sulfur particles were mainly glued to the skeleton of the PDMS/GF by the PVDF/carbon black matrix. With an increase of sulfur loading, the sulfur particles filled the macropores of the interconnected network. The electrode structure was also reconstructed and visualized by X-ray microtomography (XRM), as shown in Fig. 6.3e–h, which confirms sulfur distribution in the porous graphene network. Figure 6.3e, g give the 2D projections of the S-PDMS/GF electrodes with sulfur loadings of 3.3 and 10.1 mg $cm^{-2}$, respectively. It can be clearly seen that the concentration of sulfur particles is

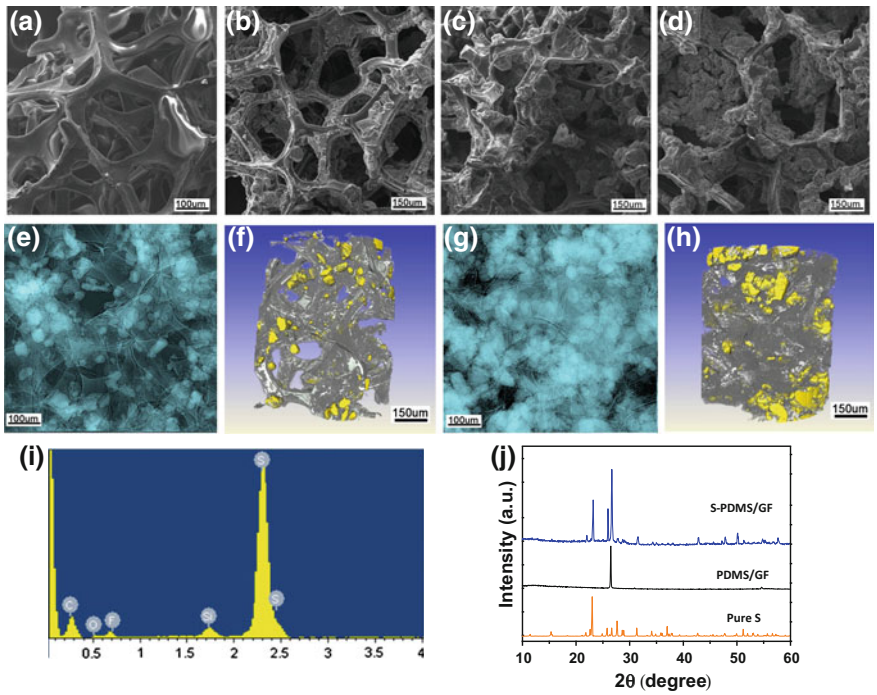


**Fig. 6.3** **a** SEM image of a PDMS/GF. **b–d** SEM images of S-PDMS/GF electrodes with different sulfur loading amounts of 3.3, 6.1 and 10.1 mg $cm^{-2}$. **e**, **g** XRM 2D projections of S-PDMS/GF electrodes with 3.3 and 10.1 mg $cm^{-2}$ sulfur loading. **f**, **h** 3D images of the reconstructed S-PDMS/GF electrodes with 3.3 and 10.1 mg $cm^{-2}$ sulfur loading (graphene and carbon black marked in *gray*, sulfur particles marked in *yellow* and PDMS marked in *white*). **i** EDS analysis of S-PDMS/GF electrodes (unit: keV). **j** XRD patterns of S-PDMS/GF, PDMS/GF and pure sulfur

distinctly increased. Figure 6.3f and h display the 3D volume renderings of S-PDMS/GF electrodes, in which the PDMS is distributed uniformly on the interlinked GF and both serve as a skeleton to support the sulfur particles. The sulfur particles together with the PVDF and carbon black are dispersed evenly in the porous conductive and flexible framework. EDS analysis of the S-PDMS/GF electrode is shown in Fig. 6.3i. C, O, S, F, and Si elements are presented and there is no peak from Ni, indicating that the etching process was complete. The F and Si come from PVDF and PDMS, respectively. XRD patterns of S-PDMS/GF, PDMS/GF and pure sulfur are shown in Fig. 6.3j. Sharp diffraction peaks are observed in the S-PDMS/GF, indicating the orthorhombic structure of sulfur (JCPDS card No. 08-0247) and the diffraction peaks at around 26° and 54° mainly correspond to the graphene, which is consistent with the EDS analysis.

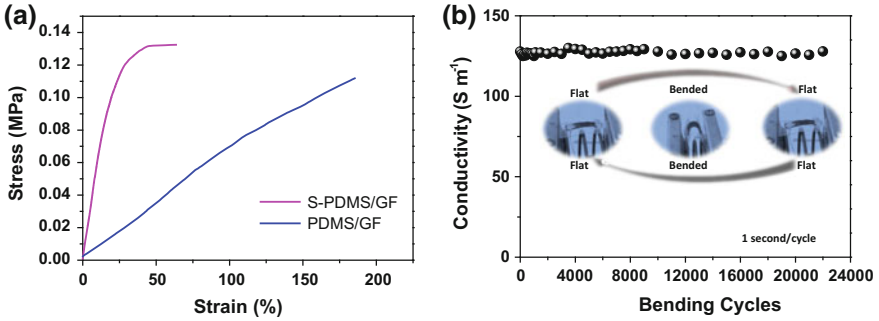


**Fig. 6.4** **a** Stress-strain curves of a PDMS/GF and S-PDMS/GF electrode with 10.1 mg $cm^{-2}$ sulfur loading. **b** Stability of a S-PDMS/GF electrode with 10.1 mg $cm^{-2}$ sulfur loading in terms of electrical conductivity over 22,000 cycles

## 6.3 Mechanical Properties of the 3D GF-Based Electrode

Stress-strain curves of the S-PDMS/GF electrode and PDMS/GF are shown in Fig. 6.4a. After filling the PDMS/GF with the well-mixed sulfur slurry, the modulus of the material was improved (0.06 MPa for PDMS/GF and 0.42 MPa for S-PDMS/GF), which indicates that the stiffness of the electrode was increased. Although the elongation of the S-PDMS/GF compared with PDMS/GF is lower, the 20% elastic strain of the S-PDMS/GF is still higher than or comparable to other values reported to date [19–22]. The dynamic electrical properties of the S-PDMS/GF electrode were investigated by measuring the changes of electrical resistance and conductivity during the bend cycling process. The electrode showed a high electrical conductivity of $\sim$125 S $m^{-1}$, which remained unchanged after 22,000 bending cycles (Fig. 6.4b). The resistance curves for the first and last 50 bending cycles are shown in Fig. 6.5, indicating that the resistance of the electrode was very stable for many cycles. After bending 22,000 times, no cracks were

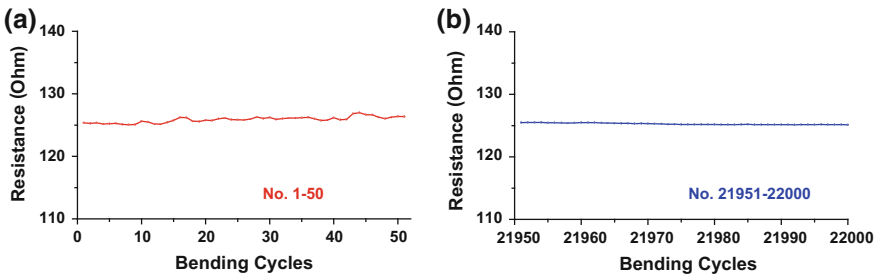


**Fig. 6.5** Typical resistance variation of the S-PDMS/GF electrode (10.1 mg $cm^{-2}$ sulfur loading) during the **a** first 50 cycles and **b** last 50 cycles of a 22,000 cycle test

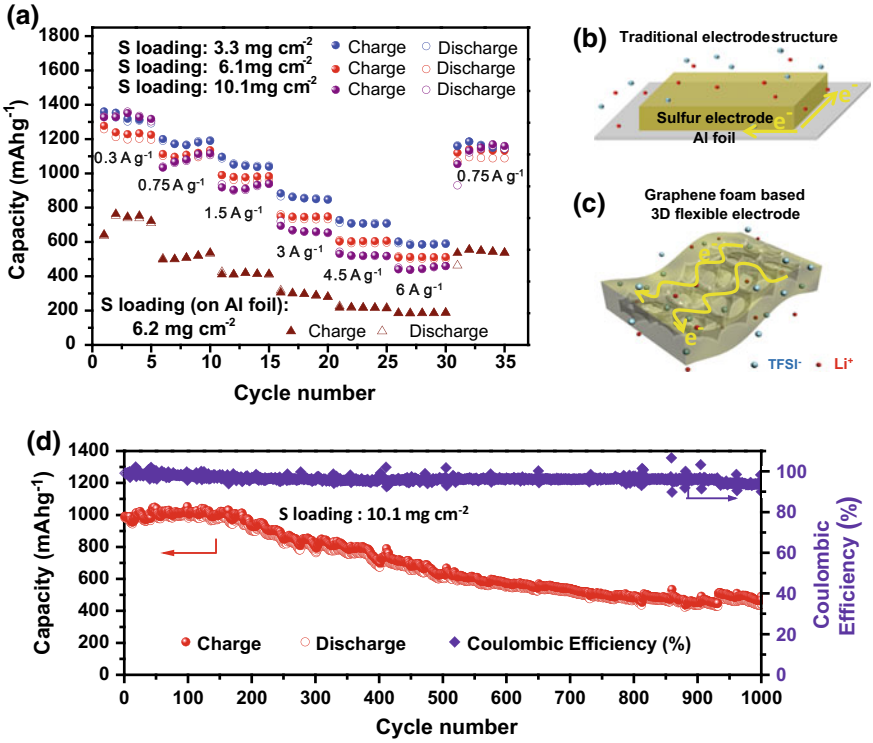


**Fig. 6.6** **a** Rate performance of the S-PDMS/GF electrodes with different sulfur loadings and the electrode with sulfur coated on an Al foil (Due to the activation process, we took the stable sixth to tenth cycles of rate performance for the 10.1 mg $cm^{-2}$ sulfur-loaded electrode under the current density of 300 mA $g^{-1}$ to compare with other sulfur-loaded electrodes). **b** and **c** Comparison between electrode design in which sulfur is coated on an Al foil and a GF-based flexible electrode. **d** Cycling performance and Coulombic efficiency of the S-PDMS/GF electrode with a 10.1 mg $cm^{-2}$ sulfur loading at 1500 mA $g^{-1}$ for 1000 cycles

observed in the electrode. All these results suggest that the S-PDMS/GF electrode shows excellent stretchability, high electrical conductivity, and long-term bending durability, which is promising for high-performance flexible electrode materials.

## 6.4 Electrochemical Performance of the 3D GF-Based Sulfur Electrode

In order to evaluate the electrochemical performance of the flexible electrode with a large sulfur loading, coin cells were assembled. When the discharge current density was increased from 300 to 6000 mA $g^{-1}$ (Fig. 6.6a), the electrodes delivered a reversible capacity higher than 450 mAh $g^{-1}$, which indicates an ultrafast

**Table 6.1** The electrical conductivity of different materials measured using the four-point probe method

| Materials | Graphene foam (GF) | PDMS/GF | S-PDMS/GF (3.3 mg $cm^{-2}$) | S-PDMS/GF (6.1 mg $cm^{-2}$) | S-PDMS/GF (10.1 mg $cm^{-2}$) |
|---|---|---|---|---|---|
| Conductivity (S $m^{-1}$) | ~2000 | ~480 | ~210 | ~165 | ~130 |

charge/discharge capability. It was noticed that the rate performance changed with increased sulfur loading mainly because of the difference in electrical conductivity, which is consistent with the results measured by the four-point probe method (Table 6.1). When the current density was changed back to 750 mA $g^{-1}$, these cells resumed their original capacity of over 1000 mAh $g^{-1}$, exhibiting good capacity retention. In contrast, active material on an Al foil could not show this ability, owing to poor bonding between the thick active material and the Al current collector. Figure 6.6b and c illustrate the structural differences between the GF-based flexible electrode and the electrode with sulfur coated on an Al foil current collector. The current collector mainly plays a role in supporting the active materials and offering a continuous conductive pathway. The GF current collector could provide enough space to accommodate and load active material, and act as an inner conductive network. Different from the Al current collector with active materials only on the surface, the GF-based current collector with an interconnected network is beneficial for providing good electrical and electrolyte contact [11]. The galvanostatic charge/discharge behavior of the S-PDMS/GF was evaluated at different current densities (Fig. 6.7, 6.1 mg $cm^{-2}$ sulfur loading). The discharge/charge profiles typically have two plateaus, which correspond to the reduction of elemental sulfur to lithium polysulfides at 2.3–2.4 V and the formation of $Li_2S_2/Li_2S$ at around 2 V [23, 24].

It is worth pointing out that with increased sulfur loading, especially when it reaches 10.1 mg $cm^{-2}$, not all sulfur particles take part in the electrochemical

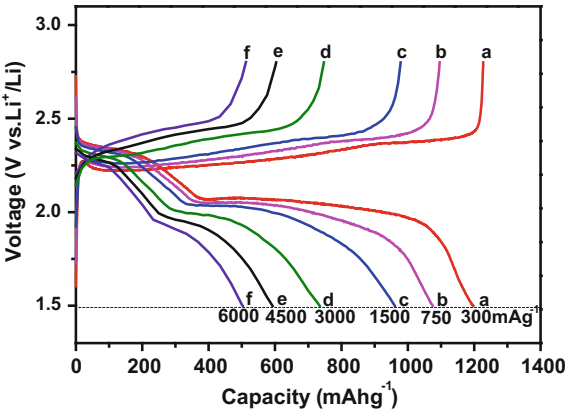


**Fig. 6.7** Galvanostatic charge/discharge curves of the S-PDMS/GF electrode with 6.1 mg $cm^{-2}$ sulfur loading

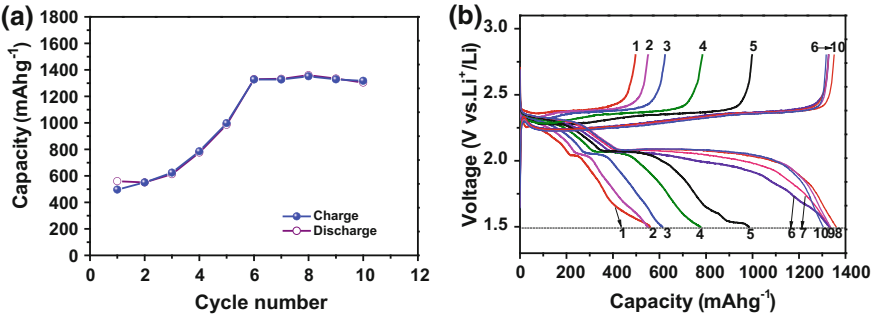


**Fig. 6.8** **a** The initial ten cycles of the S-PDMS/GF electrode with 10.1 mg $cm^{-2}$ sulfur loading under the current density of 300 mA $g^{-1}$ and **b** the corresponding galvanostatic charge/discharge curves

reaction during the first few cycles (Fig. 6.8a). This phenomenon was found in previous papers on high sulfur-loaded electrodes [25, 26]. This is because the reaction of sulfur to lithium polysulfides and finally to $Li_2S_2/Li_2S$ is a solid–liquid–solid transformation, which needs time to achieve "sulfur activation" [26]. Therefore, the plateaus around 2.0 and 2.3 V in the discharge/charge profiles become more and more obvious (Fig. 6.8b). The activation process of sulfur affects the capacity and the first Coulombic efficiency of Li–S batteries, but its influence is gradually eliminated during the subsequent cycling. Figure 6.6d and Fig. 6.9 show

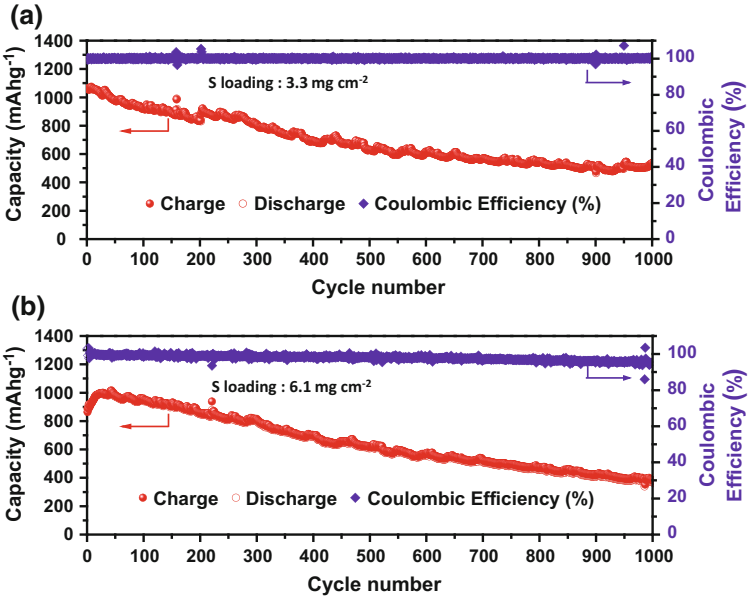


**Fig. 6.9** Cycling performance and Coulombic efficiency of the S-PDMS/GF electrodes with **a** 3.3 and **b** 6.1 mg $cm^{-2}$ sulfur loading at 1500 mA $g^{-1}$ for 1000 cycles

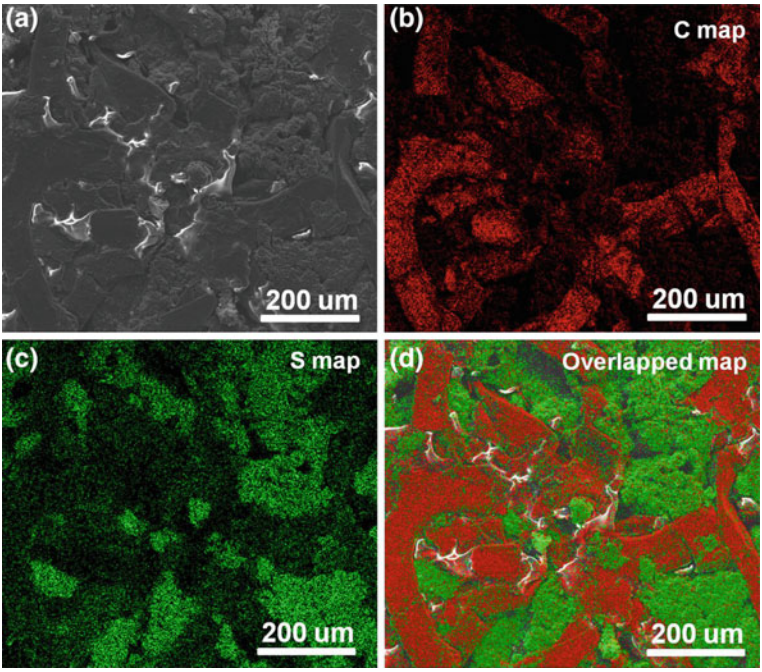


**Fig. 6.10** **a** SEM image of the S-PDMS/GF electrode after cycling. **b** Carbon, **c** sulfur, and **d** carbon and sulfur overlapped elemental mapping of the S-PDMS/GF electrode after cycling

the cycling performance of the S-PDMS/GF electrodes with different sulfur loadings from 3.3 to 10.1 mg $cm^{-2}$. After 1000 cycles at a current density of 1500 mA $g^{-1}$, all of these sulfur electrodes exhibited good cyclic performance, retaining capacities of 527, 467 and 448 mAh $g^{-1}$, respectively, with a Coulombic efficiency above 95%. The corresponding capacity decays are only 0.066%, 0.083%, and 0.071% per cycle.

Post-cycling SEM and XRM characterizations were used to reveal the integrity of the electrode and the maintaining of sulfur in the GF matrix. The cell was disassembled in a glovebox, and the S-PDMS/GF electrode with a sulfur loading of 10.1 mg $cm^{-2}$ was taken out and washed using a 1, 2-dimethoxyethane solution. As shown in Figs. 6.10a and 6.11, the overall morphology and structure of the S-PDMS/GF electrode materials were well preserved, and the carbon, sulfur, and their overlapped element mappings confirmed that the sulfur is still uniformly embedded in the GF matrix (Fig. 6.10b–d), indicating the structural stability of the electrode. 3D XRM image of the S-PDMS/GF electrode after cycling showed sulfur particle refinement and its dispersed state in the GF framework (Fig. 6.11b), which is consistent with our previous results [27].

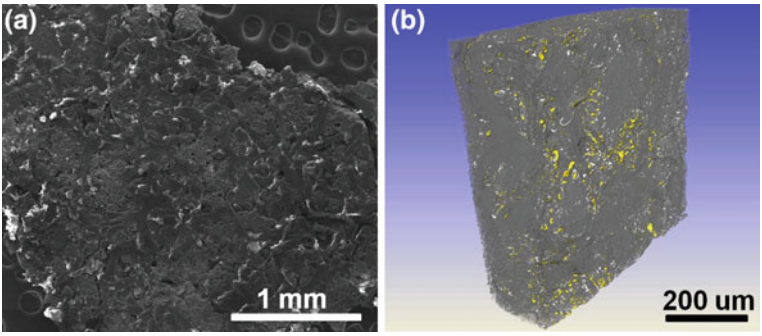


**Fig. 6.11** **a** SEM image of the S-PDMS/GF electrode after cycling. **b** 3D image of the reconstructed S-PDMS/GF electrode with 10.1 mg $cm^{-2}$ sulfur loading after cycling (graphene and carbon black marked in *gray*, sulfur particles marked in *yellow* and PDMS marked in *white*)

## 6.5 Areal Capacity of the 3D GF-Based Sulfur Electrode

The areal capacity of S-PDMS/GF electrodes was calculated, as shown in Fig. 6.12a. A very high areal capacity (13.4 mAh $cm^{-2}$ at 300 mA $g^{-1}$) of the sulfur cathode with the high sulfur loading (10.1 mg $cm^{-2}$) was obtained. The areal capacity of present LIB cathodes (such as $LiCoO_2$) with areal loadings of 20–30 mg $cm^{-2}$ is ~3–4 mAh $cm^{-2}$ [28]. The areal capacity of the present Li–S battery electrodes with a cathode areal loading of 0.5–2 mg $cm^{-2}$ is only between 0.5 and 3 mAh $cm^{-2}$ [14, 15]. Therefore, it is clear that the areal capacity of the S-PDMS/GF electrode is much higher than that of reported $LiCoO_2$ and sulfur electrodes. Furthermore, the S-PDMS/GF electrode with a sulfur loading of 10.1 mg $cm^{-2}$ and high sulfur content of 70 wt% could deliver a high areal capacity of 9.3 mAh $cm^{-2}$ at a high current density of 1500 mA $g^{-1}$ (corresponding to 3.6 mA $cm^{-2}$). Even at a very high current density of 14.4 mA $cm^{-2}$ (6000 mA $g^{-1}$), its areal capacity was higher than 4.5 mAh $cm^{-2}$.

For comparison, the areal capacities based on sulfur were approximately estimated from some recent publications (Fig. 6.12b, c, Tables 6.2 and 6.3). From Fig. 6.12b and Table 6.2, it can be concluded that a large sulfur loading on a porous electrode is an efficient way to obtain a high areal capacity for a Li–S battery. At the same time, the overall areal capacities were also calculated and compared taking into account the weight of the current collectors, as shown in Fig. 6.12c and Table 6.3. The sulfur content in the S-PDMS/GF electrode with a sulfur loading of 10.1 mg $cm^{-2}$ was ~50 wt% (including PDMS, carbon black and PVDF) based on thermogravimetric analysis (Fig. 6.13). After considering the weight of the current collectors, the areal capacity of the S-PDMS/GF electrodes is even more attractive compared to

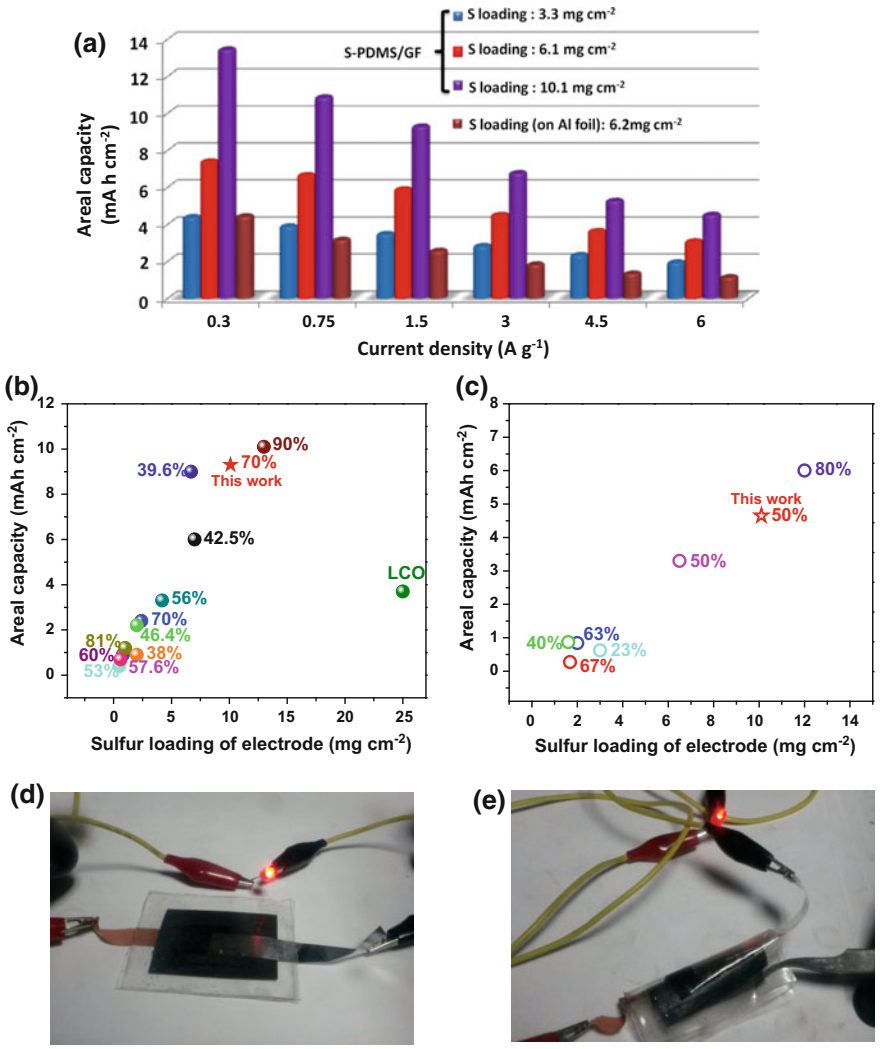


**Fig. 6.12** **a** Areal capacity at different current densities of the S-PDMS/GF electrodes with different sulfur loadings and an electrode with sulfur coated on an Al foil. **b** Comparison of areal capacity and sulfur weight percentage of the S-PDMS/GF electrode with that of Li–S batteries (based on sulfur) and $LiCoO_2$ from some recent publications (★ [this work] @ 1500 mA $g^{-1}$ corresponding to 3.60 mA $cm^{-2}$, ● [29] @ 167 mA $g^{-1}$ corresponding to 1.17 mA $cm^{-2}$, ● [30] @ 1675 mA $g^{-1}$, ● [31] @ 1500 mA $g^{-1}$, ● [32] @ 1675 mA $g^{-1}$, ● [33] @ 1675 mA $g^{-1}$, ● [34] @ 1672 mA $g^{-1}$, ● [35] @ 1675 mA $g^{-1}$, ● [36] @ 335 mA $g^{-1}$, ● [28] @ 4.20 mA $cm^{-2}$, ● [37] @ 0.70 mA $cm^{-2}$, ● [3] @ 0.50 mA $cm^{-2}$ and ● [28] $LiCoO_2$ @ 145 mA $g^{-1}$). **c** Comparison of overall areal capacity and sulfur weight percentage of the S-PDMS/GF electrode with that of Li–S batteries from some recent publications taking the weight of the current collector into consideration (☆ [this work] @ 1500 mA $g^{-1}$ corresponding to 3.60 mA $cm^{-2}$, ○ [38] @ 1675 mA $g^{-1}$ corresponding to 2.57 mA $cm^{-2}$, ○ [20] @ 1500 mA $g^{-1}$, ○ [23] @ 1500 mA $g^{-1}$, ○ [39] @ 150 mA $g^{-1}$ corresponding to 0.98 mA $cm^{-2}$, ○ [25] @ 165 mA $g^{-1}$, ○ [40] @ 1675 mA $g^{-1}$). **d** and **e** Photographs of a prototype flexible Li–S battery lighting a red LED device under flat and bent states (color figure online)

**Table 6.2** Comparison of areal capacity of the S-PDMS/GF electrode with those from some recent publications about Li–S batteries (based on sulfur) and $LiCoO_2$ cathode

| Symbol | Material | Sulfur (or LCO) percentage of electrode (%) | Sulfur loading of electrode (mg $cm^{-2}$) | Current density | Areal capacity (mAh $cm^{-2}$) | Refs. |
|---|---|---|---|---|---|---|
| ★ | Sulfur-PDMS/ Graphene foam | 70.0 | 10.1 | 3.60 mA $cm^{-2}$ | 9.3 | This work |
| ● | Al foam current collector with the CNT/Sulfur | 42.5 | 7.0 | 1.17 mA $cm^{-2}$ | 6.0 | [29] |
| ● | Sulfur-$TiO_2$ Yolk-Shell Nanoarchitecture | 53.0 | 0.5 | 1675 mA $g^{-1}$ | 0.4 | [30] |
| ● | GCC/S+G-separator | 70.0 | 2.4 | 1500 mA $g^{-1}$ | 2.4 | [31] |
| ● | S@Sandwich-type hybrid Carbon nanosheets consisting of Graphene and Micro/Mesoporous Carbon layer | 60.0 | 0.8 | 1675 mA $g^{-1}$ | 0.9 | [32] |
| ● | S@C NWs | 81.0 | 1.0 | 1675 mA $g^{-1}$ | 1.2 | [33] |
| ● | Unstacked double-layer template Graphene/S | 57.6 | 0.6 | 1672 mA $g^{-1}$ | 0.7 | [34] |
| ● | Sulfur-Polypyrrole | 38.0 | 2.0 | 1675 mA $g^{-1}$ | 0.9 | [35] |
| ● | Polyaniline-Sulfur core-shell structure | 46.4 | 2.0 | 335 mA $g^{-1}$ | 2.2 | [36] |
| ● | Polyacrylonitrile (PAN)-Derived C-S Composite | 39.6 | 6.7 | 4.20 mA $cm^{-2}$ | 9.0 | [28] |
| ● | Mesoporous Nitrogen-doped Carbon–Sulfur Nanocomposite | 56.0 | 4.2 | 0.70 mA $cm^{-2}$ | 3.3 | [37] |
| ● | Sulfur Membrane@Carbon Cloth | 90.0 | 13.0 | 0.50 mA $cm^{-2}$ | 10.1 | [3] |
| ● | LCO | 92.0 | 25.0 | 145 mA $g^{-1}$ | 3.7 | [4] |

conventional planar electrodes. In order to verify the feasibility of this flexible electrode design, we fabricated a flexible prototype Li–S battery (Fig. 6.14) with a high sulfur-loaded electrode according to the method previously reported [41]. This prototype Li–S battery showed excellent flexibility, and could power a red light-emitting diode (LED) when it was flat or bent, as shown in Fig. 6.12d and e.

**Table 6.3** Comparison of overall areal capacity of the S-PDMS/GF electrode with some recent publications about Li–S batteries when taking the weight of current collector into consideration

| Symbol | Material | Sulfur percentage of electrode (%) | Sulfur loading of electrode (mg $cm^{-2}$) | Current density | Areal capacity (mAh $cm^{-2}$) | Refs. |
|---|---|---|---|---|---|---|
| ☆ | Sulfur-PDMS/Graphene foam | 50.0 | 10.1 | 3.60 mA $cm^{-2}$ | 4.65 | This work |
| ○ | Graphene/Sulfur paper | 67.0 | 1.68 | 2.57 mA $cm^{-2}$ | 0.27 | [38] |
| ○ | Sulfur-CNTs paper | 23.0 | 3.0 | 1500 mA $g^{-1}$ | 0.62 | [20] |
| ○ | Graphene/Sulfur hybrids | 63.0 | 2.0 | 1500 mA $g^{-1}$ | 0.84 | [23] |
| ○ | Carbon cloth/ Sulfur | 50.0 | 6.5 | 0.98 mA $cm^{-2}$ | 3.3 | [39] |
| ○ | Sulfur-Graphene sponge | 80.0 | 12.0 | 165 mA $g^{-1}$ | 6.0 | [25] |
| ○ | Sulfur/multi-wall Carbon Nanotube | 40.0 | 1.6 | 1675 mA $g^{-1}$ | 0.87 | [40] |

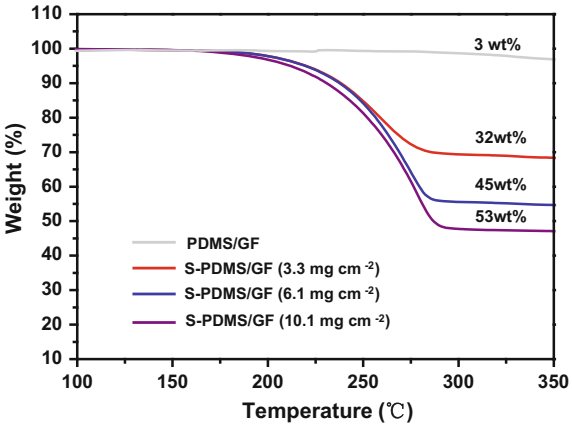


**Fig. 6.13** Thermogravimetric curves of S-PDMS/GF electrodes with different sulfur loadings in Ar with a heating rate of 10 °C $min^{-1}$, indicating sulfur contents of 29, 42 and 50 wt% (after eliminating the slight weight loss (about 3 wt%) of PDMS/GF) in the whole electrode (including the current collector)

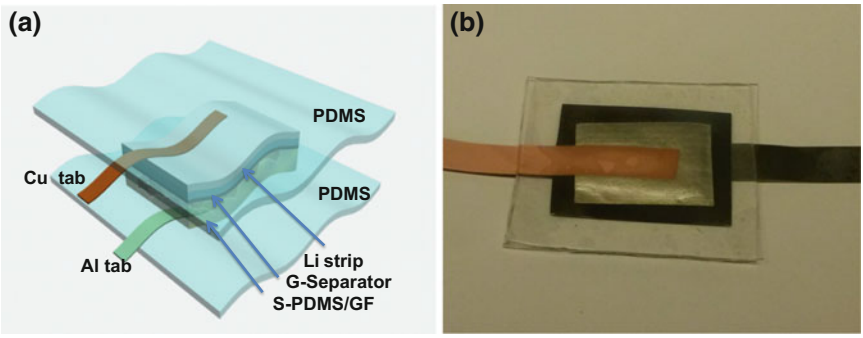


**Fig. 6.14** **a** Diagram and **b** corresponding photograph of a prototype flexible Li–S battery using a S-PDMS/GF electrode as cathode and lithium strip as anode

## 6.6 Conclusion

In this chapter, we proposed an effective strategy to obtain flexible Li–S battery electrodes with high-energy density, high power density, and long cyclic life by adopting GF-based electrodes. GF can provide a highly electrically conductive network, robust mechanical support, and sufficient space for a high sulfur loading. The main conclusions are as follows:

1. The sulfur loading in GF-based electrodes can be tuned from 3.3 to 10.1 mg $cm^{-2}$.
2. The electrode with 10.1 mg $cm^{-2}$ sulfur loading could deliver an extremely high areal capacity of 13.4 mAh $cm^{-2}$, much higher than the commonly reported Li–S electrodes and commercially used lithium cobalt oxide cathode with a value of $\sim$3–4 mAh $cm^{-2}$.
3. The high sulfur-loaded electrodes retain a high rate performance with reversible capacities higher than 450 mAh $g^{-1}$ under a large current density of 6 A $g^{-1}$ and preserve stable cycling performance with $\sim$0.07% capacity decay per cycle over 1000 cycles.
4. The S-PDMS/GF electrode shows excellent stretchability, high electrical conductivity and long-term bending durability, which is promising for high-performance flexible electrode materials.
5. A flexible prototype Li–S battery with a high sulfur-loaded electrode was demonstrated with excellent flexibility, and could power a red light-emitting diode when it was flat or bent.

## References

1. Evers S, Nazar LF (2013) New approaches for high energy density lithium–sulfur battery cathodes. Acc Chem Res 46(5):1135–1143
2. Yang Y, Zheng G, Cui Y (2013) Nanostructured sulfur cathodes. Chem Soc Rev 42(7):3018–3032
3. Zhang SS, Tran DT (2012) A proof-of-concept lithium/sulfur liquid battery with exceptionally high capacity density. J Power Sources 211:169–172
4. Hagen M et al (2013) Development and costs calculation of lithium–sulfur cells with high sulfur load and binder free electrodes. J Power Sources 224:260–268
5. Gao J, Abruña HD (2014) Key parameters governing the energy density of rechargeable Li/S batteries. J Phys Chem Lett 5(5):882–885
6. Jeong G, Kim Y-U, Kim H, Kim Y-J, Sohn H-J (2011) Prospective materials and applications for Li secondary batteries. Energy Environ Sci 4(6):1986–2002
7. Lee S-Y et al (2013) Progress in flexible energy storage and conversion systems, with a focus on cable-type lithium–ion batteries. Energy Environ Sci 6:2414–2423
8. Gao XP, Yang HX (2010) Multi-electron reaction materials for high energy density batteries. Energy Environ Sci 3(2):174–189
9. Zhou G, Li F, Cheng H-M (2014) Progress in flexible lithium batteries and future prospects. Energy Environ Sci 7:1307–1338
10. Fongy C, Gaillot A-C, Jouanneau S, Guyomard D, Lestriez B (2010) Ionic vs electronic power limitations and analysis of the fraction of wired grains in $LiFePO_4$ composite electrodes. J Electrochem Soc 157(7):A885–A891
11. Hu L et al (2011) Lithium-Ion textile batteries with large areal mass loading. Adv Energy Mater 1(6):1012–1017
12. Mazouzi D et al (2014) Very high surface capacity observed using Si negative electrodes embedded in copper foam as 3D current collectors. Adv Energy Mater 4(8):1301718
13. Pikul JH, Gang Zhang H, Cho J, Braun PV, King WP (2013) High-power lithium ion microbatteries from interdigitated three-dimensional bicontinuous nanoporous electrodes. Nat Commun 4:1732

14. Wang D-W et al (2013) Carbon–sulfur composites for Li–S batteries: status and prospects. J Mater Chem A 1(33):9382–9394
15. Manthiram A, Fu Y, Chung S-H, Zu C, Su Y-S (2014) Rechargeable lithium–sulfur batteries. Chem Rev 114(23):11751–11787
16. Chen ZP et al (2011) Three-dimensional flexible and conductive interconnected graphene networks grown by chemical vapour deposition. Nat Mater 10(6):424–428
17. Chen Z, Xu C, Ma C, Ren W, Cheng H-M (2013) Lightweight and flexible graphene foam composites for high-performance electromagnetic interference shielding. Adv Mater 25 (9):1296–1300
18. Wang DW, Li F, Liu M, Lu GQ, Cheng HM (2008) 3D aperiodic hierarchical porous graphitic carbon material for high-rate electrochemical capacitive energy storage. Angew Chem Int Ed 47(2):373–376
19. Jia XL et al (2012) Building robust architectures of carbon and metal oxide nanocrystals toward high-performance anodes for lithium–ion batteries. ACS Nano 6(11):9911–9919
20. Zhou GM et al (2012) A flexible nanostructured sulphur-carbon nanotube cathode with high rate performance for Li–S batteries. Energy Environ Sci 5(10):8901–8906
21. Wang K et al (2013) Super-aligned carbon nanotube films as current collectors for lightweight and flexible lithium ion batteries. Adv Funct Mater 23(7):846–853
22. Luo S et al (2012) Binder-free $LiCoO_2$/carbon nanotube cathodes for high-performance lithium ion batteries. Adv Mater 24(17):2294–2298
23. Zhou GM et al (2013) Fibrous hybrid of graphene and sulfur nanocrystals for high-performance lithium–sulfur batteries. ACS Nano 7(6):5367–5375
24. Ji XL, Lee KT, Nazar LF (2009) A highly ordered nanostructured carbon–sulphur cathode for lithium–sulphur batteries. Nat Mater 8(6):500–506
25. Lu S, Chen Y, Wu X, Wang Z, Li Y (2014) Three-dimensional sulfur/graphene multifunctional hybrid sponges for lithium–sulfur batteries with large areal mass loading. Sci Rep 4:4629
26. Miao L, Wang W, Yuan K, Yang Y, Wang A (2014) A lithium-sulfur cathode with high sulfur loading and high capacity per area: a binder-free carbon fiber cloth-sulfur material. Chem Commun 50:13231–13234
27. Zhou GM et al (2015) A flexible sulfur–graphene–polypropylene separator integrated electrode for advanced Li–S batteries. Adv Mater 27(4):641–647
28. Kim J-S, Hwang TH, Kim BG, Min J, Choi JW (2014) A lithium–sulfur battery with a high areal energy density. Adv Funct Mater 24(34):5359–5367
29. Cheng X-B et al (2014) Three-dimensional aluminum foam/carbon nanotube scaffolds as long- and short-range electron pathways with improved sulfur loading for high energy density lithium–sulfur batteries. J Power Sources 261:264–270
30. Seh Z et al (2013) Sulphur–$TiO_2$ yolk–shell nanoarchitecture with internal void space for long-cycle lithium–sulphur batteries. Nat Commun 4:1331
31. Zhou GM et al (2014) A graphene–pure-sulfur sandwich structure for ultrafast, long-life lithium–sulfur batteries. Adv Mater 26(4):625–631
32. Xa Chen et al (2014) Sulfur-impregnated, sandwich-type, hybrid carbon nanosheets with hierarchical porous structure for high-performance lithium–sulfur batteries. Adv Energy Mater 4(13):1301988
33. Moon S et al (2013) Encapsulated monoclinic sulfur for stable cycling of Li–S rechargeable batteries. Adv Mater 25(45):6547–6553
34. Zhao M-Q et al (2014) Unstacked double-layer templated graphene for high-rate lithium–sulphur batteries. Nat Commun 5:3410
35. Fu Y, Manthiram A (2012) Orthorhombic bipyramidal sulfur coated with polypyrrole nanolayers as a cathode material for lithium–sulfur batteries. J Phys Chem C 116(16):8910–8915
36. Zhou W, Yu Y, Chen H, DiSalvo FJ, Abruña HD (2013) Yolk-shell structure of polyaniline-coated sulfur for lithium-sulfur batteries. J Am Chem Soc 135(44):16736–16743

37. Song J et al (2014) Nitrogen-doped mesoporous carbon promoted chemical adsorption of sulfur and fabrication of high-areal-capacity sulfur cathode with exceptional cycling stability for lithium–sulfur batteries. Adv Funct Mater 24(9):1243–1250
38. Jin J et al (2013) Flexible self-supporting graphene-sulfur paper for lithium sulfur batteries. RSC Adv 3(8):2558–2560
39. Elazari R, Salitra G, Garsuch A, Panchenko A, Aurbach D (2011) Sulfur-impregnated activated carbon fiber cloth as a binder-free cathode for rechargeable Li–S batteries. Adv Mater 23(47):5641–5644
40. Su YS, Fu YZ, Manthiram A (2012) Self-weaving sulfur-carbon composite cathodes for high rate lithium-sulfur batteries. Phys Chem Chem Phys 14(42):14495–14499
41. Li N, Chen ZP, Ren WC, Li F, Cheng HM (2012) Flexible graphene-based lithium ion batteries with ultrafast charge and discharge rates. Proc Natl Acad Sci USA 109(43):17360–17365

# Chapter 7
# Conclusions and Perspective

## 7.1 Main Conclusion and Innovations

Developing high-energy density lithium secondary battery has been the focus of worldwide research. In this dissertation, based on the nanocarbon materials and construction of conductive network, we designed and developed high-energy density sulfur/carbon composite cathode materials by confining sulfur in micropores, surface active sites, two graphene membranes, and 3D graphene framework. The results obtained lay insight for the design and development of high capacity, high-power, and long-life Li–S batteries. The main results and innovations are summarized as follows:

1. We selectively immobilized sulfur into the micropores of hierarchical carbon by a melt adsorption-solvent extraction strategy. Micropores in the hierarchical porous carbon have strong adsorption potential to confine sulfur, which acts as solvent-restricted reactors for sulfur lithiation even in carbonate-based electrolytes. We suggested the localized electrochemical transition of "solid–solid" reaction instead of "sulfur-polysulfides-lithium sulfides" reaction through the desolvation effect in sub-nanometre pores. We proposed a "confinement factor" to define the capability to constrain polysulfides. It is obvious that a filling system comprising solely of micropores gives a near-perfect confinement level (96.9%) compared to the meso/macropore confinement systems (4.6%). The micropores restrict the highly soluble polysulfides and improve the sulfur utilization, and the cathode is able to demonstrate a high capacity of 1067 mAh $g^{-1}$ at 0.15 A $g^{-1}$ and operate reversibly over 800 cycles with marginal capacity loss at a rate of 3 A $g^{-1}$.
2. We prepared a cathode, which is a self-supporting fibrous graphene–sulfur (G-S) hybrid, through a one-pot process using the hydrothermal reduction and self-assembly strategy. The surface oxygen-containing functional groups of graphene promote the distribution of sulfur nanocrystals and tight contact of the sulfur with graphene. The G–S hybrid can be cut and pressed into plates for use as Li–S



G. Zhou, *Design, Fabrication and Electrochemical Performance of Nanostructured Carbon Based Materials for High-Energy Lithium–Sulfur Batteries*, Springer Theses,
DOI 10.1007/978-981-10-3406-0_7

battery electrodes without metal current-collector, binder, and conductive additive. The fibrous graphene facilitates electron transfer, the porous network of interconnected graphene allows rapid ion transport, and the sulfur nanocrystals provide short $Li^+$ diffusion distance. Our experimental observations, combined with first-principles calculations, demonstrate that the dissolution/diffusion of polysulfide anions in electrolyte can be greatly reduced by the strong binding of sulfur to the oxygen-containing (mainly hydroxyl/epoxide) groups on reduced graphene oxide, resulting in a high capacity of 1180 mAh $g^{-1}$ at 0.3 A $g^{-1}$, 390 mAh $g^{-1}$ at 4.5 A $g^{-1}$ and improved cyclic stability.

3. We designed a unique sandwich structure with pure sulfur between two graphene membranes. One graphene membrane is used as a current collector (GCC) to replace commercial Al foil with sulfur coated on it as the active material, and the other graphene membrane is coated on a commercial polymer separator (G-separator). The flexible and conductive graphene layers on both sides of the sulfur electrode provide excellent electrical conductivity, and the sandwich structure can accommodate the large volumetric expansion of sulfur during lithiation. The graphene layer on the separator surface acts as a good barrier to mitigate the shuttle effect of dissolved polysulfides. When the discharge current density was increased to 6 A $g^{-1}$, the battery with a sandwich structure can still deliver capacities as high as 750 mAh $g^{-1}$, which indicates an ultrafast charge/discharge capability; and the capacity is 50 times higher than a conventional Li–S battery tested under the same conditions. Furthermore, the sulfur electrode exhibits good cyclic performance and retains a capacity of 679 mAh $g^{-1}$ with a Coulombic efficiency nearly 100% during cycling after 300 cycles at a current density of 1.5 A $g^{-1}$, so the capacity decay is only 0.1% per cycle. For the first time, we used three-dimensional X-ray microtomography to explore sulfur diffusion during cycling. It should be noted that the graphene used is produced through an intercalation-exfoliation method from graphite and is commercially available. These features give the design and materials strong potential for the industrial production and application of Li–S batteries.
4. We synthesized CNTs with sulfur in the wall by template-directed chemical vapor deposition and carbon thermo-reduction of sulfate. Combined with first-principles calculations, it is found that sulfur exists as short-chain-like molecules ($S_{2–4}$) in sub-nanometre pores rather than cyclo-$S_8$ molecules in the pores with a size larger than 1 nm. A binder-free and metal current-collector-free flexible cathode was prepared by ethanol evaporation-induced assembly for Li–S batteries. The membrane cathode can sustain a 10 MPa stress with a 9% strain and shows a high electrical conductivity of 800 S $m^{-1}$, which remains unchanged after 12,000 bend cycles. The micropore-confinement of sulfur in the S-CNT walls hinders polysulfide dissolution and accommodates the large volumetric expansion of sulfur during lithiation, resulting in long cycling stability. Finally, we proposed a flexible Li–S full cell consisting of flexible prelithiated silicon/graphene membrane anode material and S-CNT cathode material. The flexible full cell obtained can work well under flat and bent states, indicating this

S-CNT cathode material and the assembly are potentially adaptable for flexible Li–S batteries and other flexible energy storage devices.

5. We have developed a graphene-foam based flexible electrode to obtain high-performance Li–S batteries through a simple yet effective strategy. A high sulfur loading (10.1 mg $cm^{-2}$) and high sulfur content guaranteed the sulfur cathode to have a high areal capacity (13.4 mAh $cm^{-2}$). The S-PDMS/GF electrode shows high rate performance with a reversible capacity higher than 450 mAh $g^{-1}$ even at a large current density of 6000 mA $g^{-1}$ and retained a stable cyclic performance with $\sim$0.07% capacity decay per cycle over 1000 cycles. This graphene-based flexible electrode structure may also be promising for lithium iron phosphate, lithium titanium oxide, silicon, and other electrode materials in improving the energy density of their devices.

## 7.2 Perspective for Future Works

1. On account of the sulfur confinement in micropores, further efforts can be focused on observing the sulfur states in the micropores and optimizing the pore structure for maximizing the battery performance; improving the mass loading of sulfur in the whole electrode, and designing highly conductive, large pore volume, and strong sulfur confinement systems are effective approaches for reaching the final goals of high energy Li–S batteries.
2. According to the understanding of surface chemistry, exploring the effect of doping atoms such as nitrogen, oxygen, boron, phosphorous, sulfur, or codoping on the electrochemical performance of sulfur/carbon composite cathode materials is needed; Another important way is to combine theoretical calculations and experimental design for getting deep insight on the binding energy of doping atoms with lithium polysulfides, and identifying the mechanism for how binding energy trapping dominate the lithium polysulfide diffusion process and overall battery performance.
3. Based on the concept of designing sandwich cathode structure, next step should be pairing with anode materials to assemble full batteries and explore the possibility for practical applications.
4. Developing gel polymer electrolytes (GPEs) which consist of conventional liquid Li–S electrolytes embedded in a polymer is expected for constructing flexible solid-state Li–S batteries.